

# **Impact of Laser Frequency Noise on Rydberg Superatom Dephasing**

Simon Schroers

Masterarbeit in Physik  
angefertigt im Institut für Angewandte Physik

vorgelegt der  
Mathematisch-Naturwissenschaftlichen Fakultät  
der  
Rheinischen Friedrich-Wilhelms-Universität  
Bonn

June 2025

I hereby declare that this thesis was formulated by myself and that no sources or tools other than those cited were used.

Bonn, .....  
Date

.....  
Signature

- 1. Gutachter: Prof. Dr. Sebastian Hofferberth
- 2. Gutachter: Prof. Dr. Daqing Wang

# Contents

---

|          |  |           |
|----------|--|-----------|
| <b>1</b> | <b>Introduction</b>  | <b>1</b>  |
| <b>2</b> | <b>Coherent Single-Photon-Matter Interaction using Rydberg Superatoms</b>                | <b>3</b>  |
| 2.1      | Rydberg Atoms and their Interactions . . . . .   | 3         |
| 2.1.1    | Adiabatic Elimination . . . . .  | 4         |
| 2.1.2    | Collective Excitations . . . . .   | 5         |
| 2.2      | Single-Photon Rabi Oscillations of Superatoms . . . . .                                  | 6         |
| 2.3      | Dephasing Mechanisms of Rydberg Superatoms . . . . .                                     | 8         |
| 2.4      | Rabi Oscillations with a Noisy Driving Field . . . . .                                   | 12        |
| <b>3</b> | <b>Experimental Setup Creating Rydberg Superatoms</b>                                    | <b>16</b> |
| 3.1      | Experimental Apparatus and Atom Preparation Cycle . . . . .                              | 16        |
| 3.2      | Measuring and Evaluating Rabi Oscillations of Rydberg Superatoms . . . . .               | 18        |
| 3.3      | Two-Photon Excitation Laser System . . . . .   | 19        |
| 3.3.1    | Fast Analog Linewidth Control . . . . .  | 21        |
| 3.3.2    | External Cavity Diode Lasers . . . . .   | 24        |
| 3.3.3    | Frequency Reference Measurements of the Probe and Control Laser . . . . .                | 27        |
| 3.3.4    | Closed Loop Transfer Function of the Feedback Loop . . . . .                             | 28        |
| <b>4</b> | <b>Laser Noise Interferometer</b>  | <b>30</b> |
| 4.1      | Optical and Electronic Setup . . . . .   | 30        |
| 4.2      | Theoretical Interferometer Output Signal . . . . .                                       | 32        |
| 4.3      | Experimental Determination of Laser Frequency Noise Spectra . . . . .                    | 35        |
| 4.4      | Alternative: Using a Fabry-Perot Interferometer instead of a Mach-Zehnder interferometer | 39        |
| <b>5</b> | <b>Influence of Frequency Noise the Two-Photon Rydberg Excitation</b>                    | <b>42</b> |
| 5.1      | Measured Frequency Noise Spectra of the Probe and Control laser . . . . .                | 42        |
| 5.1.1    | Probe Laser . . . . .  | 42        |
| 5.1.2    | Control Laser . . . . .  | 44        |
| 5.2      | Bode's Integral Formula . . . . .  | 45        |
| 5.3      | Stability of the Servo Bump Position . . . . .   | 47        |
| 5.4      | Simulation of a Noisy Two-Photon Rydberg Excitation . . . . .                            | 50        |
| 5.5      | Comparing Simulated and Measured Dephasing Rates . . . . .                               | 53        |
| <b>6</b> | <b>Conclusion &amp; Outlook</b>  | <b>57</b> |
| 6.1      | Outlook . . . . .  | 58        |

**A Appendix** **59**

    A.1 Superatom Dephasing due to Inhomogeneous Density of the Atomic Cloud . . . . . 59

    A.2 Worsened Feedback Loop Settings . . . . . 60

**B Acknowledgements** **62**

**Bibliography** **63**

---

## Introduction

---

Quantum optics experiments study the interaction between quantized matter and photons, the latter are the fundamental particles of light [1]. As a quantum emitter it is natural to consider single atoms. However, the interaction probability between a single photon and a single atom is very small [2].

One method to increase the interaction strength is placing the atom inside an optical cavity, such that the single photon passes the atom multiple times increasing the probability of interaction [3, 4].

Alternatively, one can use ensembles of  $N$  atoms collectively coupled to the light field of interest. Using Rydberg states it is possible to turn many-atom systems into saturable quantum emitters. For sufficiently small ensembles the strong interaction between atoms in the Rydberg state limits the number of excited atoms to one [5]. These ensembles are so-called superatoms and make it possible to achieve coupling enhanced by  $\sqrt{N}$  between photons and a quantum emitter. The enhanced coupling of superatoms has been observed in Rabi oscillations mapped onto few-photon pulses [6], when using superatoms as single-photon sources [7, 8] or when utilizing superatoms as manipulable qubits [9, 10].

Aside the coupling strength, which can be tuned through various parameters such as the strength of the driving field or the number of atoms, another important figure of merit for the quality of a superatom is the coherence time [11]. The coherence time characterizes how long an information transcribed from the light onto the superatom can be reliably stored. A short coherence time leads to a loss of information and varying results when repeating an experiment [12].

In the course of this thesis the coherence time of a superatom is probed by driving few-photon Rabi oscillations. From previous works it is known that the coherence time is limited due to multiple effects: thermal motion of the constituent atoms [13], inhomogeneous density of the atomic cloud [14], differential light shifts due to different trapping potentials for ground and Rydberg state [15] and off-resonant decay from the Rydberg state [6, 16, 17]. This thesis investigates an additional source of decoherence<sup>1</sup>, which is Frequency noise of the lasers driving the system. Frequency noise in the driving field as a source of decoherence has already been described for single Rydberg atoms in tweezers and for ion experiments [20–22]. The goal of this thesis is to characterize the noise of the Rydberg excitation laser system and to assess whether laser frequency noise contributes significantly to the dephasing of the superatom. The structure of this thesis is as follows:

---

<sup>1</sup> Decoherence typically refers to the loss of phase information due to an entanglement between the quantum system and the environment [18]. In the context of the superatom the term decoherence is commonly used to describe all mechanisms leading to a dephasing. These mechanisms can be internal, e.g. thermal dephasing [6], or connected to the environment, e.g. as frequency noise of the driving field [19].

[Chapter 2](#) introduces a mathematical model describing the dynamics of the Rydberg superatom. This includes an overview on the other mechanisms leading to the decoherence. In the end of this chapter the addition of a term accounting for frequency noise induced dephasing to the initial mathematical model is discussed.

In [Chapter 3](#), the experimental setup used for the realization of Rydberg superatoms is introduced, and it is presented how superatom Rabi oscillations are detected with few-photon-pulses. This is followed by a description of the feedback loop used for frequency stabilization of the excitation lasers. It is discussed how the settings of the feedback loop determine the noise characteristics of the driving fields.

[Chapter 4](#) introduces an optical setup that allows to measure the noise characteristics of any laser over a broad range of infrared wavelengths. Afterward, the data post-processing to extract the frequency noise spectral density the laser light source is described.

In [Chapter 5](#), the measured frequency noise spectra of the excitation lasers are presented and discussed. Using a simulation, the impact of the recorded frequency on few-photon Rabi oscillations noise is numerically calculated. The simulation is then used make a prediction on the significance of frequency noise as a source of superatom dephasing. Finally, the simulation effect is compared to the experimentally observed dephasings.

# Coherent Single-Photon-Matter Interaction using Rydberg Superatoms

## 2.1 Rydberg Atoms and their Interactions

Shortly after Balmer had observed the line-spectra in hydrogen Rydberg proposed a formula describing the wavelengths of the observed spectral lines [23]

$$\frac{1}{\lambda} = R_{\infty} \left( \frac{1}{n_1^2} - \frac{1}{n_2^2} \right) \quad (2.1)$$

This proposal sets no boundaries for the choice of  $n_1$  and  $n_2$ , except from being integers. Therefore, this formula postulates the existence of highly excited states with a high principal quantum number  $n$ . These highly excited states can be experimentally observed and are called Rydberg states. They have distinct features, such as a long lifetime (scaling with  $n^{-3}$ ) and a large wave function of the valence electron (scaling with  $n^2$ ) [24]. The large distance between the negatively charged electron and the positively charged atomic core increases the probability to acquire induced dipole moments compared to ground state atoms. This results in a strong response of in the state energy to external electric and magnetic fields, which is typically described by the polarizability  $\alpha_{Ryd}$  scaling with  $n^7$  [24, 25]. The shift of in the Rydberg level caused by an external electric field  $E$  is given by [26]

$$\Delta_{Ryd} = -\frac{1}{2} \frac{\alpha_{Ryd} E^2}{\hbar} \quad (2.2)$$

where  $\hbar$  denotes the reduced Planck constant.

Due to the strong response of Rydberg atoms to electric fields they also strongly interact with each other by inducing dipole moments. If the distance between two Rydberg atoms is significantly larger than their electronic wavefunction, the interaction Hamiltonian can be approximated by multipolar expansion leading to [24]

$$V_{ddi} = \frac{1}{4\pi\epsilon_0} \frac{\vec{d}_1 \cdot \vec{d}_2 - 3(d_1 \cdot \vec{n})(d_2 \cdot \vec{n})}{R^3} \quad (2.3)$$

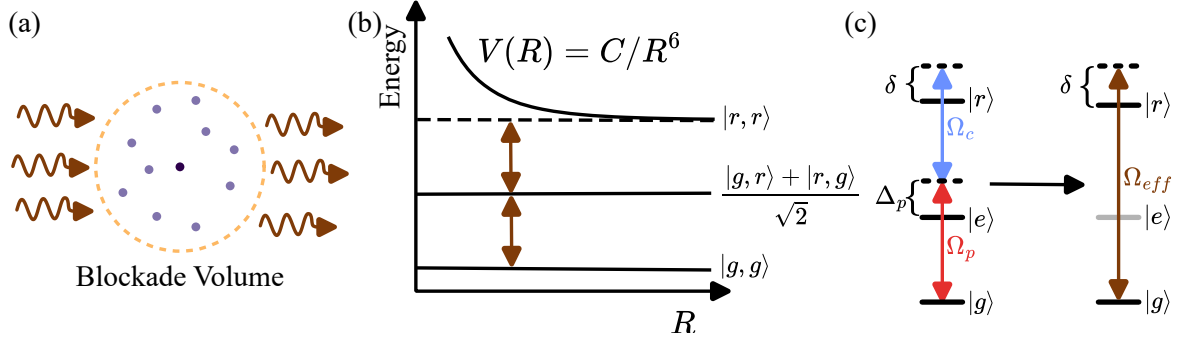


Figure 2.1: Basic principles of the Rydberg superatom. (a) Simple sketch of the experimental system. A single Rydberg atom (dark purple circle) with multiple ground state atoms (light purple) inside its blockade volume (dashed yellow circle). The atomic cloud is illuminated with single photons resonant to the ground-to-Rydberg transition (brown arrows) and the transmitted light is measured. (b) Energy scheme of system of two atoms as a function on the interatomic distance  $R$ . Each atom can be either in the ground state (denoted as  $g$ ) or the Rydberg state (denoted as  $r$ ). All energy levels are labeled with the corresponding collective state. The brown arrows indicate the energy brought into the system by the external driving field. The energy of  $|r, r\rangle$  is shifted due to the van der Waals interaction of the Rydberg atoms, giving rise to the blockade effect. (c) Adiabatic elimination. Level scheme of a single atom with the ground state  $|g\rangle$  the intermediate state  $|e\rangle$  and the Rydberg state  $|r\rangle$ . The two-sided-arrows indicate an external field driving the system: The probe field (red) with Rabi frequency  $\Omega_p$ , the control field (light blue) driving with  $\Omega_c$  and the effective field (brown). If the detuning is large enough one can consider the system instead of a three-level-system (left side) as a two-level system driven by the effective field (right side).

where  $d_1$  and  $d_2$  are the dipole operators of the two atoms,  $\vec{n}$  is the normalized vector between the atoms and the interatomic distance  $R$  characterizes the strength of the dipole-dipole interaction  $V_{\text{ddi}}$ . For the case where both Rydberg atoms are in the same s-state, applying non-degenerate perturbation theory leads to a van der Waals interaction between the atoms scaling with  $V_{\text{vdW}} = C_6/r^6$  as illustrated in Figure 2.1 [24, 27, 28].

This strong interaction gives rise to the Rydberg blockade: The presence of a Rydberg atom shifts the energy levels of other atoms in its vicinity [29, 30]. If an atomic ensemble is illuminated with a field with a Rabi frequency  $\Omega$  coupling the ground state to the Rydberg state, the presence of the Rydberg atom prevents the other atoms from being excited. The sphere around a Rydberg atom in which ground state atoms are blocked meaning  $V > \hbar\Omega$  has a radius

$$R_b = \sqrt[6]{C_6/(\hbar\Omega)} \quad (2.4)$$

Thus, inside the blockade sphere only a single atom can be excited into the Rydberg state [5, 31]. In our experiment the atomic cloud is confined to a volume smaller than the blockade sphere (see Figure 2.1 (a)) such that exactly one atom in the prepared atomic cloud can be excited in the Rydberg state.

### 2.1.1 Adiabatic Elimination

In the experiment the Rydberg excitation of the individual atoms is realized by combining two light fields: A *probe* and a *control* field (see Figure 2.1 (c)) connecting the ground state  $|g\rangle$  the intermediate state  $|e\rangle$  and the Rydberg state  $|r\rangle$ . The probe field drives the transition between  $|g\rangle$  and  $|e\rangle$  with a Rabi

frequency  $\Omega_p$  and a detuning  $\Delta_p$  of the light relative to the transition frequency. The control drives the transition between  $|e\rangle$  and  $|r\rangle$  with the Rabi frequency  $\Omega_c$  and the detuning  $\Delta_c = \Delta_p - \delta$ , where  $\delta$  is the two-photon detuning (see Figure 2.1 (c)). The Hamiltonian describing the driven single three-level atom is [32]

$$\mathcal{H} = \frac{\hbar}{2} \begin{bmatrix} 0 & \Omega_p & 0 \\ \Omega_p & 2\Delta_p & \Omega_c \\ 0 & \Omega_c & 2(\Delta_p - \delta) \end{bmatrix} \quad (2.5)$$

after the rotating wave approximation applied, neglecting fast oscillating terms for the atomic state. In the Hamiltonian the diagonal terms describe the energies of each states while the off-diagonal terms characterize the coupling between the terms. To obtain the populations one has to solve the system dynamics under the influence of the Hamiltonian  $\mathcal{H}$ . To approximate a two-level system one chooses  $\Delta_p$  to be large compared to the linewidth of the laser and  $\delta$  to adiabatically eliminate the intermediate state  $|e\rangle$ . In this case  $|e\rangle$  is barely populated and has a population that is changing much faster in time than the populations of  $|g\rangle$  and  $|r\rangle$  [33]. The effective coupling of such a two level system is given by [32]

$$\Omega_{\text{eff},2\gamma} = \frac{\Omega_c \Omega_p}{2\Delta_p}. \quad (2.6)$$

Even though, the intermediate state has little population it still introduces an additional decay channel to the Rydberg atom: The Rydberg  $|r\rangle$  can be off-resonantly coupled to the intermediate state  $|e\rangle$  and then undergo a spontaneous decay with the rate  $\Gamma_e$ . The overall rate for such this process is given by [32]

$$\Gamma = \frac{\Omega_c^2}{4(\Delta_p - \delta)^2} \Gamma_e \quad (2.7)$$

Since the lifetime of the Rydberg state is very long, this effect is the dominant channel of spontaneous decay especially if Rydberg and ground state are in the  $s$ -state. Using a two-photon transition with a large  $\Delta_p$  has multiple advantages over a single photon excitation scheme: Firstly, the two-photon excitation allows a broader range of Rydberg states: For example the ground and the Rydberg state can both be  $s$ -states, which would be dipole-forbidden for a single photon excitation. Secondly, the Rabi frequencies of the probe and the control can be freely chosen. This offers the possibility of combining a single-photon probe beam with a strong control beam [32].

### 2.1.2 Collective Excitations

To further investigate the characteristics the atomic cloud inside the blockade sphere, let us consider two atoms with driven by a field that is resonant with the ground-to-Rydberg transition. Figure 2.1 (b) shows the energy level scheme of such a case. The state of the two-atom system can be described in a collective basis. The collective ground state  $|gg\rangle$ , with both atoms in the ground state is resonantly coupled to the states  $|gr\rangle$  and  $|rg\rangle$  which contain exactly one Rydberg and one ground state atom with a coupling strength  $\Omega$ . The  $|rr\rangle$  state contains both atoms excited to the Rydberg state. Whether the  $|rr\rangle$  state can be excited depends strongly on the distance  $R$  between the two atoms. If their distance is smaller than the blockade radius  $R_b$  the  $|rr\rangle$  state cannot be excited (see Figure 2.1(b)). If both atoms are driven by the external field at the same time, one cannot differentiate between the states  $|gr\rangle$  and  $|rg\rangle$ . Thus,

the field drives the transition between the ground  $|gg\rangle$  and the superposition state  $(|gr\rangle + |rg\rangle)/\sqrt{2}$  with a coupling of  $\sqrt{2}\Omega$  if the interatomic distance is smaller than the blockade radius. The increased coupling is a direct consequence of the Rydberg blockade and does not apply if the system is not fully blockaded [29, 30, 34].

## 2.2 Single-Photon Rabi Oscillations of Superatoms

We now want to expand the concept of enhanced coupling from the two-atom ensemble to  $N$  atoms in a cloud inside the blockade sphere. In this case one considers the coupling between the ground state  $|G\rangle = |g_1, \dots, g_N\rangle$  and a collective excited state [6]

$$|W\rangle = (1/\sqrt{N}) \sum_{j=1}^N e^{i\vec{k}\cdot\vec{x}_j} |j\rangle \quad (2.8)$$

where  $|j\rangle = |g_1, \dots, r_j, \dots, g_N\rangle$  denotes the state with the  $j$ -th atom in the Rydberg state,  $\vec{x}_j$  being the location of the  $j$ -th atom and  $\vec{k}$  being the wavevector of the driving field. The coupling between the  $|G\rangle$  and  $|W\rangle$  scales with  $\sqrt{N}$  since the light can couple to every single atom. This system of a cloud of many atoms inside the blockade sphere and strongly and described by such a two-level system is called a *Rydberg superatom* [5, 6].

Now we consider a system of a superatom consisting of  $N$  atoms is driven by an external light field consisting of a probe and a control beam. The weak probe field is used to control the excitation and deexcitation of the atomic ensemble via absorption and stimulated emission of single photons. By analyzing the transmitted (single-photon) probe field the dynamics of the superatom can be resolved. The control field is used to increase the coupling between light field and the superatom. Thus, in the following model one treats the system as if it was driven by the probe field with the amplitude  $\alpha(t)$ , which is related to the incoming photon rate via  $R_{\text{in}}(t) = |\alpha(t)|^2$ . The coupling between the  $|G\rangle$  and  $|W\rangle$  is given by [6]

$$\Omega_{GW} = 2\sqrt{N}g_0 \frac{\Omega_c}{2\Delta_p} \alpha(t), \quad (2.9)$$

where  $g_0$  describes the coupling between the atom and the light. Thus, one can control the coupling, through the choice of the atomic transition ( $g_0$ ), the number of atoms  $N$ , the power of the control ( $\Omega_c$ ) and the detuning of the probe  $\Delta_p$ . All this is summarized in  $\kappa = Ng_0^2 \frac{\Omega_c^2}{4\Delta_p^2}$  such that  $\Omega_{GW} = 2\sqrt{\kappa}\alpha(t)$ .

The state  $|W\rangle$  carries an imprint of the wavevector  $\vec{k}$  of the exciting light in  $e^{i\vec{k}\cdot\vec{x}_j}$ . These phase factors cause the atomic ensemble to emit photons (with wavevector  $\vec{k}_e$ ) via spontaneous decay into the exciting mode such that  $\vec{k} = \vec{k}_e$ , which is referred to as *single photon superradiance*. Just like the coupling the rate of spontaneous emission in the forward direction is increased by  $\sqrt{N}$  [35]. In the context of the two-photon excitation scheme, this means that the photons emitted due to spontaneous emission propagate in the directions the probe and control beam. Due to this feature, this state is referred to as the *bright state*.

The Hilbert space containing  $|G\rangle$  and  $|W\rangle$  also contains  $N - 1$  other states denoted as  $\{|D\rangle\}_{i=1}^{N-1}$  (see Figure 2.2). These also carry a single Rydberg excitation, but are not coupled to the driving laser field

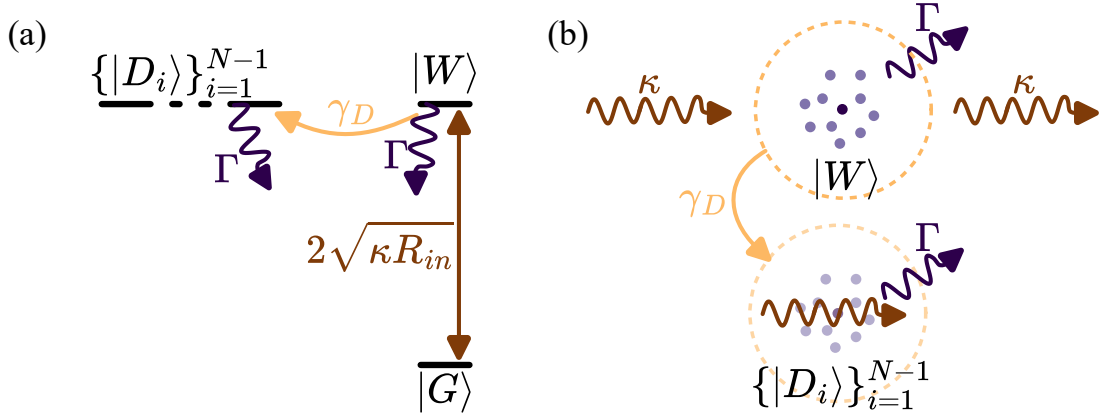


Figure 2.2: Rydberg superatom schemes. (a) Simplified level scheme of the Rydberg superatom consisting of  $N$  atoms with the collective ground state  $|G\rangle$ , the collective bright state  $|W\rangle$  and the dark states  $\{|D_i\rangle\}_{i=1}^{N-1}$ . The brown arrow indicates the effective light field driving the system. Dark purple arrows indicate the spontaneous decay of  $|W\rangle$  and  $\{|D_i\rangle\}_{i=1}^{N-1}$  into  $|G\rangle$  via the intermediate state with rate  $\Gamma$ . The yellow arrow indicates the dephasing of a bright state into a superposition of dark states. (b) Interaction of the probe field with a Rydberg superatom consisting of a cloud of ground state atoms (light purple) and a single Rydberg atom (dark purple) inside the blockade sphere (yellow dashed). The brown arrows describe the interaction of the probe field with the atomic cloud for the ensemble in the bright state (upper) and the dark states (lower).

due to different phase factors  $e^{i\vec{k}\cdot\vec{x}_j}$  making them orthogonal to  $|W\rangle$ . As a cloud in a state  $\{|D_i\rangle\}$  is blocked the cloud becomes transparent for the driving field (see Figure 2.2). Therefore, the states  $\{|D_i\rangle\}_{i=1}^{N-1}$  are referred to as *dark states* [6, 19]. Also, these states do not exhibit superradiance in the direction of the driving field.

$|W\rangle$  and  $\{|D_i\rangle\}_{i=1}^{N-1}$  form an orthonormal basis and are thus in theory not coupled to each other. However, there are processes that cause the transition from  $|W\rangle$  to a superposition of  $\{|D_i\rangle\}_{i=1}^{N-1}$ . This can be approximated as an irreversible decay with the rate  $\gamma_D$ . Due to multiple dephasing mechanisms with a combined decay rate  $\gamma_D$  a collective bright state  $|W\rangle$  transitions into a superposition of the dark states  $\{|D_i\rangle\}_{i=1}^{N-1}$  over time preventing the laser from driving a transition back into the ground state  $|G\rangle$  (these will be highlighted in section 2.3).

Both  $|W\rangle$  and  $\{|D_i\rangle\}_{i=1}^{N-1}$  can decay into  $|G\rangle$  with the rate  $\Gamma$  due to the control laser deexciting the atom in the intermediate state from where it decays spontaneously [6]. For the previously introduced model shown in Figure 2.2 one can formulate an effective Hamiltonian describing the light field driving the atom as [6, 36]

$$H_{\text{eff}}(t) = \hbar\sqrt{\kappa}(\alpha^*(t)\sigma_{GW} + \alpha(t)\sigma_{GW}^\dagger) + \delta/2(\sigma_{DD} + \sigma_{WW} - \sigma_{GG}) \quad (2.10)$$

with  $\sigma_{\alpha\beta} = |\alpha\rangle\langle\beta|$  being the excitation/deexcitation of the superatom and  $\alpha^*(t)/\alpha(t)$  describing the coherent light field of the probe. Using this effective Hamiltonian one can formulate a master equation,

which describes the change in the atomic density function in time as [6, 36]

$$\partial_t \rho(t) = -\frac{i}{\hbar} [H_{\text{eff}}(t), \rho(t)] + \kappa \mathcal{L}[\sigma_{GW}] \rho(t) + \gamma_D \mathcal{L}[\sigma_{DW}] \rho(t) + \Gamma (\mathcal{L}[\sigma_{GD}] + \mathcal{L}[\sigma_{GW}]) \rho(t) \quad (2.11)$$

where  $\mathcal{L}[\sigma] \rho = \sigma \rho \sigma^\dagger - (\sigma^\dagger \sigma \rho + \rho \sigma^\dagger \sigma)/2$  is the Lindblad superoperator. The master equation contains all dynamics that were previously introduced (see Figure 2.2): The first term describes the light field coherently driving the two-level-system of  $|G\rangle$  and  $|W\rangle$ , causing a Rabi oscillations with a frequency  $\Omega_{\text{eff}} = \sqrt{4\kappa R_{\text{in}}}$  between the two states.

The second term describes the enhanced spontaneous emission of the bright state into exciting mode of the probe laser. The third term captures the decay of the collective bright state into a superposition of the dark states with the rate  $\gamma_D$ . The fourth term captures the decay of a Rydberg state (independent whether bright or dark state) into the collective ground state. Photons emitted in this process are radiated into an arbitrary direction (and therefore not captured by the detectors in the experiment).

In order to make the Rydberg superatom a useful system for quantum experiments one aims to increase the coherence time of the system. The decay of the Rabi oscillation amplitude characterizes the coherence time of the superatom. Therefore, to obtain long coherences one has to increase the coupling  $\kappa$ , while keeping the dephasing  $\gamma_D$  and the rate of spontaneous emission  $\Gamma$  as low as possible.

When the incoming light field  $\alpha(t)$  and the initial state of the atomic ensemble is known, one can numerically solve the master equation (in our case we use QuTip [37] to determine the population of the  $|D\rangle$ ,  $|W\rangle$  and  $|G\rangle$  - see Figure 2.3). The influence the light field has on the state of the superatom is described in Equation 2.10, but not the impact of the superatom on the light field. With knowledge of the superatom density matrix one can calculate the electric field transmitted through the superatom as the sum of the incoming field  $\alpha(t)$  and the field emitted/absorbed by the atomic ensemble [6]

$$E(t) = \alpha(t) - i\sqrt{\kappa} \sigma_{GW}(t) \quad (2.12)$$

From Equation 2.12 one can deduce the expected outgoing photon rate at the location of the superatoms as [6]

$$R_{\text{out}} = |E(t)|^2 = |\alpha(t)|^2 + \kappa \langle \sigma_{GW}^\dagger(t) \sigma_{GW}(t) \rangle - i\sqrt{\kappa} [\alpha^*(t) \langle \sigma_{GW}(t) \rangle - \alpha(t) \langle \sigma_{GW}^\dagger(t) \rangle]. \quad (2.13)$$

Therefore, with the knowledge of the incoming field  $\alpha(t)$  one can calculate on the outgoing field that only depends on  $\kappa$ ,  $\gamma_D$  and  $\Gamma$  [6]. Figure 2.3 shows the population and the photon rate with realistic experimental parameters calculated using QuTip.

## 2.3 Dephasing Mechanisms of Rydberg Superatoms

As one can see in Figure 2.3 the dark states  $\{|D\rangle\}_{i=1}^{N-1}$  are expected to play a significant role when performing single-photon Rabi oscillations with the superatom. In this section three effects leading to the dephasing from  $|W\rangle$  to  $\{|D\rangle\}_{i=1}^{N-1}$  will be introduced: thermal motion of the atoms [13], differential light shifts of the atoms due to different trapping potentials for ground and Rydberg states [15] and the energy shifts due an inhomogeneous density in the atom cloud [14]. A more detailed description of these mechanisms can be found in [16, 17].

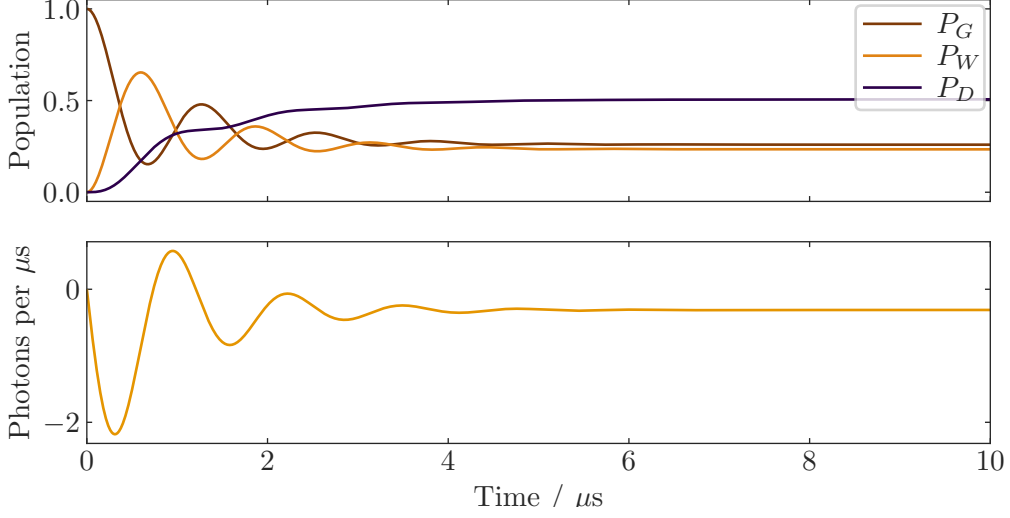


Figure 2.3: Superatom state population and photon rate for realistic experimental parameters. (Upper) Population of the states  $|G\rangle$ ,  $|W\rangle$  and  $\{|D\rangle\}_{i=1}^{N-1}$  over time. (Lower) Difference between the incoming  $R_{\text{in}}$  and the outgoing light field  $R_{\text{out}}$ . The calculation was done using QuTip `mesolve` with the system initially prepared at  $|G\rangle$ . For the calculation  $\kappa = 0.31$  MHz,  $\Gamma = 0.42$   $1/\mu\text{s}$ ,  $\gamma_D = 0.91$   $1/\mu\text{s}$  and a time-constant probe photon field with  $R_i n = 20$   $1/\mu\text{s}$  was used.

Firstly, the thermal motion of the constituent atoms lead to dephasing of the bright state  $|W\rangle$  into the dark states  $\{|D\rangle\}_{i=1}^{N-1}$ . This is due to the atoms changing their position affecting the phase terms  $e^{i\vec{k}\vec{x}_j}$  of the state with the  $j$ -th atom excited. If the overlap between the collective state of the atoms and the (ideal) bright state  $|W\rangle$  is reducing this means that the coupling between the light field and the superatom decreases. Assuming that the velocity distribution of the atomic ensemble in the direction of the wavevector  $\vec{k}$  is a Boltzmann distribution, one can derive that the overlap between the initial state  $|\psi(0)\rangle = |W\rangle$  and the state at the time  $t$  is given by [17]

$$|\langle\psi(0)|\psi(t)\rangle|^2 = \exp\left(-t^2/\tau_{\text{thermal}}^2\right) \quad \text{with} \quad \tau_{\text{thermal}} = \sqrt{\frac{m}{k^2 k_B T}} \quad (2.14)$$

where  $k$  is the length of the wavevector,  $m$  is the mass of the atoms,  $k_B$  is the Boltzmann constant and  $T$  denotes the temperature of the atomic ensemble. For typical parameters in the experiment of  $T = 3$   $\mu\text{K}$ , a mass of  $m_{Rb87} = 1.443 \times 10^{-25}$  kg[38] and  $k = 2\pi \cdot (1/480 \text{ nm} - 1/780 \text{ nm}) = 8.01 \times 10^5$   $1/\text{m}$  this leads to  $\tau_{\text{thermal}} \approx 11.7$   $\mu\text{s}$ . Since this effect leads to a dephasing of the state  $|W\rangle$  into the states  $\{|D\rangle\}_{i=1}^{N-1}$  this process contributes to the dephasing characterized by  $\gamma_D$ .

Secondly, one has to take into account differential light shifts of the ground states  $|g\rangle$  and the Rydberg states  $|r\rangle$  of the individual atoms. In the experiment the atoms are trapped using the optical dipole force using a focused laser beam (red-detuned to the  $D_2$ -line). This trapping method utilizes the AC Stark effect shifting the energy levels of the ground state atoms, which attracts the atoms to the highest intensity

of the beam. The shift of the energy level of the ground state is proportional to the intensity  $I(\vec{x})$  [16, 39]

$$\Delta E_g = -\frac{\alpha_g}{4} I(\vec{x}) \quad (2.15)$$

where  $\alpha_g$  is the ground-state polarizability. The value of  $\alpha_g$  depends on the detuning from the  $D_1$ -line of Rb-87 and is specific for the ground state of Rubidium. The sign of  $\alpha_g$  determines whether the atoms are attracted or repulsed by the trapping beam. Each state of Rubidium has a different polarizability and therefore a different trapping potential. In the case of the Rydberg states the potential also depends on the intensity profile of the trapping light, since one has to take into account that the valence electron samples the potential around the position of the atomic core (see [16]). If one neglects this effect, approximating the trapping potential over the extent of the electrons wavefunction one obtains [16]

$$\Delta E_r = -\left( \frac{D_{ar}^2}{16\hbar\Delta_{ar}} - \frac{\alpha_f}{4} \right) I(\vec{x}) \quad (2.16)$$

where the trapping light is detuned by  $\Delta_{ar}$  to the transition from  $|r\rangle$  to  $|a\rangle$  characterized by the dipole matrix element  $D_{ar}$  and  $\alpha_f$  is the free-electron polarizability.

Comparing Equation 2.15 and Equation 2.16 one sees that if the  $\alpha_g \neq \frac{D_{ar}^2}{4\hbar\Delta_{ar}} + \alpha_f$ , this means that  $\Delta E_g - \Delta E_r \neq 0$ . Therefore, the atom excitation energy depends on their position in the optical trap. This can also be understood as a position-dependent detuning of the atoms when driving the system with a monochromatic light source. If the superatom is initially prepared in  $|\psi(0)\rangle = |W\rangle$  then after the time  $t$  it is in the state [39]

$$|\psi(t)\rangle = (1/\sqrt{N}) \sum_{j=1}^N e^{i(\vec{k}\cdot\vec{x}_j + H_{gr}(\vec{x}_j)/\hbar t)} |j\rangle \quad (2.17)$$

where  $H_{gr}(\vec{x}_j)$  is the two-level Hamiltonian characterizing the interaction between the driving field and the  $j$ -th atom. The position-dependence of the Hamiltonians causes the phases of the states in the sum, to evolve with different frequencies  $\omega_j \cdot \hbar |j\rangle = H_{gr}(\vec{x}_j) |j\rangle$  leading to a dephasing of the collective bright state  $|W\rangle$  into the dark states.

To give a rough estimate of the effect we look at a simplified case: We assume that an atomic cloud is trapped in the  $y$ -direction, which is the probe direction, by a Gaussian beam with a waist  $w$  and a peak intensity  $I_0$  with the intensity profile

$$I(y) = I_0 e^{-\frac{y^2}{w^2}}. \quad (2.18)$$

Since the trapping potential for the ground and Rydberg state atoms ( $U_g(y)$  and  $U_r(y)$ ) is directly proportional to the intensity profile and assuming that the atoms are only sitting around the potential minimum, one can approximate the potential using a Taylor expansion

$$U_{g/r}(y) = -\alpha_{g/r} I_0 e^{-\frac{y^2}{w^2}} = \alpha_{g/r} \cdot I_0 \left( 1 - \frac{y^2}{w^2} + \mathcal{O}(y^4) \right), \quad (2.19)$$

where  $\alpha_r = \frac{D_{ar}^2}{4\hbar\Delta_{ar}} - \alpha_f$  is the combined Rydberg polarizability. Using the trapping potential for the ground state one can deduct the normalized atomic density of the form [40]

$$n(y) = \frac{e^{-\frac{U_g(y)}{k_B T}}}{\int e^{-\frac{U_g(y)}{k_B T}}} \quad (2.20)$$

where  $k_B$  denotes the Boltzmann constant and  $T$  the temperature of the atomic ensemble. The differential light shift is the difference between the ground state and the Rydberg state trapping potential

$$\Delta_{dl}(y) = U_r(y) - U_g(y) = (\alpha_r - \alpha_g)/4 \cdot I_0 \left(1 - \frac{y^2}{w^2}\right). \quad (2.21)$$

With Equation 2.21 we can calculate the overlap of the bright state wave function with the superatom wavefunction after the time  $t$

$$|\langle W|\psi(t)\rangle|^2 = \left| \frac{1}{\sqrt{N}} \sum_{j=1}^N e^{-ik_y \cdot y_j} \langle j| \frac{1}{\sqrt{N}} \sum_{j=1}^N e^{i(k_y \cdot y_j + \Delta_{dl}(y_j)/\hbar t)} |j\rangle \right|^2 = \left| \frac{1}{N} \sum_{j=1}^N e^{i\Delta_{dl}(y_j)/\hbar t} \right|^2 \quad (2.22)$$

We now replace the sum by an integral using  $\sum_i f(y_i) \rightarrow N \int dy n(y) f(y)$  under the condition that the number of atoms is large [41] leading to

$$|\langle W|\psi(t)\rangle|^2 = \left| \frac{\int dy e^{-\frac{U_g(y)}{k_B T}} e^{i\Delta_{dl}(y)/\hbar t}}{\int e^{-\frac{U_g(y)}{k_B T}}} \right|^2 \quad (2.23)$$

$$= \left| e^{i(\alpha_r - \alpha_g)/4\hbar \cdot I_0 t} \frac{\int dy e^{-\left(\frac{\alpha_g}{k_B T} + i(\alpha_r - \alpha_g)/\hbar t\right) \frac{y^2 \cdot I_0}{4w^2}}}{\int dy e^{-\frac{y^2 \cdot I_0 \alpha_g}{4k_B T w^2}}} \right|^2 \quad (2.24)$$

$$= \frac{1}{1 - \left(\frac{\alpha_r}{\alpha_r} - 1\right)^2 \left(\frac{t \cdot k_B T}{\hbar}\right)^2}. \quad (2.25)$$

This result corresponds to a first order Taylor expansion of a Gaussian decay of the form  $\exp(-t^2/\tau_{dl})$  with a time constant  $\tau_{dl} = \left(\frac{\alpha_r}{\alpha_r} - 1\right) \frac{k_B T}{\hbar}$ . In our model this effect is approximated assuming that it contributes to the overall dephasing rate  $\gamma_D$ .

Thirdly, one has to consider that the excitation energy of the Rydberg atom is shifted by the presence of other ground state atoms nearby. Rydberg atoms can form molecules with ground state atoms, if the valence electron scatters with a ground state atom inside the Rydberg electron wave function [42]. In this way dimers, trimers etc. can be formed consisting of a Rydberg atom and one, two etc. ground state atoms. If the atomic ensemble is very dense and the Rydberg atom is in a highly excited state the individual molecular lines are not resolved but instead a shift in the Rydberg line is observed [42]. In first order one can approximate the shift of the atomic line due to the density of the atomic cloud  $\rho_n(\vec{x})$

as [42]:

$$\Delta E_\rho = \frac{2\pi\hbar^2 a}{m_e} \underbrace{\int d\vec{x} |\Psi_e(\vec{x})|^2 \rho_n(\vec{x})}_{\overline{\rho_n}} = \frac{2\pi\hbar^2 a}{m_e} \overline{\rho_n} \quad (2.26)$$

where  $\Psi_e(\vec{x})$  denotes the wavefunction of the Rydberg electron,  $a$  is the scattering length,  $m_e$  denotes the electron mass and  $\rho_n(\vec{x})$  is the density of ground state atoms in the atomic ensemble. The atomic density weighted by the electrons wavefunction  $\overline{\rho_n}(\vec{x})$  differs depending on the position of the atom in the cloud due to the inhomogeneous density of the atomic cloud. Similarly to the differential light shift this causes the detuning of driving field relative to the ground-to-Rydberg state transition to differ depending on the position of the Rydberg atom. Therefore, one expects steep density gradients to give rise to a similar dephasing behavior of  $|W\rangle$  as for the differential light shift. [section A.1](#) in the appendix describes the experimental confirmation, that this effect contributes significantly to the overall dephasing  $\gamma_D$ .

To reduce the differential light shifts and thermal motion a magic wavelength lattice trap had been introduced to trap the atomic cloud in the vacuum chamber (a detailed description is given in [16, 17]). In that case the wavelength of the trapping beams is chosen, such that the light shifts of the ground and of the Rydberg state become equal. Under these circumstances the differential light shift vanishes. With the trapping light a one-dimensional optical lattice in the direction of the probe and the control beam (y-direction) was realized. The trap limits the thermal motion of the atoms in the direction of the wavevector  $\vec{k}$  to one lattice site, leading to a reduction in the thermal dephasing. However, this came at the cost of increasing the atomic density in each lattice site. The confinement leads to steep density profile increasing the dephasing due to inhomogeneous density. Overall with the introduction of the magic trap no significant improvement of the coherence time (or reduction of  $\gamma_D$ ) in the superatom could be achieved.

## 2.4 Rabi Oscillations with a Noisy Driving Field

In the model of [Equation 2.11](#) the various effects leading to a dephasing are solely captured in  $\gamma_D$ . In previous works ([6, 36]) this  $\gamma_D$  was also used to capture the dephasing due to fluctuations in the driving lasers. This thesis investigates the impact of laser noise on the loss of coherence in more detail with the goal of separating this effect from the other dephasing effects.

Laser noise can either be described as random fluctuations in the laser phase or fluctuations of the laser frequency. This feature is typically characterized using the phase or frequency noise power spectral density  $S_\Phi(f)/S_\nu(f)$ , where  $f$  denotes the Fourier frequencies of the noise components. They are connected via [43]

$$S_\nu(f) = f^2 S_\Phi(f) \quad (2.27)$$

and therefore can be directly translated into each other.

To consider the impact of frequency noise, the superatom is modeled as a two level system with the states  $|W\rangle = \begin{pmatrix} 1 \\ 0 \end{pmatrix}$  and  $|G\rangle = \begin{pmatrix} 0 \\ 1 \end{pmatrix}$ . The two-level system is driven by a laser field with the Rabi frequency  $\Omega'_{\text{eff}}(t) = \Omega_{\text{eff}} \cdot e^{-i\Phi(t)}$ , where  $\Phi(t)$  denotes fluctuations in the phase due to the phase noise

and a detuning  $\delta$  [44]. In that case the effective Hamiltonian looks like this:

$$H(t) = \hbar \begin{bmatrix} \delta/2 & \Omega_{\text{eff}}(t)/2 \\ \Omega_{\text{eff}}^*(t)/2 & -\delta/2 \end{bmatrix} = \hbar \left( \sigma_z \frac{\delta}{2} + \frac{\Omega_{\text{eff}}}{2} \begin{bmatrix} 0 & e^{i\Phi(t)} \\ e^{-i\Phi(t)} & 0 \end{bmatrix} \right), \quad (2.28)$$

where  $\sigma_x$ ,  $\sigma_y$  and  $\sigma_z$  denote the Pauli matrices. If one applies the unitary transformation

$$U = e^{-i\frac{\Phi(t)}{2}\sigma_z} = \begin{bmatrix} e^{-i\frac{\Phi(t)}{2}} & 0 \\ 0 & e^{i\frac{\Phi(t)}{2}} \end{bmatrix} \quad (2.29)$$

$$\text{with } \dot{U} = e^{-i\frac{\Phi(t)}{2}\sigma_z} \cdot \left( -i\frac{\dot{\Phi}(t)\sigma_z}{2} \right) \quad (2.30)$$

using the transformation rule  $H \rightarrow UHU^\dagger + i\hbar\dot{U}U^\dagger =: \check{H}$  [39, 45] one obtains

$$\check{H} = \underbrace{e^{-i\frac{\Phi(t)}{2}\sigma_z} \hbar \left( \sigma_z \frac{\delta}{2} + \frac{\Omega_{\text{eff}}}{2} \begin{bmatrix} 0 & e^{i\Phi(t)} \\ e^{-i\Phi(t)} & 0 \end{bmatrix} \right) e^{i\frac{\Phi(t)}{2}\sigma_z}}_{UHU^\dagger} + \underbrace{\hbar \dot{\Phi}(t) \frac{\sigma_z}{2}}_{i\hbar\dot{U}U^\dagger} \quad (2.31)$$

$$= \hbar \sigma_z \frac{\delta}{2} + \hbar \frac{\Omega_{\text{eff}}}{2} \sigma_x + \hbar \dot{\Phi}(t) \frac{\sigma_z}{2} \quad (2.32)$$

$$= \hbar \begin{bmatrix} (\delta + \dot{\Phi}(t))/2 & \Omega_{\text{eff}}/2 \\ \Omega_{\text{eff}}/2 & -(\delta + \dot{\Phi}(t))/2 \end{bmatrix} \quad (2.33)$$

Comparing Equation 2.33 and Equation 2.28 one sees that a fluctuation in the phase affecting the driving field can also be seen as a fluctuation in the frequency affecting the detuning of the light field driving the system.

The fluctuations in the driving field frequency distorts the sinusoidal oscillation of the ground and Rydberg state population. If one averages over multiple realizations of this system this appears as a dephasing mechanism leading to a reduction in the oscillation amplitudes. In the following this loss of coherence shall be modeled. For that we start with the Von-Neumann-equation considering only the two-level-system and neglecting other dephasing and decay terms and assume that the frequency fluctuation is white noise. The Hamiltonian is written as a superposition of the Pauli matrices  $\sigma_x$  and  $\sigma_z$  [45]:

$$\partial_t \rho(t) = -\frac{i}{\hbar} \left[ \underbrace{\hbar \sigma_z \frac{\delta}{2} + \hbar \frac{\Omega_{\text{eff}}}{2} \sigma_x}_{H_{\text{eff}}} + \underbrace{\hbar \frac{\dot{\Phi}(t)}{2} \sigma_z}_{H_v(t)} \right] \rho(t) \quad (2.34)$$

To simplify the following calculation we look at the case where the two-photon detuning is zero and assume that the frequency fluctuations are significantly faster than the dynamics of the effective Hamiltonian driving the system. Integrating the Von-Neumann-equation from  $t = 0$  and using the

linearity of the commutator leads to:

$$\rho(t) = \rho(0) - i \left( \int_0^t dt' \frac{\Omega_{\text{eff}}}{2} [\sigma_x, \rho(t')] + \int_0^t dt' \frac{\dot{\Phi}(t')}{2} [\sigma_z, \rho(t')] \right). \quad (2.35)$$

Plugging this relationship into the density matrix in the second integral leads to five terms:

$$\begin{aligned} \rho(t) = & \underbrace{\rho(0)}_{(I)} - i \left( \underbrace{\int_0^t dt' \frac{\Omega_{\text{eff}}}{2} [\sigma_x, \rho(t')]}_{(II)} + \underbrace{\int_0^t dt' \frac{\dot{\Phi}(t')}{2} [\sigma_z, \rho(0)]}_{(III)} \right) \\ & - \left( \underbrace{\int_0^t dt' \int_0^{t'} dt'' \frac{\dot{\Phi}(t') \Omega_{\text{eff}}}{4} [\sigma_z, [\sigma_x, \rho(t'')]]}_{(IV)} + \underbrace{\int_0^t dt' \int_0^{t'} dt'' \frac{\dot{\Phi}(t') \dot{\Phi}''(t')}{4} [\sigma_z, [\sigma_z, \rho(t'')]]}_{(V)} \right). \end{aligned} \quad (2.36)$$

Term  $(I)$  describes the starting value of the density matrix at  $t = 0$  and term  $(II)$  describes the time evolution of the density matrix in the ideal case. Assuming that the noise fluctuates very fast around the carrier leads to  $\int dt' \dot{\Phi}(t') = 0$  and the term  $(III)$  vanishes. Term  $(IV)$  averages out if the system is realized multiple times (e.g. see [46]). To calculate  $(V)$  we use that white noise is uncorrelated. Then one can use that  $\langle \dot{\Phi}(t) \dot{\Phi}(t + \tau) \rangle = \alpha_W \delta(\tau)$ , where  $\delta$  denotes the Delta function and  $\alpha_W$  scales with the noise power [47]. With these approximations one obtains the following form for an averaged density matrix

$$\overline{\rho(t)} = \rho(0) - i \left( \int_0^t dt' \frac{\Omega_{\text{eff}}}{2} [\sigma_x, \rho(t')] + \int_0^t dt' \frac{\alpha_W}{4} \underbrace{[\sigma_z, [\sigma_z, \rho(t')]]}_{\mathcal{L}(\sigma_z)\rho(t')} \right) \quad (2.37)$$

When differentiating this form one finally obtains a modified version of the initial equation with

$$\partial_t \overline{\rho(t)} = -\frac{i}{\hbar} [H_{\text{eff}}, \rho(t)] + \frac{\gamma_V}{2} \mathcal{L}(\sigma_z)\rho(t), \quad (2.38)$$

where we choose  $\gamma_V = \alpha_W/2$ . This relation was derived under the assumption of a driven two level system without a dephasing into of the dark state  $|D\rangle$  with rate  $\gamma_D$  or the decay of the Rydberg state via spontaneous emission. If these are taken into account the calculation becomes significantly more complicated. Assuming that the frequency noise impact on the Master equation is not correlated to the dephasing  $\gamma_D$  and or the spontaneous decay channels with rates  $\kappa$  or  $\Gamma$  all effects are combined into one

Lindblad master equation describing the development of the averaged density matrix as:

$$\begin{aligned} \partial_t \overline{\rho(t)} = & -\frac{i}{\hbar} [H_{\text{eff}}(t), \rho(t)] + (\kappa + \Gamma) \mathcal{L}[\sigma_{GW}] \rho(t) \\ & + \gamma_D \mathcal{L}[\sigma_{DW}] \rho(t) + \Gamma \mathcal{L}[\sigma_{GD}] \rho(t) + \gamma_\nu \mathcal{L}(\sigma_{WW}) \rho(t), \end{aligned} \quad (2.39)$$

where the zero-energy was chosen to be at the energy of the ground state  $|G\rangle$ . This allows to replace  $\frac{\gamma_\nu}{2} \mathcal{L}(\sigma_{WW} - \sigma_{GG})$  by  $\gamma_\nu \mathcal{L}(\sigma_{WW})$ , which is more convenient here.

To derive the term  $\gamma_\nu \mathcal{L}(\sigma_{WW})$  the frequency noise of the driving field was approximated by white noise, which allowed to neglect multiple terms in [Equation 2.36](#). However, the frequency noise spectra of the excitation lasers are not necessarily flat, but have distinct noise features. Therefore, the Master equation in [Equation 2.39](#) is an approximation of the experimental measurement and does not resemble the dynamics of the superatom exactly.

---

## Experimental Setup Creating Rydberg Superatoms

---

As discussed in [Chapter 2](#) the coherent interaction between few photons and the Rydberg superatom is limited by different dephasing mechanisms. Our experimental apparatus allows us to investigate these dephasing mechanisms.

In this section, I outline the experimental setup and the methods to capture and prepare a cloud of ultracold Rubidium-87 atoms in the RQO experiment. Then I will describe the experimental realization of Rydberg superatoms and the techniques used to investigate them. This includes a description frequency stabilization scheme used for the lasers driving the excitation of the Rydberg states.

### 3.1 Experimental Apparatus and Atom Preparation Cycle

The RQO experiment consists of a glass cell connected to a vacuum chamber with an ion pump to preserve a vacuum pressure of  $\sim 1 \times 10^{-10}$  mbar. Using current-controlled dispensers a background gas of Rubidium-87 is created in the chamber. The atoms are loaded and prepared from this background gas using the light beams shown in [Figure 3.1](#).

In the first step, a cloud of Rubidium atoms is trapped and cooled from the background gas by using a *magneto-optical trap* (MOT) for  $\sim 1.3$  s. The MOT is realized using 6 circularly polarized laser beams driving the  $F = 2 \rightarrow F' = 3$  transition (the beams in the z-direction are not shown in the sketch) and three sets of coils aligned to the axes x, y and z in the anti-Helmholtz configuration. Each MOT-beam is overlapped with a *repumper*-beam driving the  $F = 1 \rightarrow F' = 2$  transition. Due to imperfections in the cooling cycle a part of the atoms decays in the  $F = 1$ -state, which cannot be excited by the MOT beams.

To increase the atomic density the atoms are transferred into an optical dipole trap [\[49\]](#). [Figure 3.1](#) shows the two crossing beams (ODT) with a wavelength of 1064 nm a power of  $\sim 12$  W and an angle of  $31.4^\circ$ . Both beams have opposite linear polarization to prevent interference and thus the formation of an optical lattice. To transfer the atoms from the MOT to the ODT the magnetic fields are ramped up for 100 ms and the detuning MOT cooler beams and the repumper beams is reduced to compress the cloud. Simultaneously the power of the MOT and repumper is linearly ramped down such that the atoms are then trapped by the optical dipole trap.

To reduce the temperature of the atomic cloud the power of the ODT beams is reduced, lowering the trap depth and cooling the atomic ensemble via evaporative cooling [\[50\]](#). This is combined with

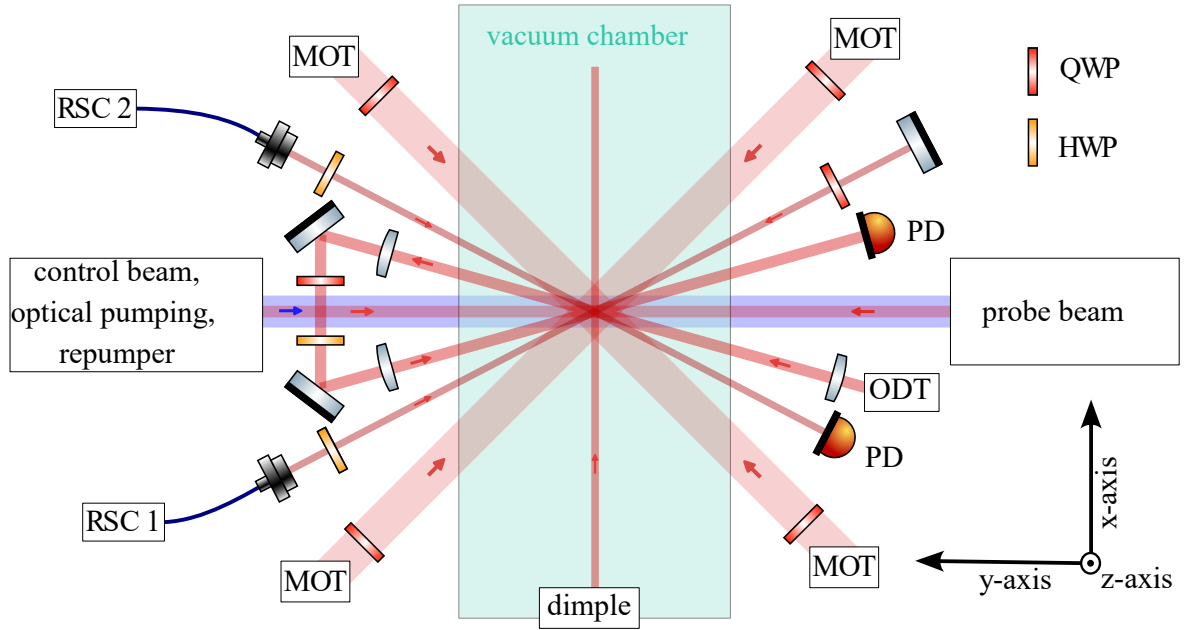


Figure 3.1: A sketch of the vacuum chamber (light blue) with the optical beams used in the RQO experiment. The beams depicted here are from the magneto-optical trap (MOT), the optical lattice used for Raman-sideband-cooling, the optical dipole trap (ODT) and the dimple beam. On the main experimental axis (y-direction) the beam of the repumper, the optical pumping beam (both red) are overlapped with the control beam (blue) while the probe counterpropagates these beams. Around the glass cell magnetic coils are installed to compensate stray magnetic fields and apply well-defined magnetic bias fields in a given direction (for MOT, optical pumping etc.). Not shown in this sketch are the beams going in the z-direction (MOT and polarizer). Neither are the beams for vertical and horizontal absorption imaging (x- and z direction) Adapted from [48].

simultaneous Raman-sideband-cooling (RSC) to further reduction of temperature: An optical lattice with three beams is realized (see RSC beams in Figure 3.1) and a magnetic field is applied such that Zeeman splitting corresponds to the splitting of the vibrational states in the lattice. By using an additional “polarizer” beam driving the  $F = 1 \rightarrow F' = 0$  transition the vibrational state is reduced, cooling the atoms beyond the Doppler-limit. In combination with the evaporative cooling in the optical dipole trap the atoms can be cooled to temperatures as low as  $\sim 3 \mu\text{K}$  (a more detailed description can be found in [48]).

To create a small atomic ensemble that can be fully blockaded (to later create Rydberg superatoms), the crossed dipole trap is overlapped with a dimple trap consisting of a single Gaussian beam. The direction of this “dimple” is perpendicular to the long axis of the atomic cloud in the crossed trap (see Figure 3.1). Then, by ramping up the power of the dimple beam and simultaneously ramping down the power of the beams of the optical dipole trap the atoms are transferred into the dimple trap. Atoms that are not in the overlapping region escape due to their kinetic energy such there are no atoms around the trapped cloud. Afterward, the dimple is ramped back down to half of the initial power resulting in a trap depth of  $\sim 250 \mu\text{K}$ , while the ODT is turned back on to confine the atomic cloud in the y-direction (the trap depth is approximately  $160 \mu\text{K}$ ).

As a last step in the preparation cycle, the atoms are transferred into  $|5S_{1/2}, F = 2, m_F = 2\rangle$  by applying the *optical pumping* beam that is resonant with the  $F = 2 \rightarrow F' = 2$  and  $\sigma^+$  polarized.

To define a quantization axis a magnetic bias field along the  $y$ -direction is applied. Additionally, the “repumper” beam is used to depopulate the  $F = 1$  state. Finally, the atoms are fully prepared, cooled and confined enough to conduct superatom experiments.

## 3.2 Measuring and Evaluating Rabi Oscillations of Rydberg Superatoms

After the preparation the atomic cloud is probed in 1000 consecutive experiments each lasting  $100 \mu\text{s}$ . Afterward, the trapping beams are turned off releasing the trapped atoms and 1000 reference measurements without an atomic cloud are conducted.

In each experiment the atomic cloud is illuminated with the light of the counterpropagating red probe laser (780 nm) and the blue control laser (480 nm) (see [Figure 3.1](#)). The single-photon detuning of the probe beam is  $\Delta_p = 100 \text{ MHz}$  and the two-photon detuning is chosen to be  $\delta = 0 \text{ MHz}$  such that the condition for adiabatic elimination is fulfilled. The control laser has a Rabi frequency of  $\sim \Omega_c = 12 \text{ MHz}$ , while the light coming from the Probe laser is strongly attenuated typically to a rate of  $R_{\text{in}} \sim (10 - 30)$  photons per  $\mu\text{s}$ .

To perform a measurement, the optical dipole trap is turned off to reduce the differential light shift while the atoms are illuminated with the control light. With an Acusto-optic modulator a Tuckey-pulse with a length of  $\sim 8 \mu\text{s}$  of probe photons is created to illuminate the atoms (see gray trace [Figure 3.2](#)). Ideally, one would like to use a square pulse to drive the system with a single Rabi frequency. However, since sharp edges in the time domain correspond to a broadening in the linewidth of the probe laser in the frequency domain, a Tuckey-pulse with more rounded edges was chosen. The transmitted light is coupled into an optical fiber and the measured with Single-Photon-Counting-Modules (SPCMs), with the temporal resolution set to  $\sim 20 \text{ ns}$  (color trace in [Figure 3.2](#)). After that the optical dipole trap is turned back on to counteract a dissipation of the atomic cloud in the  $x$ -direction.

After 1000 of these experiments the dimple and the optical dipole trap are turned off for 15 ms causing the atomic cloud to fully dissipate due to gravitation and the kinetic energy of the atoms. Without atoms in the trap 1000 reference measurements are done with the same procedure measuring the transmission of the probe laser are done.

Normally, these experiments are performed for multiple probe photon rates  $R_{\text{in}}$  each resulting in a different trace due to the different Rabi frequency  $\Omega_{\text{eff}} = 2\sqrt{\kappa R_{\text{in}}}$ . The procedure of preparing the atoms and then performing the experiment measuring the probe transmission is then repeated for each of the probe laser powers separately. For typical measurements, like presented in [Figure 3.2](#), one averages across of  $3500 * 1000$  to  $5000 * 1000$  experiments.

After averaging over the experiment and reference measurement one obtains the plots shown in [Figure 3.2](#). The Rabi oscillations are fully characterized by the rates  $\kappa$ ,  $\Gamma$ ,  $\gamma_D$  and  $\gamma_v$  from [Equation 2.39](#). Thus, one can fit a function of the form

$$R_{\text{out}} = |E(t)|^2 = R_{\text{in}}(t) + \kappa \langle \sigma_{GW}^\dagger(t) \sigma_{GW}(t) \rangle - i\sqrt{\kappa} \left[ \sqrt{R_{\text{in}}(t)} \langle \sigma_{GW}(t) \rangle - \sqrt{R_{\text{in}}(t)} \langle \sigma_{GW}^\dagger(t) \rangle \right]. \quad (3.1)$$

where the measured reference field pulses are inserted as  $R_{\text{in}}(t)$ , to the measured oscillation traces. The time-dependent correlation terms  $\sigma_{GW}^\dagger(t)$  and  $\sigma_{GW}(t)$  are calculated from the Lindblad Master equation using QuTip [37]. To increase the accuracy of the fit, the measurements with different probe photon rates are fitted with the same  $\kappa$ ,  $\Gamma$  and  $\gamma_D$  since these rates are expected to be independent of the input

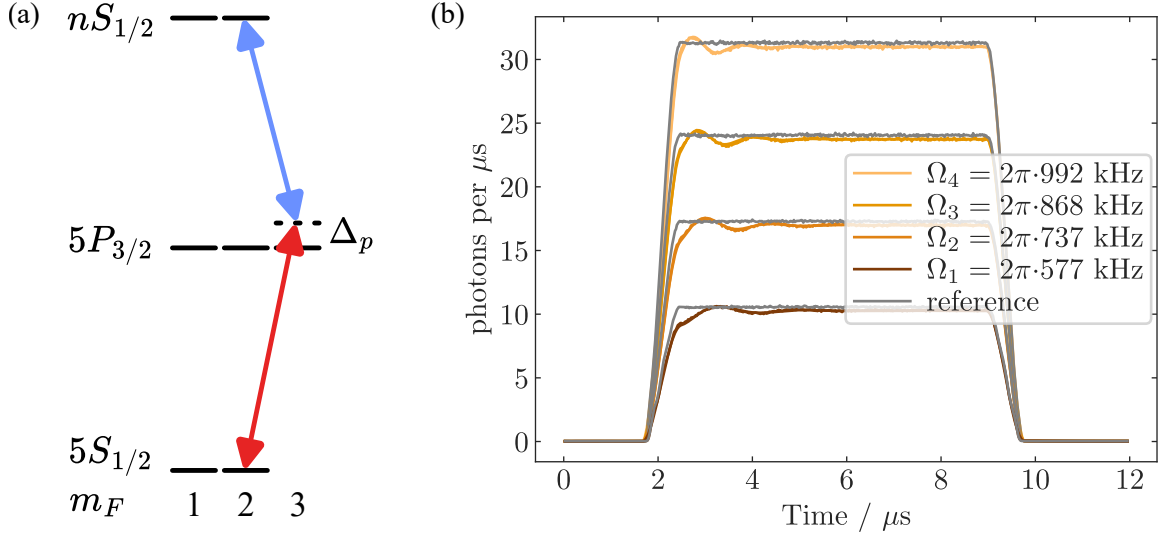


Figure 3.2: Two-photon excitation scheme and example of a Rabi oscillation measurement performed in the RQO experiment for four different probe photon rates  $R_{\text{in}}$ . (a) Simplified level-scheme of Rubidium-87 used in the experiment. Here only the hyperfine levels with a positive magnetic quantum number are shown. The transition driven by the  $\sigma^+$ -polarized probe is depicted in red and the transition driven by the  $\sigma^-$ -polarized control is depicted in light blue. The detuning of the probe light is denoted between the transition  $|5S_{1/2}\rangle \rightarrow |5P_{3/2}\rangle$  and the laser frequency is denoted as  $\Delta_p$ . (b) The transmitted probe light is measured for the case with (colored) and without (gray) a superatom in the probe beam path. The different Rabi frequencies are calculated from the height of the reference pulses using  $\Omega = 2\sqrt{\kappa R_{\text{in}}}$ . To each of the recorded traces a function was fitted of the form of Equation 3.1. The fit has the following parameters  $\kappa = 0.31(1)$  MHz,  $\Gamma = 0.42(1)$   $1/\mu\text{s}$ ,  $\gamma_D = 0.91(4)$   $1/\mu\text{s}$ ,  $\gamma_{v1} = 0.78(9)$   $1/\mu\text{s}$ ,  $\gamma_{v2} = 0.89(8)$   $1/\mu\text{s}$ ,  $\gamma_{v3} = 1.27(8)$   $1/\mu\text{s}$  and  $\gamma_{v4} = 2.13(9)$   $1/\mu\text{s}$ .  $\gamma_{v1}$  corresponds to the case with the lowest input photon-rate  $R_{\text{in}}$  and  $\gamma_{v4}$  corresponds to the case with the highest input photon rate.

rate of photons  $R_{\text{in}}$ . Since it is expected that the dephasing  $\gamma_v$  induced by the frequency noise of the laser depends on the characteristics of the driving field (see Equation 2.37). Each trace is fitted with an individual value for  $\gamma_v$ .

The fitting parameters of the measurement in Figure 3.2 suggest that the frequency noise induced dephasing has a rate between  $0.78(9)$   $1/\mu\text{s}$  and  $2.13(9)$   $1/\mu\text{s}$  depending on  $R_{\text{in}}$ . The fit indicates that frequency noise of the excitation lasers contributes significantly to the dephasing of Rabi oscillations. However, it could also be that another unknown power-dependent effect is measured here. This will be quantitatively investigated in Chapter 5.

### 3.3 Two-Photon Excitation Laser System

In this section, the setup of the probe and the control laser is described in detail. The optical and electronic setup determines the frequency noise characteristics of both lasers.

The probe laser is an external cavity diode laser operating at 780 nm with an optical isolator to prevent back-reflections. The control laser also has an external cavity diode laser operating at 960 nm, which is then amplified with a tapered amplifier. Afterward, the light is frequency-doubled using second harmonic

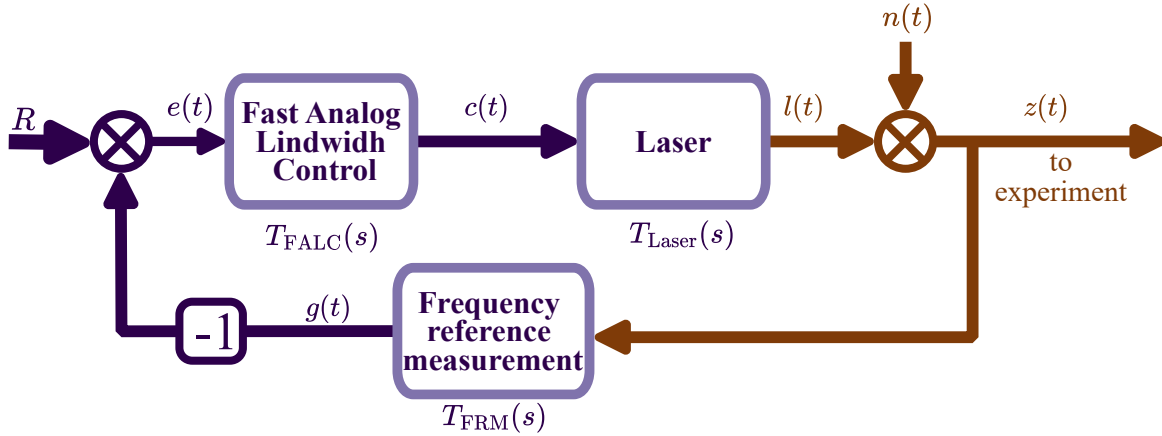


Figure 3.3: Simplified sketch of probe or control laser fast stabilization loop. The boxes indicate the controller (Fast Analog Linewidth Control), the actuator (Laser) and the sensor (Frequency reference measurement) with the transfer function of the respective component denoted by  $T(s)$ . Arrows indicate the electrical (dark purple) or optical (brown) signals sent through the different components. The trace of each signal is labeled with small letters ( $e(t)$ ,  $g(t)$ ,  $c(t)$ ,  $l(t)$  and  $z(t)$ ). The error signal  $e(t)$  is calculated from the difference between the set point  $R$  (typically 0) and the sensor output  $g(t)$ . In this sketch, the only noise source is considered the intrinsic frequency noise of the laser  $n(t)$ , which is added to the output signal of the resulting from the modulation of the laser current modulation.

generation transforming wavelength to 480 nm.

To suppress changes in the laser frequency, the probe and the control laser are frequency stabilized to a reference, respectively. A feedback loop minimizes the difference between the laser frequency and the reference frequency. The changes in the difference range from slow drifts over hours or days to fast changes on the time-scales of the experiment. Figure 3.3 shows the scheme for frequency stabilization against fast changes in the frequency, which are relevant for the frequency noise induced dephasing  $\gamma_D$ . The light coming out of the laser is compared to a frequency reference. In the case of the control laser the Pound-Drever-Hall method is used stabilizing the laser to an ultra-low expansion cavity [51]. The probe is stabilized by using the beat note with a stabilized *master laser* [52]. The reference measurement creates an error signal which increases linearly with a deviation in the laser frequency from the reference frequency.

The error signal is used as an input to a Fast Analog Linewidth Control (FALC by *TOPTICA*), which generates two output signals used to apply feedback to the laser: A (slow) *Unlimited Integrator Output* signal is used to offset slow drifts in the laser frequency by modulating the voltage of piezo changing the length of the external cavity  $L$  (not shown in Figure 3.3). The *Main Output* provides feedback on the current supplied to the laser diode to compensate for fast changes in the frequency. Since for the dephasing of single-photon Rabi oscillations only fast changes in the frequency are relevant, we will focus on these in the following.

Each component in the fast feedback loop has an individual complex transfer function  $T(s)$  characterizing the relation between an in- and an output signal  $x(t)$  and  $y(t)$  of each component. The transfer

function is defined via the Laplace transform as [53]

$$T(s) = \frac{Y(s)}{X(s)} \quad (3.2)$$

$$X(s) = \int_0^{\infty} e^{-st} x(t) dt \quad (3.3)$$

$$Y(s) = \int_0^{\infty} e^{-st} y(t) dt, \quad (3.4)$$

where  $x(t)$  and  $y(t)$  are the in- and output signals in the time domain. The parameter  $s$  is a complex number. The real part of  $s$  describes how fast the signals  $x(t)$  and  $y(t)$  decay in time and the imaginary part describes the frequency with which  $x(t)$  and  $y(t)$  oscillate in time. The transfer function is complex valued characterizing not only the amplitude relation between an in- and an output signal but also their phase relation.

Each component of the feedback loop introduces noise, disturbing the frequency stabilization. The noise can either be electronic noise or noise in the laser frequency. For the analysis presented in this thesis, the intrinsic laser frequency noise ( $n(t)$  in Figure 3.3) is dominating all electronic noise and can therefore be considered the only source of noise in the feedback loop. In the following, the components of the feedback loop will be introduced and their impact on the feedback loop performance is analyzed.

### 3.3.1 Fast Analog Linewidth Control

The Fast Analog Linewidth Control (FALC) is the main tool to tune the response of the feedback loop to keep the frequency constant at the set point producing a steady state in the laser frequency.

The input of the controller is an electrical error signal  $e(t) = g(t) - S$  which is the difference between the measured frequency signal  $g(t)$  and the set point  $S$  (see Figure 3.3). To produce the output signal based on the input signal, the controller uses three fundamental components: Proportional amplifiers, Integrators and Differentiators. These will be introduced in their most basic form here:

A proportional amplifier amplifies the input error signal  $e(t)$  producing an output signal of the form [53]

$$u_p(t) = k_p \cdot e(t) \quad (3.5)$$

where  $k_p$  is the amplifier gain which also defines the transfer function  $T_p = k_p$ . If a feedback loop is realized with a proportional amplifier only it is not capable of achieving a steady state with  $e(t) = 0$  (see [53]).

An integrator is capable of reducing such offsets in the error signal by integrating the error signal over time [53]

$$u_i(t) = k_i \int_0^t e(\tau) d\tau \quad (3.6)$$

The transfer function of an Integrator is given by  $T_i = k_i/s$ , where  $s$  denotes the variable defined in the Laplace Transform (see Equation 3.4) [53]. If one feeds a sinusoidal signal into an integrator the output signal will be delayed by  $90^\circ$ . Therefore, an Integrator produces a lag in the output phase relative to the input phase.

|      | Control |         |     | Probe   |         |     |
|------|---------|---------|-----|---------|---------|-----|
|      | $f_1$   | $f_2$   | $K$ | $f_1$   | $f_2$   | $K$ |
| XSLI | -       | -       | 1   | -       | -       | 1   |
| SLI  | 2.4 kHz | 140 kHz | 1   | 1.1 kHz | 65 kHz  | 1   |
| FLI  | 6.5 kHz | 80 kHz  | 1   | -       | -       | 1   |
| FLD  | 1 MHz   | 190 kHz | 5   | 1 MHz   | 190 kHz | 5   |

Table 3.1: Set corner frequencies of the Main branch of the Fast Analog Linewidth Control of the probe and the control laser. Plugging these values into Equation 3.8 will lead to the transfer functions of each component. Entries denoted with “-” indicate that the corresponding component was disabled.

As the third component, the Differentiator produces an output signal depending on the derivative of the error signal [53]

$$u_d(t) = k_d \frac{de}{dt} \quad (3.7)$$

with a transfer function  $T_d = k_d \cdot s$ . Here the differentiation leads to an advance in the phase of  $90^\circ$  in the output signal.

If one combines a differentiator and an integrator, one can create a lead-lag or a lag-lead compensator which have a transfer function of the form [54]

$$T_s = K \frac{f_2 + s}{f_1 + s} \quad (3.8)$$

where  $K$  is the overall gain of the controller stage.  $f_1$  and  $f_2$  are the corner frequencies determining which noise signals are amplified/attenuated. If one chooses  $f_1 < f_2$  one obtains a lag-lead compensator which has a high gain for low frequencies and produces a phase lag. In the opposite case, one gets a lead-lag filter, which has a high gain for high frequencies and produces a phase lead.

The *Fast Circuit Branch* of the Fast Analog Linewidth Control consists of three Lag-Lead compensators and one Lead-Lag compensators connected in line with each other: An *Extra Slow Limited Integrator* (XSLI), a *Slow Limited Integrator* (SLI), a *Fast Limited Integrator* (FLI) and a *Fast Limited Differentiator* (FLD). Each of these components is supposed to be used for different, yet overlapping, frequency ranges, such that a broad range of fluctuations can be compensated for (see Figure 3.4) [55].

*Limited* means here that the controllers are integrating only over a limited period of time, which prevents the controller from doing a *windup*. This occurs if the controller runs into one of its output boundaries and then integrates the saturated error signal [53].

By adjusting the corner frequencies  $f_1$  and  $f_2$  of each component, one can tune the overall transfer function of the controller. Table 3.1 shows the corner frequencies set in the Fast Analog Linewidth Control of the probe and the control Feedback loop. Figure 3.4 shows the transfer functions of the components of the controllers of the probe and control feedback loop for these settings in a Bode Plot. Such a Bode plot shows the amplitude and the phase relation between the in- and the output signal plotted against the frequency of the input signal. One can see there how the amplifications and induced phase leads or lags are summing up leading to the total transfer function of the controller. One can see the three lag-lead filters have a high gain at low frequencies, while the Fast Limited Differentiator compensates for fluctuations in the high frequency regime. The total transfer function of the controller is

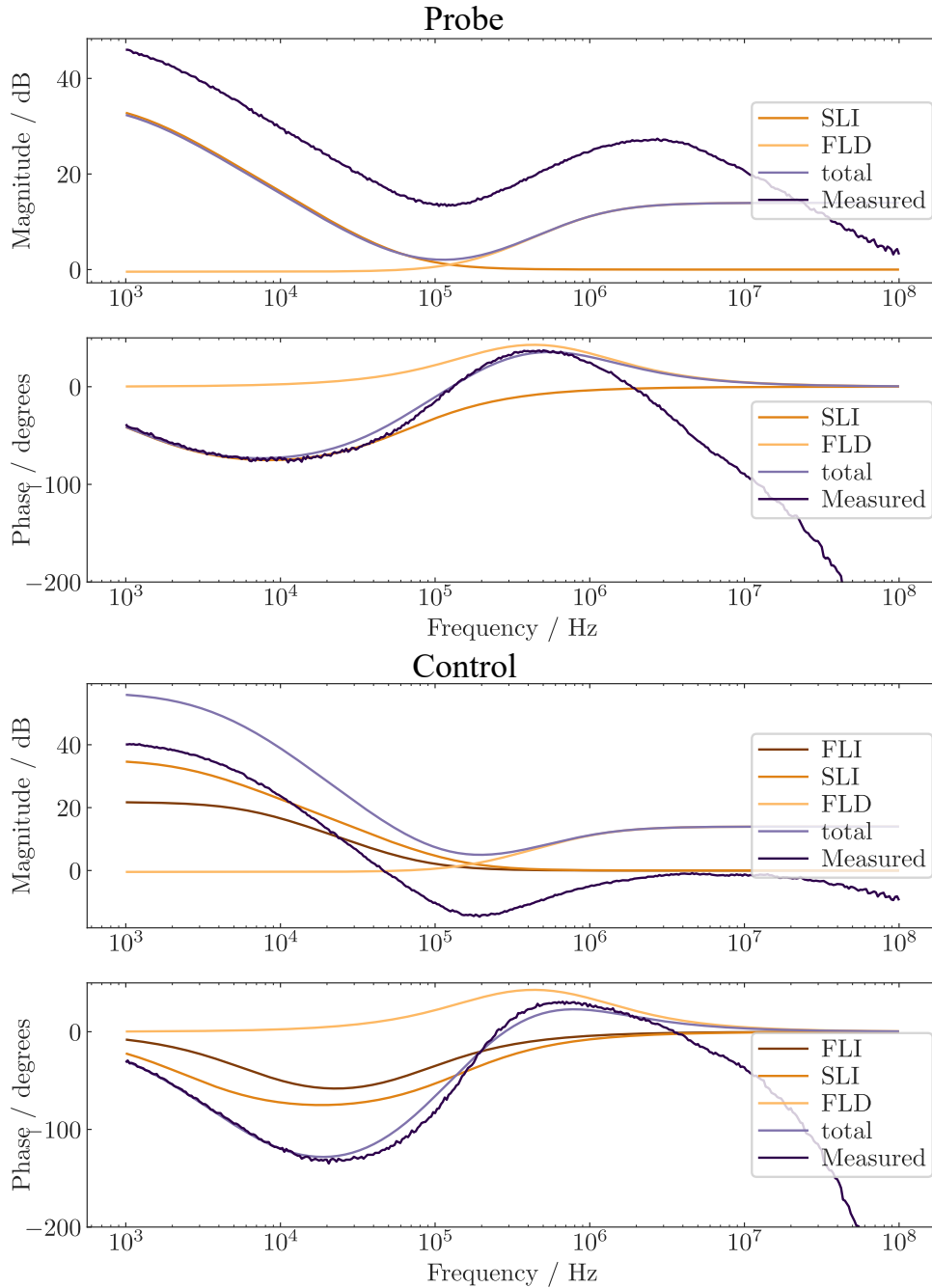


Figure 3.4: Bode plots of the open loop transfer function of the Fast Analog Linewidth Control of the probe and control laser for the settings from [Table 3.1](#). The transfer functions of the Extra Slow Limited Integrator (XSLI), Slow Limited Integrator (SLI), Fast Limited Integrator (FLI) and the Fast Limited Differentiator (FLD) were calculated using [Equation 3.8](#) to produce the phase and amplitude relation between in- and output of each component. Transfer functions of components that were turned off are not plotted. The total transfer function (light purple) was calculated from the product of the component transfer functions. The transfer function was measured by doing an open-loop network measurement of the (fast) Main Branch. The difference in magnitude between the measured and calculated curves results from an additional amplifier in the FALC. The limited bandwidth of the controller is visible as a drop in magnitude and phase towards higher frequencies in the network measurement. In the calculation the limited bandwidth of the controller was neglected.

the product of the transfer function of the components.

To quantify the calculated total transfer function of the FALC, the transfer function of the controller was experimentally measured performing a network measurement. In a network measurement a monochromatic RF-signal is fed into the device to be analyzed (here the FALC) and the output signal of the device is measured. By comparing the in- and the output signal of the controller, phase and the amplitude relation can be obtained. Varying the frequency of the input signal produces the Bode plots of interest.

To perform the measurement, the signal coming from the network analyzer was fed into the main input of the controller and the signal from the controllers main output is fed back into the network analyzer. Comparing the calculated and the measured responses in [Figure 3.4](#) of the FALC controllers, one can see that they are in good agreement. In the calculation, the input amplification and the main gain affecting the output signal were not taken into account, which just shifts the gain profile up and down and has no impact on the phase relation. This is similar to the transfer function of a proportional amplifier which is independent of  $s$ . For frequencies beyond 1 MHz, one can see that the measured and the calculated curves for the amplitude and the phase relation differ significantly. This is due to the limited bandwidth of the controller, which is expected to be  $\sim 10$  MHz. Thereby, the feedback loop has an upper frequency limit where it can compensate.

The second *Unlimited Integrator Output* is used to offset slow drifts in the frequency e.g. due to slow changes in the ambient temperature. In the feedback loop this branch controls the voltage applied to the piezo crystal with the Bragg reflector. This branch consists of an integrator (see [Equation 3.6](#)) and amplifiers. This branch has a significantly higher DC gain (up to 110 dB) to reset the integrators in the fast branch to 0 once the Unlimited Integrator has settled [55]. It is not possible to perform a network measurement of the slow branch since the integrator is too slow and one would measure the integrator windup.

With the dual branch approach, the controller is capable of compensating for slow drifts as well as fast fluctuations of the laser frequency.

### 3.3.2 External Cavity Diode Lasers

The probe and the control laser are both external cavity diode lasers (ECDLs) by *TOPTICA*. [Figure 3.5\(a\)](#) shows a sketch of the laser diode unit which is similar in both lasers: The laser diode supplied with a current emits light that forms a standing wave inside the semiconductor active medium. Thus, the diode itself works as a cavity filtering the wavelength of the light emitted (internal mode) [56]. The light passes through an anti-reflection coated window and then falls on a blazed grating mounted on a piezo crystal. The angle of the blazed grating tuned such that the -1st order is reflected into the laser diode. The wavelength can be tuned with the angle of the blazed grating and can thus be used to tune the wavelength of the emitted light. The light that is reflected back into the laser diode is reflected by the back facet of the laser diode and forms another cavity with length  $L$  (external mode).

[Figure 3.5 \(b\)](#) shows a sketch of the overall emission profile of an ECDL, which is the product of the internal mode, external mode, grating mode and the medium gain, which is almost flat in comparison to the other modes. The overall gain of the laser is chosen that it is  $> 1$  for exactly one laser line such that a single mode is emitted.

By tuning the position of the different modes, the wavelength of the emitted light can be controlled. To tune the external mode, which offers the finest resolution in frequency, one can change the voltage supplied to the piezo to change the length  $L$ . Additionally, one can change the current applied to the

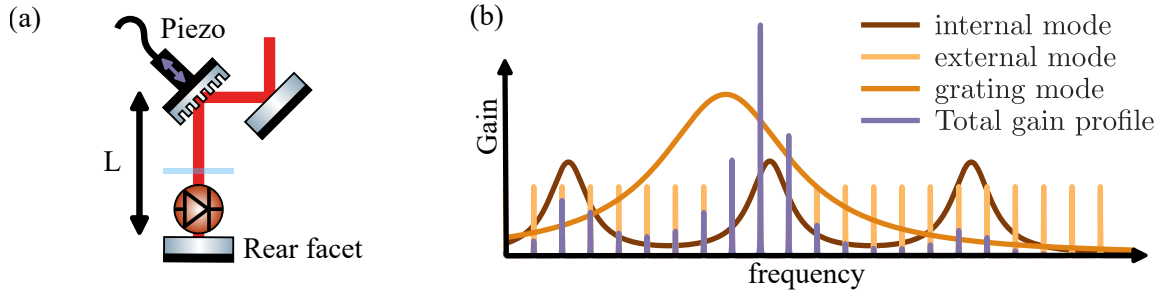


Figure 3.5: Simplified sketch of Probe/Control laser setup and the laser gain profile. (a) Sketch of the laser diode setup used in the probe and the control laser. The laser diode (brown bulb) emits light that forms a standing wave inside the laser diode (internal mode). The light falls on the blazed grating, with the -1st order being reflected (grating mode) in the laser diode. The 0-th reflection order is reflected by the internal mirror can then be used in the experiment or be further amplified by e.g a tapered amplifier. (b) Sketch of the gain profile of the external cavity diode laser by *TOPTICA* in arbitrary units. The angle of the grating defines the grating profile has a width of  $\sim 50$  GHz. The formation of standing waves in the diode laser medium defines the internal modes with a separation of  $\sim 64$  GHz and a width of 20 GHz. The cavity formed by the grating and the rear facet provides the finest selection of the laser frequency with a separation of 9 GHz. Not drawn in the sketch is the gain profile of the laser medium which has a width of  $\sim 5000$  GHz. The total gain profile is calculated as a product of the individual gain profiles. Widths of the gain profiles are taken from [58]

laser diode tuning the refractive index in the diode medium or change the temperature of the laser diode, which also tuning the length of the diode medium [56, 57].

As the external cavity has the finest resolution, one could try tuning the laser by only changing the voltage controlling the piezo crystal. However, if the voltage is tuned too far, the carrier peak of the external cavity is shifted to a lower gain due to the internal mode and another peak is shifted to the center of the gain profile. The laser frequency rapidly changes towards the peak in the center of the internal mode. The sudden change in the frequency is commonly referred to as a *mode-hop*. The frequency range across which the laser can be tuned without a mode-hop occurring is called the *mode-hop-free tuning range* [57].

To increase the mode-hop-free tuning range the probe and the control laser have a feed-forward implemented, which adjusts the current of the diode if the voltage applied to the piezo crystal is changed [58]. With the feed-forward, the probe laser has a mode-hop-free tuning range of 30 GHz and the control laser has a mode-hop-free tuning range of 20 GHz.

In the case of a feedback loop as shown in Figure 3.3, the only source of noise is the intrinsic laser frequency noise  $n(t)$  of the laser diode. For any type of laser, the fundamental limit for the linewidth is given by the Shawlow-Townes-Limit [59]

$$\Delta\nu_{\text{laser}} = \frac{4\pi h\nu_0(\Delta\nu_{\text{ec}})^2}{P_{\text{out}}} \quad (3.9)$$

where  $\nu_0$  denotes the laser frequency,  $h$  is the Planck constant,  $\Delta\nu_{\text{ec}}$  is the full width at half maximum of the external cavity and  $P_{\text{out}}$  is the output power of the laser. The white noise results from spontaneous emission inside the laser medium and linear losses in the external cavity [60].

In a diode laser, the noise is normally overshadowed by  $1/f$ -noise or *flicker noise* in the frequency range up to 1 MHz [61]. The flicker noise originates from the discreteness of charge carriers in the

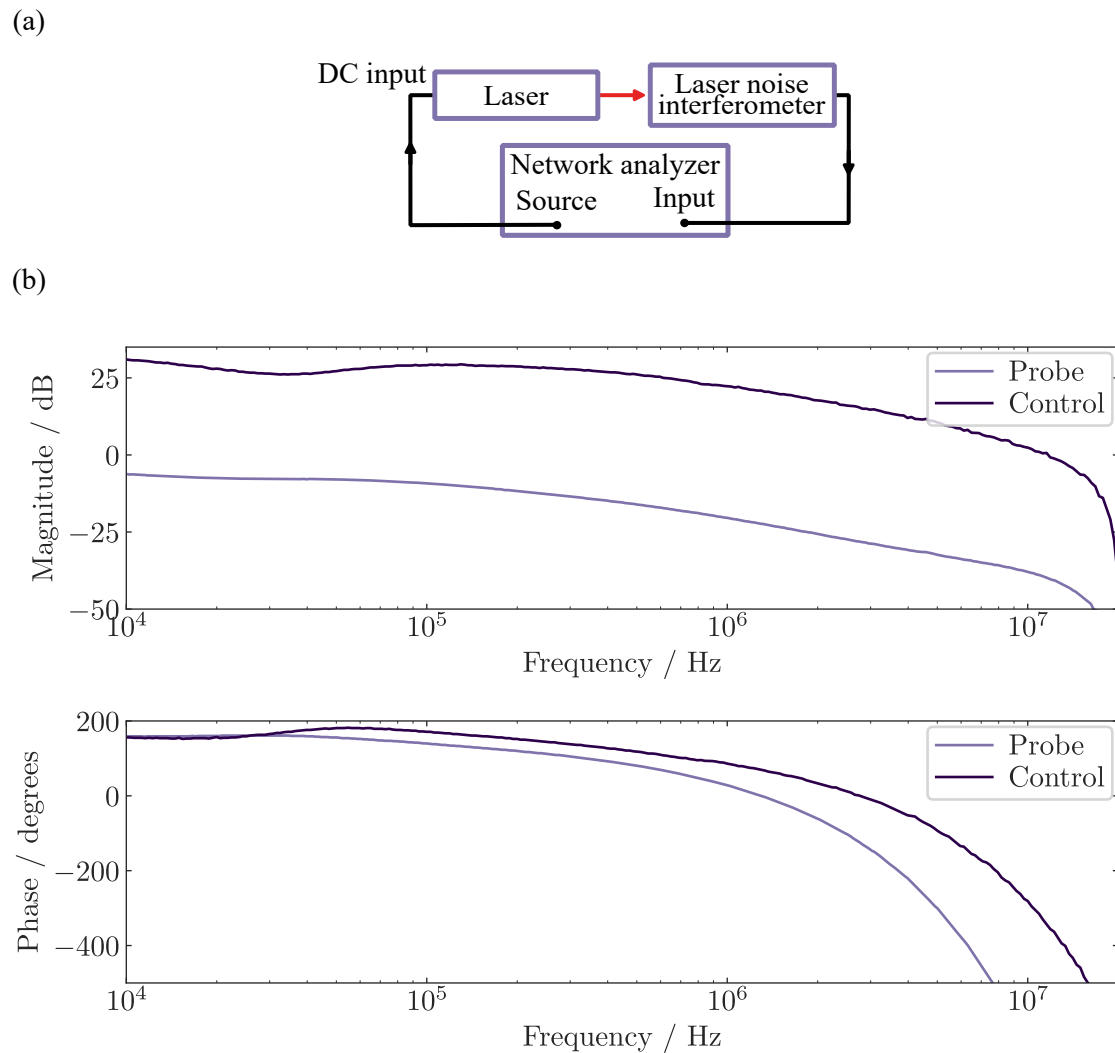


Figure 3.6: Open-loop Bode plots of the probe and the control laser. (a) Measurement setup for the open loop measurement. The source output of the network analyzer is connected to the DC input of the laser and the laser light is analyzed with the interferometer explained in [Chapter 4](#). The signal measured with the interferometer is sent back into the network analyzer. (b) Bode plot of the open loop transfer function of the probe and control laser.

semiconductor of the laser diode. The presence of charge carriers affects the refractive index in the gain medium which causes a fluctuation in the frequency [62–64].

Additionally, the electronic components of the laser and outer disturbances can cause noise in the laser frequency. Because drifts in the laser diode temperature induce a change in the laser frequency, the probe and the control laser have an internal feedback loop stabilizing the temperature of the diode.

To analyze the response of the probe and control laser to externally applied feedback the open loop transfer function is measured. [Figure 3.6\(a\)](#) shows the measurement setup: the network analyzer modulates the diode current via the AC input of the laser and the response is measured using a laser noise interferometer. The interferometer setup will be introduced in detail in [chapter 4](#). The cable from

the interferometer is terminated with a  $50\ \Omega$  resistor to prevent cable reflections.

Figure 3.6(b) shows the Bode plot of the response of the probe and the control laser. Comparing the amplitude relation between the signal sent into the laser and the measured response it can be observed, that the control Bode plot has a hump at around 50 kHz. In contrast to that the amplitude of the measurement with the probe laser is steadily decreasing for higher frequencies. In the FALC such a hump in the Bode plot was caused by a Lead-Lag-filter. The sharp drop in the measured amplitude beyond 10 MHz is due to the suppression effect of the interferometer (see Figure 4.8). When looking at the phase relation in the Bode plot, one notices that for low frequencies the phase of the probe and the control laser match. At around 50 kHz the phase of the control increases, which shows that there is an internal phase-lead built into the control laser. Compared to the FALC controllers of both lasers, the lasers themselves introduce a significant phase lag into the feedback circle. Therefore, the lasers do contribute to the limited bandwidth of the feedback loop.

### 3.3.3 Frequency Reference Measurements of the Probe and Control Laser

The control laser is stabilized using an Ultra Low Expansion (ULE) cavity from *Stable Laser Systems* using a Pound-Drever-Hall signal [51]. This cavity has a linewidth of  $\sim 75$  kHz and its transmission peaks are drifting by  $\sim 21$  kHz per day. A small fraction of the light coming from the laser diode with the frequency  $\omega_0$  is coupled into an optical fiber with a fiber EOM. For the RF-input of the fiber EOM two signals are being mixed: A signal with frequency  $\Omega = 25$  MHz coming from the control laser control unit and a signal from an RF-generator with the frequency  $\omega_{\text{RF}}$  (in the case of the  $108S_{1/2}$  Rydberg state this was 279 MHz) to shift the carrier frequency onto a cavity peak. The signal  $\Omega = 25$  MHz is used to modulate small sidebands on the carrier of the laser light. The transmission of the EOM then has in total three sets (separated by the RF-frequency) of a carrier peak with the power  $P_c$  and two small sidebands with the power  $P_s$  with a separation of  $\Omega$ .

For the lock, the carrier with the lowest or the highest frequency sidebands at  $\omega_l = \omega_0 \pm \omega_{\text{RF}}$  are used. The light is then sent into the cavity and the back reflection is recorded on a photodiode. The measured reflected signal is then fed back into the laser control unit, where it is mixed with the 25 MHz-signals that created the small sidebands which creates the Pound-Drever-Hall signal. A detailed explanation of the mixing procedure leading to the desired error signal can be found in [51]. The error signal  $\epsilon$  depends on the frequency  $\omega_l$  of the sideband as [51]

$$\epsilon(\omega_l) = -2\sqrt{P_c P_s} \text{Im}\{F(\omega_l)F^*(\omega_l + \Omega) - F^*(\omega_l)F(\omega_l - \Omega)\} \quad (3.10)$$

$$F(\omega) = \frac{r(\exp\{i\frac{\omega}{\Delta\nu_{\text{FSR}}}\} - 1)}{1 - r^2 \exp\{i\frac{\omega}{\Delta\nu_{\text{FSR}}}\}} \quad (3.11)$$

where  $r$  denotes the reflectivity of the cavity mirrors and  $\Delta\nu_{\text{FSR}}$  denotes the Free Spectral Range of the cavity. This signal has a steep slope at multiples of the Free Spectral Range  $N \cdot \Delta\nu_{\text{FSR}}$  and can therefore be used to stabilize the frequency of the laser. The mixing of the RF signal allows shifting the Pound-Drever-Hall signal freely relative to the cavity peaks.

The probe laser is locked to the master laser, which itself is locked to the same ULE cavity as the control laser using a Pound-Drever-Hall signal. To generate an error signal, a small part of the probe laser light is split off and shifted with an acusto-optic modulator by 80 MHz. The shifted probe light is overlapped with a part of the light from the master laser and the beat is detected with a fast photodiode.

As the photodiode cannot resolve THz frequencies, the measured signal consists of a constant offset and a term oscillating with the frequency difference  $\omega_d$  between the light of the probe and the master laser [52]. The beat signal is processed in a digital phase frequency detector that compares the beat frequency to a reference RF-signal. Depending on the sign of  $\omega_d$ , the digital phase frequency detector gives out a positive or negative digital signal, which after being sent through a low-pass filter can be used as an error signal.

### 3.3.4 Closed Loop Transfer Function of the Feedback Loop

If one wants to calculate the response of the complete feedback loop to noise introduced to the laser, one has to compute the *Closed Loop Transfer Function*. In a closed feedback loop the phase relation between the noise and the response of the feedback loop is crucial. In the optimal case the feedback loop counteracts the noise signal causing optimal compensation. In this thesis, this will be referred to as zero phase delay. As it was shown in Figure 3.4 the phase delay depends on noise frequency due to the limited bandwidth of the components. If the phase delay is at  $180^\circ$  the noise signal and the feedback loop response are exactly in phase. To prevent the feedback loop from amplifying the high-frequency noise components leading to resonant behavior of the system the gain is chosen to be smaller than one before a phase delay of  $180^\circ$  is reached [53, 65].

Mathematically, the closed loop transfer function depends on what is considered as the in- and the output signal (see Figure 3.3).

In the following the dependence of the output signal  $z(t)$  on a fluctuation of the laser frequency due to its intrinsic noise is described. Both are connected via  $y(t)$

$$z(t) = n(t) + y(t). \quad (3.12)$$

Using the linearity of integrals, one can derive the same relation for Laplace transforms. In the following Laplace transforms will be denoted by capital letters:

$$Z(s) = N(s) + Y(s). \quad (3.13)$$

By using the definition of the transfer function, one can rewrite  $Y(s)$  as:

$$Y(s) = T_{\text{laser}}(s) \cdot C(s) \quad (3.14)$$

$$= T_{\text{laser}}(s) \cdot T_{\text{FALC}}(s) \cdot E(s) \quad (3.15)$$

$$= T_{\text{laser}}(s) \cdot T_{\text{FALC}}(s) \cdot (R - G(s)) \quad (3.16)$$

$$= T_{\text{laser}}(s) \cdot T_{\text{FALC}}(s) \cdot (R - T_{\text{FRM}}(s) \cdot Z(s)). \quad (3.17)$$

The steady state is reached once the Unlimited Integrator compensates for DC offsets. In the steady state we set  $S = 0$ . By plugging Equation 3.17 into Equation 3.13 one finds:

$$Z(s) = N(s) + T_{\text{laser}}(s) \cdot T_{\text{FALC}}(s) \cdot T_{\text{FRM}}(s) \cdot Z(s) \quad (3.18)$$

$$\iff \frac{Z(s)}{N(s)} = \frac{1}{1 + T_{\text{laser}}(s) \cdot T_{\text{FALC}}(s) \cdot T_{\text{FRM}}(s)} = S(s) \quad (3.19)$$

where the latter  $S(s)$  is the closed Loop transfer function or *sensitivity function* [53]. However, this transfer function is only valid for noise that is introduced at the laser output. If one e.g. wants to consider

the impact of electronic noise introduced by the controller, the transfer function changes due to the different injection point.

To measure the response of the feedback loop to the intrinsic laser frequency noise, one has to measure the laser frequency deviations outside the feedback loop. In the next chapter, I will introduce a laser noise interferometer that is capable of characterizing the frequency noise of lasers over a broad range of wavelengths.

---

## Laser Noise Interferometer

---

As it was shown in [Chapter 3](#) a significant dephasing is experimentally observed. Aside the dephasing due to differential light shifts, thermal motion and inhomogeneous density the fit shown in [Figure 3.2](#) suggests, that frequency noise contributes to the overall dephasing of the superatom. To quantify this observation, one needs to know the noise characteristics of the two excitation lasers.

In this chapter the design of a Laser noise interferometer is presented that is able to measure the frequency noise spectral density of the probe and the control. The device needs to be capable of translating a frequency deviation into a measurable voltage deviation. A fiber-delayed Mach-Zehnder interferometer is used since it translates frequency deviations into a change the phase difference. This phase difference alters the intensity of the interference pattern, which is measured using an amplified photodiode. To assure a linear relation between phase difference and intensity a feedback loop optical path length in one interferometer arm. In this chapter the setup will be introduced in detail and the data post-processing is presented to extract the frequency noise spectral densities of the analyzed laser light.

In the scope of this thesis measuring frequency noise with a Fabry-Perot interferometer was investigated. At the of this chapter this alternative method is introduced and compared to the Mach-Zehnder interferometer.

### 4.1 Optical and Electronic Setup

[Figure 4.1](#) shows a picture and a sketch of the fiber-delayed unbalanced Mach-Zehnder interferometer used to analyze the laser light. In the following it will be distinguished between the *long arm*, which contains the optical fiber and the path length stabilization and the *short arm*, which has no delay.

The light is introduced into the setup via a polarization maintaining single mode fiber. For coupling light into fibers and collimating light after optical fibers lenses (A110TM-B from *Thorlabs*) with a focal length of 6.24 mm were used. Using lenses with the same focal length improves the fiber coupling and ensures a similar beam size for the long and the short arm.

Using a Zero-Order Half-Wave Plate (HWP) in combination with a polarizing beam splitter (PBS) the light is split into the long and the short arm with variable power. Thus, one can adjust the power splitting of both arms such that both beams have the same power at the second beam splitter, increasing the visibility of the interference pattern.

In the long arm the light is coupled into a 10-meter long polarization-maintaining single mode fiber, which is suitable for wavelengths between 770 nm and 1100 nm (P3-780PM-FC-10 from *Thorlabs*). A

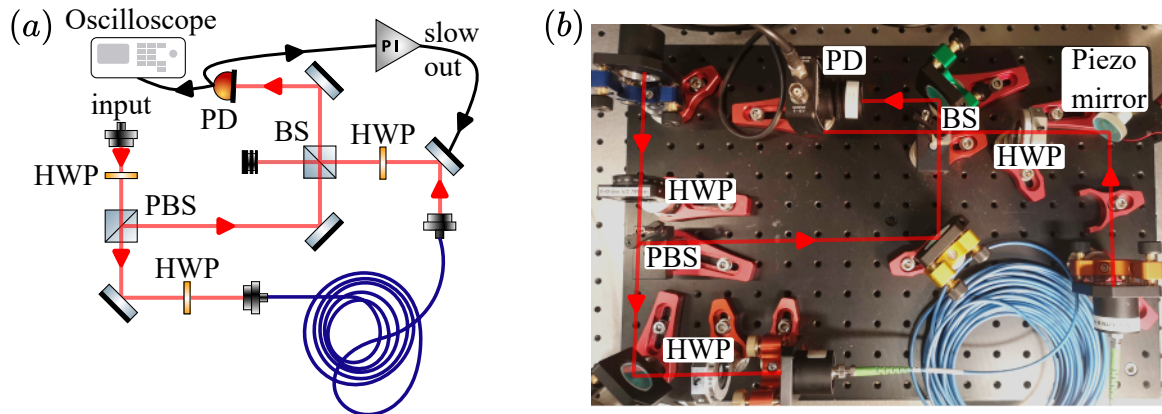


Figure 4.1: Sketch and photograph of the interferometer setup used to measure frequency noise. (a) Shows the sketch of the setup, with the light beam passing through (red). The light is fed in through a fiber (input) and split into the two arms using a Half-Wave-Plate (HWP) and a polarizing beam splitter (PBS). The light in the long arm is then coupled into an optical fiber (blue) and both arms are overlapped on a 50/50 beam splitter. One of the two transmission signals is recorded on an amplified photodiode (PD) and with a BNC-Y-piece the output is fed into an oscilloscope and the input of a PI-controller. The slow output of the PI controller is controls the piezo mirror in the long arm. (b) Shows the photograph of the setup, abbreviations are the same as in the sketch.

Half-Wave Plate in front of the fiber is used to adjust the polarization to one of the two fiber polarization axes. This reduces intensity fluctuations at the output of the fiber due the different propagation speeds of the fast and the slow polarization axis.

After the fiber the beam is reflected using the mirror mounted on the piezo electric crystal, that be controlled by applying a voltage. With the piezo electric crystal the relative phase between the light coming the long and the short arm can be regulated. The third Half-Wave Plate is used to match the polarizations of both interferometer arm to get maximum visibility in the interference signal. Both beams are overlapped on a 50/50-Beamsplitter (BS).

One of the overlapped beams is then measured on the amplified photodiode (PDA10A2 from *Thorlabs*), while the other beam is being blocked. The output of the photodiode is split using a BNC-Y-piece and connected to the input of the PID box and an oscilloscope recording the frequency noise. Each arm is terminated externally with a  $50\ \Omega$  resistor. This is important to match the impedance of the cable to reduce reflections of the electric signal.

For the stabilization the P- and the I-part of the PID-box are used stabilizing the optical path length difference between the two arms of the interferometer. [Figure 4.2](#) shows the relation between the intensity at the interferometer output as a function of the phase difference between the long and the short arm. By controlling the optical path length difference such that the phase difference is at the maximum slope (purple point) a linear relation between the phase difference and the intensity can be assumed. To accomplish this the *slow output* of the PID-controller is connected to the piezo electric crystal.

It is crucial that the lock is tuned to only compensate for slow drifts with frequencies below 1 kHz resulting from a change in temperature or vibrations. As the feedback loop compensates all fluctuations including frequency noise, the bandwidth of the feedback loop marks the lower boundary for measurable frequency noise fluctuations.

To ensure that the feedback loop only compensates for slow drifts a closed-loop network measurement is performed (see [Figure 4.3](#) (a)). The interferometer is stabilized using a laser and the PI-controller.

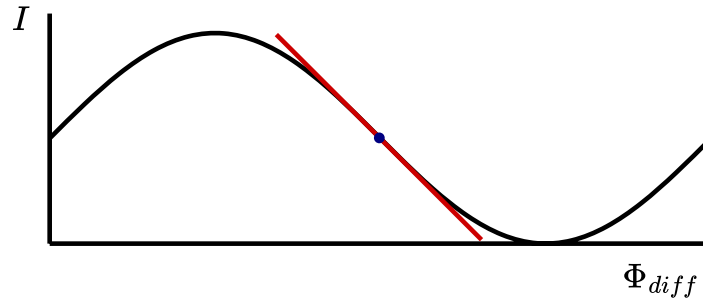


Figure 4.2: Sketch of Interferometer output intensity depending on the phase difference  $\Phi_{diff}$  between the interferometer arms (brown). By using the feedback loop the interferometer is stabilized such that the phase difference between the interferometer is at the maximum slope (purple point). Under this condition the transmission signal can be approximated by a linear curve (orange).

The *Source output* of the network analyzer and is connected to the second input of the PID controller, introducing a signal into the feedback loop. The monitor output of the PID-box is connected to the *Input* of the network analyzer.

Figure 4.3 (b) shows the observed Bode plots of the measurement. One can see that the feedback loop is compensating signals a frequency below 100 Hz reducing the amplitude and amplifies the signals with frequencies between 100 Hz and 1 kHz. Beyond 1 kHz the signal fed in by the spectrum analyzer and the measured signal have the same amplitude and are in phase. Therefore, there is no response by the system for frequencies larger than 1 kHz.

For recording the data an oscilloscope (WaveProHD by *Teledyne LeCroy*) with a ns-time-resolution was used. The oscilloscope can record traces with up to 100 million data points. This offers the possibility of resolving fluctuations in the low kHz and the high MHz regime. In contrast to a spectrum analyzer the use of an oscilloscope requires performing a Fourier transformation of the measured data to acquire a spectrum.

The possible wavelengths of the light that can be analyzed with this interferometer are limited by its components. The most crucial are the Half-Wave-Plates, with a narrow range of wavelengths. However, when changing the light source, these can be exchanged rather quickly. The other two limiting components are the optical fiber (770 nm to 1100 nm) and the polarizing beam splitter (600 nm to 1000 nm). Therefore, the setup can be used for laser light ranging from 770 nm to 1000 nm.

## 4.2 Theoretical Interferometer Output Signal

In the following a theoretical description of the measured interference signal is developed to analyze the recorded data successfully.

When two light beams with the electric field  $E_1(t) = E_1 \cdot \sin(2\pi\nu t + \Phi_1)$  and  $E_2(t) = E_2 \cdot \sin(2\pi\nu t + \Phi_2)$  with same frequency  $\nu$  are interfered on a beam splitter the intensity  $I$  of interference has the form

$$I = E_1^2 + E_2^2 + E_1 E_2 (\cos(\Phi_1 - \Phi_2 \pm \pi) - \cos(4\pi\nu t + \Phi_1 + \Phi_2 \mp \pi)) \quad (4.1)$$

Here the phase shift by  $\pi$  results from the fact that one of the two beams has been reflected and one

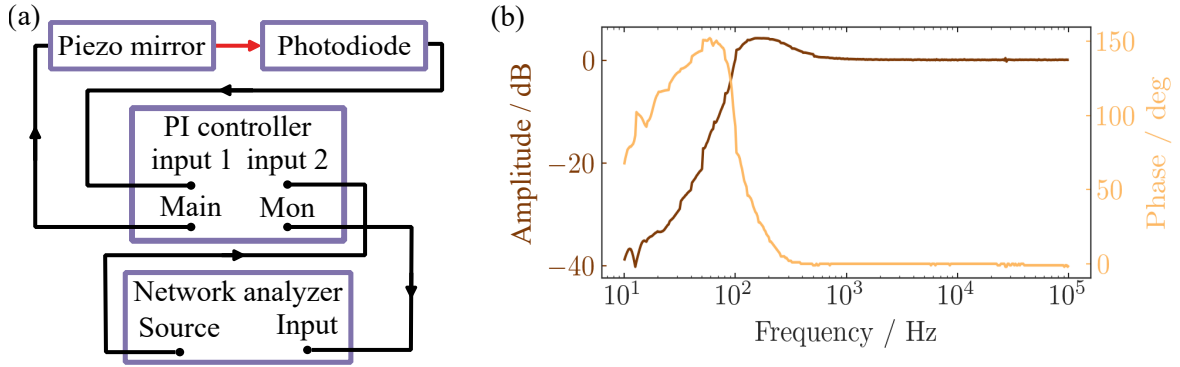


Figure 4.3: Measurement of the interferometers PI controller. (a) Measurement setup to analyze the response of the closed feedback loop. The network analyzer feeds a sinusoidal signal into the *Input 2* of the controller and measures the response at the *Monitor output* of the controller. The controller drives the piezo electric crystal with the mirror. This affects the measured signal on the photodiode (red arrow) which is fed into *Input 1*. (b) Measured Bode plot of the PI-controllers response in the closed loop measurement. The amplitude (brown) and the phase (yellow) response of the closed feedback loop was measured for a signals fed in between 10 Hz to 100 kHz. The amplitude response at below 100 Hz is negative since the feedback loop is compensating for the signal from the spectrum analyzer. The phase signal was shifted by 180° since the network analyzer cannot distinguish between absolute phase shifts, which are multiples of 180°. In this way the in- and output signal match if the feedback loop does not respond.

was transmitted by the beam splitter. This depends on which of the two interference signals is being measured.

In the case of a Mach-Zehnder Interferometer the input beam is broken down into two beams  $E_1(t)$  and  $E_2(t)$  with the first polarizing beam splitter and overlapped on the beam splitter again. If one then measures the transmitted power after the second beam splitter intensity has the form:

$$I = E_1^2 + E_2^2 + E_1 E_2 (\cos(\Phi_1 - \Phi_2) - \cos(4\pi\nu t + \Phi_1 + \Phi_2)), \quad (4.2)$$

where  $\Phi_1$  and  $\Phi_2$  describes the phase the light acquired passing through the arms of the interferometer. In the following we will denote the difference between  $\Phi_1$  and  $\Phi_2$  as  $\Phi_{\text{diff}} = \Phi_1 - \Phi_2$ .

Since  $\nu$  is in the THz regime the second term in Equation 4.2 is discarded since it cannot be resolved with a photodiode. The measured intensity then simplifies to

$$I = E_1^2 + E_2^2 + E_1 E_2 \cos(\Phi_{\text{diff}}). \quad (4.3)$$

In the following it is assumed that a change in the phase difference  $\Phi_{\text{diff}}$  originates from a change of the light frequency  $\nu(t)$  over time. For that the frequency is split into the constant carrier frequency  $\nu_0$  and the fluctuations  $\Delta\nu(t)$

$$\nu(t) = \nu_0 + \Delta\nu(t), \quad (4.4)$$

where  $\Delta\nu(t)$  denotes the noise that we want to measure (see Figure 4.4 (a)).

If one assumes that one of the beams is delayed by the time  $\tau \approx 49 \mu\text{s}$ , due to passing through the

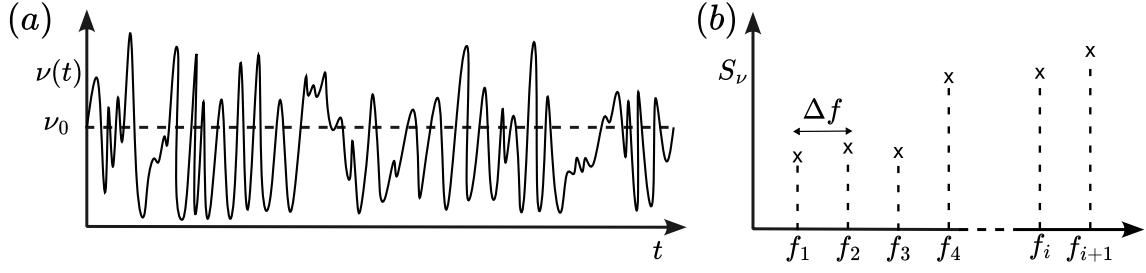


Figure 4.4: Illustration of the transformation of a frequency trace into a power spectrum. (a) A sketch of the fluctuation of a laser frequency  $\nu(t)$  in time around the carrier frequency  $\nu_0$ . (b) Sketch of a discrete frequency noise power spectral density  $S_\nu$  where  $f_i$  denotes the frequency of each noise component with a bin width of  $\Delta f$ .

optical fiber, this means that phase difference at time  $t$  corresponds to

$$\Phi_{\text{diff}}(t) = 2\pi \int_{t-\tau}^t \nu(t') dt' + \Phi_0 = 2\pi \int_{t-\tau}^t \Delta\nu(t') dt' + \underbrace{\Phi_0 + 2\pi\nu_0\tau}_{\Phi'_0}. \quad (4.5)$$

Here  $\Phi_0$  denotes the phase difference resulting from the difference in optical path length in both arms. All time-constant contributions can be summarized by  $\Phi'_0$  since the setup is only capable of measuring changes in the phase difference due to the feedback loop.

The fluctuation of the frequency  $\Delta\nu(t)$  approximated as a sum of oscillations with the discrete frequencies  $f_i$  and a random phase  $\Phi_{f,i}$  [44]

$$\Delta\nu(t) = \sum_i \sqrt{2S_{\nu,i}\Delta f} \cos(2\pi f_i t + \Phi_{f,i}), \quad (4.6)$$

where  $\Delta f = f_{i+1} - f_i$  denotes the difference of two frequencies and  $S_{\nu,i}$  is the spectral power of each noise component with frequency  $f_i$  (see Figure 4.4).

Plugging Equation 4.6 into Equation 4.5 leads to

$$\Phi_{\text{diff}}(t) = \sum_i \sqrt{2S_{\nu,i}\Delta f} 2\pi \int_{t-\tau}^t \cos(2\pi f_i t + \Phi_{f,i}) dt' \quad (4.7)$$

$$= \sum_i \sqrt{2S_{\nu,i}\Delta f} 2\pi \left[ \frac{1}{2\pi f_i} \sin(2\pi f_i t + \Phi_{f,i}) \right]_{t-\tau}^t + \Phi'_0 \quad (4.8)$$

$$= \sum_i \sqrt{2S_{\nu,i}\Delta f} \frac{2}{f_i} \sin(\pi f_i \tau) \cos\left(2\pi f_i t - \underbrace{\pi f_i \tau + \Phi_{f,i}}_{\Phi'_{f,i}}\right) + \Phi'_0 \quad (4.9)$$

$$= \sum_i \sqrt{2S_{\nu,i}\Delta f} \frac{2 \sin(\pi f_i \tau)}{f_i} \cos(2\pi f_i t + \Phi'_{f,i}) + \Phi'_0 \quad (4.10)$$

where one can sum up the constant phases in the cos since these are experimentally not measurable. This solution can be broken down into four parts:

- $\sqrt{2S_{v,i}\Delta f}$  contains the amplitudes of each frequency noise component, are measured.
- $\frac{2\sin(\pi f_i \tau)}{f_i}$  is a suppression term that describes destructive interference of noise components, between the long and the short interferometer arm.
- $\cos(2\pi f_i t + \Phi'_{f,i})$  is the time-dependent term, that contains the oscillation of each noise component.
- $\Phi'_0$  is a constant phase added arising from the intrinsic phase difference of the light passing through both interferometer arms. This value is affected by environmental changes, e.g. temperature drifts. Especially the optical fiber is prone to expanding when the ambient temperature changes affecting the optical path length of the long arm. Such drifts are compensated by the feedback loop and thus  $\Phi'_0$  is constant in time.

As indicated in [Figure 4.2](#) at the locking point is chosen such that the measured intensity  $I$  is proportional to the phase difference  $\Phi_{\text{diff}}$ . Therefore, one expects the measured intensity to have the form:

$$I(t) = \sum_i \sqrt{2S_{v,i}\Delta f} \frac{2\sin(\pi f_i \tau)}{f_i} \cos(2\pi f_i t + \Phi'_{f,i}) + I_{\text{offset}}, \quad (4.11)$$

where  $I_{\text{offset}}$  denotes the measured intensity at the locking point, if there was no frequency noise.

### 4.3 Experimental Determination of Laser Frequency Noise Spectra

To perform a measurement the interferometer has to be set up for the wavelength to be analyzed. To do that suitable half-wave-plates have to be put in, the light has to be coupled into the optical fiber, the pointing and polarization of the light coming from the long and the short arm has to match.

The measurement of the frequency noise power spectral density consists of three steps: A calibration measurement, the noise spectrum measurement and a background measurement.

For the calibration the feedback loop is turned off and a function generator is connected to the piezo electric crystal with the mirror. The function generator feeds a saw-tooth signal into the piezo electric crystal, which corresponds to linearly scanning the phase difference  $\Phi_{\text{diff}}$  up and down. An oscilloscope trace of the measured intensity can be seen in the left plot of [Figure 4.5](#). The sharp edges visible correspond to the saw-tooth changing from a positive to a negative slope. Slight asymmetries of the curve around this turning points result from the hysteresis of the piezo electric crystal [66]. To these traces, sinusoidal function can be fitted, to extract the slope at the locking point (see yellow curves in [Figure 4.5](#)).

For the noise measurement the slow-output of the PID-controller is connected to the piezo mirror and interferometer is locked using the P- and the I-Part such that the optical path length difference is kept constant. However, the response is limited by the maximum output voltage of PID-controller. To increase stability the setup is placed on a temperature-stabilized and covered laser table with closed covers. The setup is especially sensitive to drifts in the temperature changes as they cause the optical fiber to expand leading to a change in the optical path length difference. Once the setup has thermalized one can record the output signal of the photodiode with the oscilloscope. In the oscilloscope the distance between two data points is set to 10 ns and traces of  $10^8$  data points are taken (see light purple curve in [Figure 4.5](#)). By collecting multiple data traces one can reduce the statistical error in the measured spectrum.

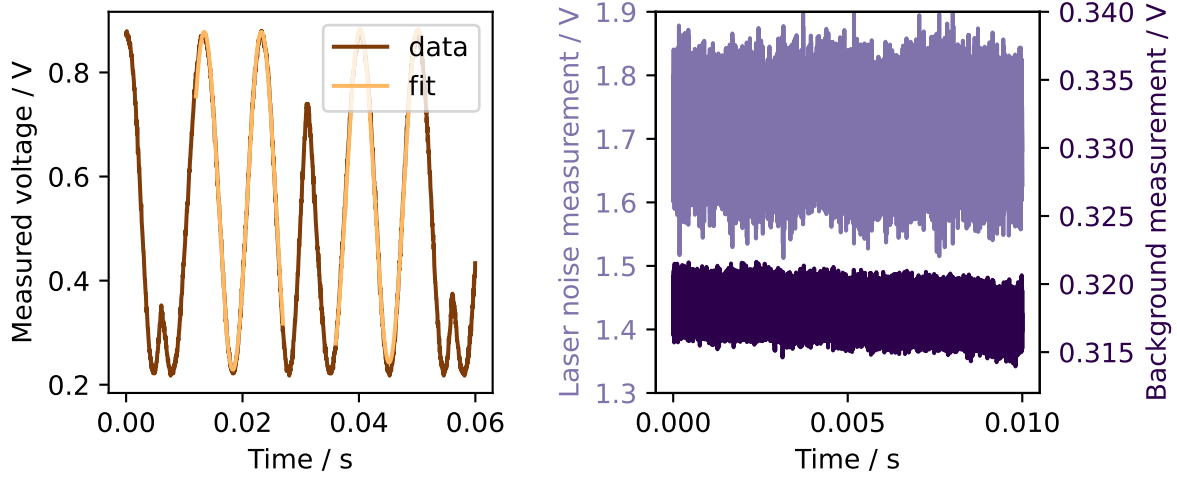


Figure 4.5: Calibration measurement and recorded noise traces. (Left) Example of a calibration measurement where the optical path difference is scanned by feeding a saw-tooth signal into the piezo mirror. The sharp edge in the center corresponds to an edge in the saw-tooth signal. A cosine function can be fitted to the steady part of the trace (yellow) to obtain the maximum slope. (Right) Traces of a noise (light purple) and a background (dark purple) measurement of the probe laser. The noise measurement is performed with the interferometer locked, and the background measurement is conducted with the short arm blocked. The y-axis shows measured output voltage of the amplified photodiode.

For the background measurement the short interferometer arm is blocked and traces of photodiode signal are recorded with the oscilloscope (see dark purple trace in Figure 4.5). With the background measurement one wants to measure fluctuations in the interference signal that do not originate from the frequency noise: These are on one hand fluctuations in the power and polarization in the laser light. The latter affects the splitting of the two interferometer arms, which affects the measured intensity. Also, this measurement accounts for fluctuations in the light transmitted through the fiber due to temperature, pressure drifts or mechanical vibrations, which also affects the measured intensity.

To obtain a frequency noise spectrum, as previously described, three different traces have been recorded: A *calibration trace* showing the cosine dependence of the measured voltage on the phase difference. The *noise trace* with the interferometer running and locked, measuring the frequency noise of the laser light. A *background trace* with one interferometer arm blocked measuring intensity fluctuations that do not result from frequency noise of the laser light. Changes in the phase difference  $\Phi_{\text{diff}}$  are calibrated to changes in the measured voltages  $U$  using the slope

$$\alpha = \frac{dU}{d\Phi_{\text{diff}}} \quad (4.12)$$

from the calibration measurement. The piezo electric crystal was operated in its linear regime, with the expansion being proportional to the voltage applied. Since the saw-tooth-signal applied to the piezo crystal with the function generator is linear in time  $t$  it can be approximated that  $t \propto \Phi_{\text{diff}}$ . This allows to fit a function of the form

$$f(t) = A \cdot \sin(t \cdot B + C) + D \quad (4.13)$$

to the continuously differentiable part of the calibration scan, where  $A, B, C, D$  are fitting parameters (see yellow curves in [Figure 4.5](#)). The proportionality between the time  $t$  and the phase difference  $\Phi_{\text{diff}}$  allows replacing  $t \cdot B = \Phi_{\text{diff}}$  in [Equation 4.13](#). This leads to

$$\alpha = \left. \frac{dU}{d\Phi_{\text{diff}}} \right|_{\Phi_{\text{diff,lock}}} = \left. \frac{df(\Phi_{\text{diff}})}{d\Phi_{\text{diff}}} \right|_{\Phi_{\text{diff,lock}}} = A \cdot \cos(\Phi_{\text{diff,lock}} + D) \quad (4.14)$$

where  $\Phi_{\text{diff,lock}}$  is the phase difference at which the interferometer is locked. The value of  $\Phi_{\text{diff,lock}}$  is calculated from the averaged noise trace  $\bar{U}_{\text{data}}$  by using the inverse fit function:

$$\Phi_{\text{diff,lock}} = f^{-1}(\bar{U}_{\text{data}}) \quad (4.15)$$

With the value for  $\alpha$  calculated from the calibration measurements, the recorded noise traces can be translated into noise spectral densities (see [Figure 4.4](#)). To turn the traces into spectra Welch's method instead of a Fourier transform is used, because it produces a lower uncertainty in the calculated spectrum. In Welch's method the noise trace is separated into overlapping segments of  $M = 2 \cdot 10^6$  data points, modified by a window function and then being Fourier transformed [67]. By averaging over the spectra acquired from each window the uncertainty of the obtained spectrum is reduced significantly. Here, a Hanning window was chosen to modify the data in each segment as [68]

$$w_{\text{H}}(n) = 0.5 \left( 1 - \cos\left(2\pi \frac{n}{M}\right) \right) \quad (4.16)$$

where  $n$  denotes the  $n$ -th data point in the segment of the length  $M$ . Due to the shorter length of the segments compared to the entire trace, low frequencies cannot be resolved. Each segment is  $\tau = 2 \cdot 10^6 \cdot 10 \text{ ns} = 10 \text{ ms}$  long, meaning that frequencies below 100 Hz cannot be measured. However, these frequency noise components are anyway suppressed by the feedback loop of the interferometer.

After applying Welch's method to the noise and the background trace one gets two voltage power spectra  $S_{U,\text{data}}$  and  $S_{U,\text{background}}$  in units of  $\text{V}^2/\text{Hz}$ . A voltage spectrum  $S_U$  is related to the measured voltage trace  $U(t)$  by

$$U(t) = \sum_i \sqrt{2S_U \Delta f} \cos(2\pi f_i t + \Phi_{f;i}) + U_{\text{offset}} \quad (4.17)$$

where  $S_U$  is the corresponding spectrum and  $\Delta f$  is the distance of two frequency components  $f_i$  and  $f_{i+1}$  and the constant offset  $U_{\text{offset}}$ .

Using that the interferometer was locked at the maximum slope (see [Figure 4.2](#)) one can assume a linear relation between the phase difference  $\Phi_{\text{diff}}(t)$  and the measured the output voltage  $U(t)$ . Let  $\Delta\Phi_{\text{diff}} = \Phi_{\text{diff}}(t) - \Phi'_0$  describe a change in the phase difference  $\Phi_{\text{diff}}(t)$  and  $\Delta U(t) = U(t) - U_{\text{offset}}$  denote a change in the measured voltage  $U(t)$ . Using [Equation 4.12](#) the relation between one can derive

$$\Delta U(t) = \alpha \cdot \Delta\Phi_{\text{diff}}(t). \quad (4.18)$$

After plugging in [Equation 4.17](#) for  $U(t)$  and [Equation 4.10](#) for  $\Phi_{\text{diff}}(t)$  one obtains

$$\sum_i \sqrt{2S_U \Delta f} \cos(2\pi f_i t + \Phi_{f;i}) = \alpha \cdot \sum_i \sqrt{2S_{v;i} \Delta f} \frac{2 \sin(\pi f_i \tau)}{f_i} \cos(2\pi f_i t + \Phi'_{f;i}). \quad (4.19)$$

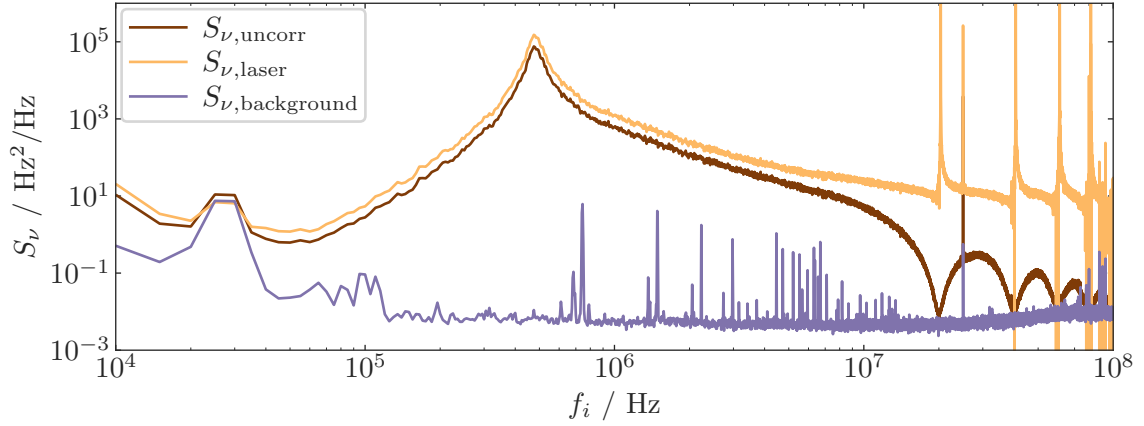


Figure 4.6: Measured frequency noise spectral densities of the control laser.  $S_{\nu,\text{laser}}$  is the frequency noise spectral density with the background subtracted.  $S_{\nu,\text{background}}$  (purple) is the measured background due to fluctuations in the laser power or polarization of the light.  $S_{\nu,\text{uncorr}}$  (brown) is the uncorrected frequency noise spectral density showing the characteristic suppression dips of the interferometer.

This can be separated by each oscillation term  $\cos(2\pi f_i t + \Phi_{f:i})$  to connect the entries of the voltage noise spectrum  $S_{U;i}$  and frequency noise spectrum  $S_{\nu;i}$  as

$$S_{U;i} = S_{\nu;i} \cdot \left( \alpha \cdot \frac{2 \sin(\pi f_i \tau)}{f_i} \right)^2 \iff S_{\nu;i} = S_{U;i} \cdot \left( \frac{f_i}{\alpha \cdot 2 \sin(\pi f_i \tau)} \right)^2. \quad (4.20)$$

Using Equation 4.20, the voltage noise power spectral densities  $S_{U,\text{data}}$  and  $S_{U,\text{background}}$  can be translated into frequency noise power spectral densities  $S_{\nu,\text{data}}$  and  $S_{\nu,\text{background}}$  in  $\text{Hz}^2/\text{Hz}$ . The final frequency noise power spectral density  $S_{\nu}$  of the laser light is given by

$$S_{\nu,\text{laser}} = S_{\nu,\text{data}} - S_{\nu,\text{background}} \quad (4.21)$$

Figure 4.6 shows an example of the obtained frequency noise power spectral densities  $S_{\nu,\text{laser}}$  and  $S_{\nu,\text{background}}$  measured for the control laser. To illustrate the suppression effect (see second term in Equation 4.10), the uncorrected spectrum  $S_{\nu,\text{uncorr}}$  of the form

$$S_{\nu,\text{uncorr}} = S_{U,\text{data}} \cdot \left( \frac{1}{2\pi\tau\alpha} \right)^2 \quad (4.22)$$

is plotted as well. The suppression dips are visible in  $S_{\nu,\text{uncorr}}$  at multiples of  $f_{\text{sup}} = 1/\tau \approx 20$  MHz. The correction from Equation 4.20 does not work perfectly as  $S_{\nu,\text{laser}}$  has significant fluctuations around  $f_{\text{sup}}$ . This result from an inaccuracy in the calculated value for  $\tau$  and  $S_{\nu,\text{uncorr}}$  not going to 0 but settling at the level  $S_{\nu,\text{background}}$ . However, below  $f_{\text{sup}}$  a smooth spectrum is obtained that can be used for further analysis.

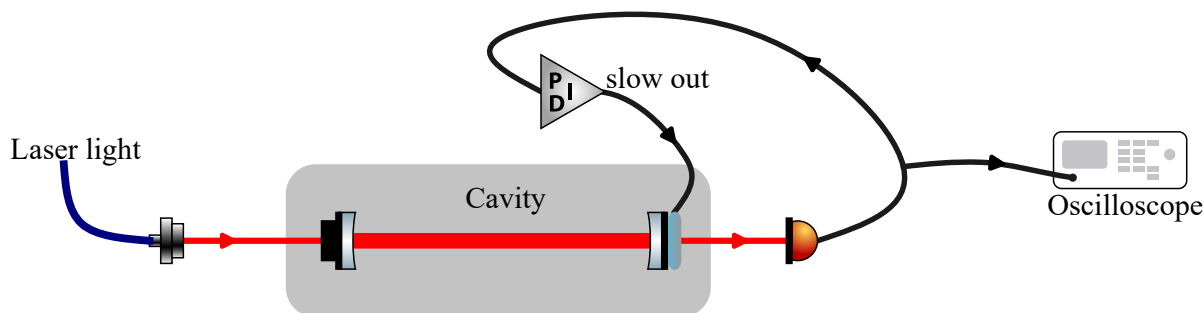


Figure 4.7: Setup for measuring laser frequency noise with a Fabry-Perot interferometer. The laser light is outcoupled from an optical fiber (dark blue) and then coupled into the Fabry-Perot interferometer (cavity). The transmission signal is used to stabilize the cavity with a PID controller and to perform the actual measurement with an oscilloscope.

#### 4.4 Alternative: Using a Fabry-Perot Interferometer instead of a Mach-Zehnder interferometer

Alternatively to the Mach-Zehnder interferometer one can also use a Fabry-Perot interferometer to measure the frequency noise of a laser. The frequency dependent transmission of a cavity can be used to detect frequency fluctuations as fluctuations in the transmitted power. The idea is to lock the cavity to the side of one of the characteristic transmission fringes and approximate the fringe with a linear slope (see left plot in Figure 4.8).

The setup is more simple, since the light of the laser is directly coupled into the cavity and the transmission is recorded on a photodiode (see Figure 4.7). The cavity length is stabilized to a fixed length with a feedback loop measuring the transmitted intensity. One of the cavity mirrors is mounted on a piezo electric crystal, that is controlled by applying a voltage tuning the length of the cavity. The transmitted intensity is measured with an amplified photodiode and the signal is fed into a PID-controller. The slow output of the controller drives the piezo electric crystal holding the mirror inside the cavity.

Simultaneously, the signal from the photodiode is recorded on a spectrum analyzer to measure the noise spectrum of the laser.

To do a calibration measurement one has to connect a function generator to the piezo mirror and feed in a saw-tooth signal. The transmission signal is recorded on an oscilloscope. The left plot in Figure 4.8 shows the transmission fringes of the Fabry-Perot interferometer. The x-axis is then recalibrated by using the Free Spectral Range of the cavity [69]

$$\Delta\nu_{\text{FSR}} = \frac{c}{2nL}, \quad (4.23)$$

where  $c$  is the speed of light,  $n$  is the refractive index inside the cavity and  $L$  is the distance between the two mirrors. As there are even and odd modes present the distance between two interference fringes corresponds to  $\Delta\nu_{\text{FSR}}/2$ .

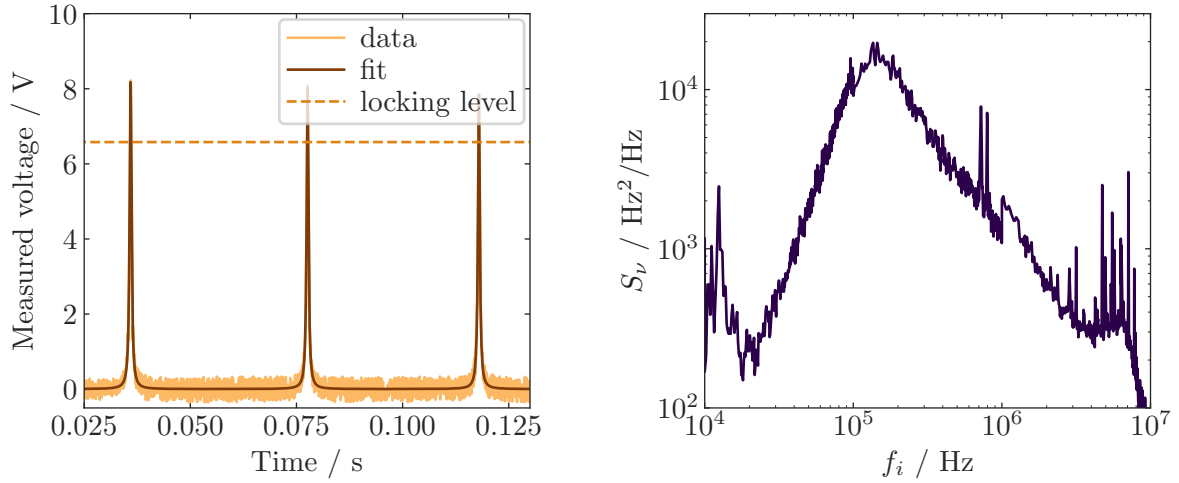


Figure 4.8: Example of a frequency noise measurement using the Fabry-Perot interferometer. (Left) Calibration measurement trace (yellow), where the voltage is applied to the piezo mirror is scanned linearly using a saw-tooth signal. The trace shows the characteristic transmission fringes of a Fabry-Perot interferometer. A function consisting of three Lorentzian peaks (brown) was fitted to the interferometer signal. The dashed line (orange) marks the maximum slope of the interference fringes. This corresponds to the locking point of the feedback loop. (Right) Measured noise spectrum of the locked probe laser. The spectrum was measured for different settings of the FALC than described in [section 3.3](#).

After recalibration, the transmission signal is fitted with Lorentzian peaks of the form

$$f(\nu) = \frac{A}{1 + \left(\frac{\nu-B}{0.5C}\right)^2} \quad (4.24)$$

where  $\nu$  is the laser frequency and  $A, B, C$  are fitting parameters determining the height, position and width of the peak.

The feedback loop is tuned such that the locking point is at the steepest part of the interference fringe (see dashed line in left plot of [Figure 4.8](#)). At the locking point the relation between the frequency and the transmitted intensity is approximately linear with a slope of

$$\tilde{\alpha} = \frac{dU}{d\nu}. \quad (4.25)$$

With the calibration in place, one can then measure the frequency noise of the laser light. For that the feedback loop is activated, and the transmitted intensity is recorded. Similarly to the Mach-Zehnder interferometer, one obtains the voltage power spectrum  $S_{U;i}$  as described in [Equation 4.17](#). To transform this into the frequency noise power  $S_\nu$ , spectrum one uses

$$S_{\nu;i} = \frac{1}{\tilde{\alpha}^2} S_{U;i} \quad (4.26)$$

To distinguish noise in the laser power from frequency noise one shines the laser light on the directly on the photodiode to perform a background measurement. The recorded background spectrum is subtracted

from the measured noise spectrum of the laser.

The right plot in [Figure 4.8](#) shows a measured frequency noise spectral density of the probe laser after the background correction. The spectrum is more noisy than the measurement shown in [Figure 4.6](#), which results from averaging over less data points. The drop in the spectrum at 10 MHz is an effect of cable reflections, the impedance was not properly matched.

The choice of the cavity is crucial for the precision of this method: The finesse  $\mathcal{F}$  determines how narrow the peaks in the transmission signal are. A higher Finesse increases the slope and therefore the sensitivity of the setup, but also reduces the frequency range where the linear approximation is valid. In the measurement shown in [Figure 4.8](#), the cavity had a Finesse of  $\mathcal{F} \approx 60$  and a Free Spectral Range of  $\Delta\nu_{\text{FSR}} = 1.5$  GHz. Thus, the full width at half maximum of an interference fringe is given by  $\nu_{\text{FWHM}} = \frac{\Delta\nu_{\text{FSR}}}{\mathcal{F}} \approx 25$  MHz [69].

Compared to the Mach-Zehnder interferometer, the Fabry-Perot interferometer is only usable for a narrow range of wavelengths, which is limited by the high-reflectivity coatings. The interferometer used in the measurement shown in [Figure 4.8](#) was only suitable to be used for 780 nm and therefore the frequency noise of the control laser with the seed laser wavelength of 960 nm could not be measured with this method. Also, one needs to tune the frequency of the laser to be close in frequency to one of the cavity transmission peaks, which is not possible for every laser and depends on the given setup. Overall the Mach-Zehnder interferometer turned out to be the superior device to measure the frequency noise of the probe and the control laser.

---

## Influence of Frequency Noise the Two-Photon Rydberg Excitation

---

As shown in [Chapter 2](#), laser noise influences the coherent interaction between few photons and a Rydberg superatom.

In this chapter, I present how the frequency noise of the two excitation lasers impacts the dephasing of superatom Rabi oscillations. In a first step the frequency noise power spectral densities of the probe and control laser are analyzed. To give an estimate of the expected dephasing rate  $\gamma_\nu$  (see [Equation 2.39](#)) a simulation of the superatom driven by a noisy light field is performed. Finally, Rabi oscillation measurements for different noise spectra and Rabi frequencies are compared with the simulation results to understand the characteristics of this dephasing mechanism.

### 5.1 Measured Frequency Noise Spectra of the Probe and Control laser

The frequency noise power spectral densities of the probe and control laser are measured using the scheme described in [Chapter 4](#). For each of the lasers the three different noise spectra were recorded: First the free-running laser with no feedback loop for frequency stabilization (Unlocked). This is the intrinsic frequency noise of the laser. Secondly, the spectrum of the laser light is measured with the frequency stabilization activated and the *optimal* settings of the FALC (see [Table 3.1](#)). With these settings the maximum bandwidth of the feedback loop is achieved, leading to a suppression over the largest range of noise frequencies possible. Third, the spectrum of the laser was measured for *worsened* settings of the FALC (see [Table A.1](#)) reducing the bandwidth of the feedback loop.

All spectra shown in this chapter are limited to noise frequencies between 5 kHz and 10 MHz since this is the optimal working range for the interferometer. The lower boundary is given by the stabilization of the interferometers internal stabilization and the upper boundary is the suppression effect, which cannot be perfectly compensated for (see [Figure 4.6](#)).

#### 5.1.1 Probe Laser

[Figure 5.1](#) shows the observed frequency noise power spectral densities observed of the Probe laser for the free-running, optimally locked and worsened locked cases. In the following the characteristics of these spectra will be analyzed using the probe laser as an example.

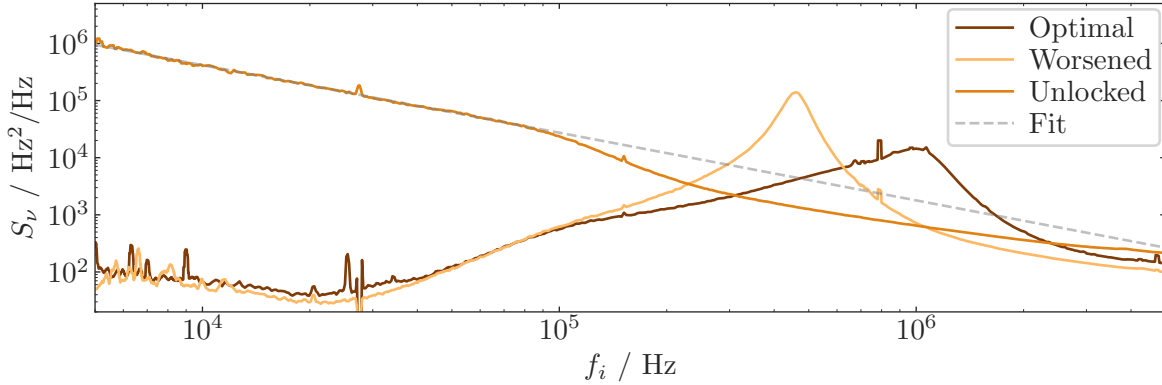


Figure 5.1: Measured frequency noise power spectral density for different feedback loop configurations of the probe laser. When the laser is free-running or unlocked (orange) one measures the intrinsic frequency noise of the laser. The optimal case (brown) shows the laser frequency noise for closed feedback loop with the setting from Table 3.1, which is the setting that is normally used in the experiment. The third curve (yellow) shows the frequency noise power spectral density, for the FALC configuration from Table A.1 where the bandwidth of the feedback loop was intentionally reduced. The gray dashed line shows function Equation 5.1 fitted to the free-running spectrum.

In the free-running case one observes the pure intrinsic frequency noise of the laser diode. To quantify whether that has the predicted  $1/f$ -shape (see section 3.3) a function of the form

$$y(f) = \frac{a}{x^b} \quad (5.1)$$

is defined, where  $a$  and  $b$  denote fitting parameters. Equation 5.1 is fitted to the free-running spectrum between 5 kHz and 100 kHz (see gray dashed line in Figure 5.1), to avoid fitting the dent at 100 kHz. The fit leads to  $a = 2.28(7) \times 10^{10} \text{ Hz}^2/\text{Hz}$  and  $b = 1.184(4)$ . Therefore, in the fitting range the free-running spectrum approximately resembles the expected  $1/f$ -shape. The dent at 100 kHz indicates that the  $1/f$ -noise has a limited bandwidth.

Comparing the two spectra of the frequency locked laser to the spectrum of the free-running laser one the suppression effect of the feedback loop becomes visible: The lock reduces the frequency noise below 200 kHz by several orders of magnitude. However, this also gives rise to the servo bump: The feedback loop amplifies the intrinsic laser noise leading to the spectrum exceeding the intrinsic noise. An amplification happens, if the feedback loop response has a phase delay of  $90^\circ$  or more and a gain that is larger than 1. At a phase delay of  $180^\circ$  feedback loops response is in phase with the noise and the amplification is maximal and for a gain  $> 1$  the system begins to oscillate and becomes unstable [70]. For the optimal FALC setting the servo bump maximum is at  $\sim 1.1$  MHz, while for the worsened settings is at  $\sim 450$  kHz.

As the feedback loop and its components is too slow to compensate for fast fluctuations the phase lag increases rapidly at high frequencies (e.g. see Figure 3.4). In order to prevent the feedback loop from amplifying the high-frequency noise components leading to resonant behavior of the system the gain is chosen to be small at high frequencies. Therefore, the feedback loop neither amplifies nor compensates in the high-frequency regime (roll-off) [53, 65]. Thus, one observes that the spectra of the both locked and the free running measurement converge at around 10 MHz.

To change the noise spectrum of the laser in the locked case from the optimal setting to the worsened

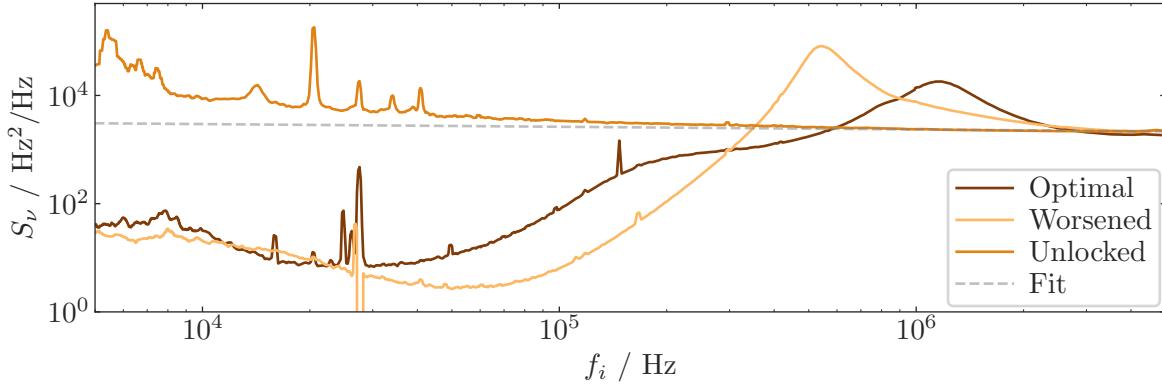


Figure 5.2: Measured frequency noise power spectral densities of the control laser. When the laser is free-running (unlocked) one measures the intrinsic frequency noise. The optimal case (brown) shows the laser frequency noise for closed feedback loop with the setting from Table 3.1, which is the setting that is normally used in the experiment. The third curve (yellow) shows the frequency noise power spectral density of the probe laser, when the location of the servo bump was intentionally shifted towards lower frequencies (settings from Table A.1). The gray dashed line shows function Equation 5.1 fitted to the free-running spectrum.

setting the Fast Limited Integrator (FLI) and the Main Gain was changed. The setting of the FLI was changed from setting “1” to “3”. Thereby the FLI is now turned on with the corner frequencies  $f_1 = 300$  kHz and  $f_2 = 3.5$  MHz. This causes an additional phase lag, compared to the optimal case, between  $f_1 = 300$  kHz and  $f_2 = 3.5$  MHz. Therefore, the phase delay of  $90^\circ$  of the total feedback loop is reached at lower frequencies. Lifting the overall gain profile by increasing the Main gain from “0.6” to “0.7”. This means that a Closed-loop gain of  $> 1$  is met at lower frequencies. This reduces the location of the servo bump further. The corner frequency settings and calculated Bode plots of the worsened FALC settings can be found in the appendix at section A.2.

### 5.1.2 Control Laser

The control laser light has a wavelength of 480 nm cannot be used with the optical fiber and polarization optics built into the interferometer setup. To circumvent this problem the laser light coming from the tapered amplifier before being frequency-doubled in the internal second-harmonic-generation cavity was measured. Thereby, Figure 5.2 shows the measured frequency noise spectrum of the control lasers 960 nm. The spectrum of the 480 nm light is expected to be proportional to the presented spectrum, but amplified by factor 4 due to the frequency doubling.

In the free-running case one can, as for the probe, observe the intrinsic frequency noise of the laser. To characterize that, a function of the form Equation 5.1 is fitted to the data (see Figure 5.2) leading to  $a = 4.7(2)$  Hz<sup>2</sup>/Hz (height) and  $b = 5.0(3) \times 10^{-2}$ . Thus, the frequency noise of the control laser has a significantly lower slope than the expected  $1/f$ . This might be a characteristic of the laser diode built into the control laser. Also, several peaks appear in the frequency regime between 5 kHz and 50 kHz, which could be due to outer perturbations or imperfect current driving electronics.

To move the servo bump from the optimal setting of  $\sim 1.1$  MHz the Fast Limited Integrator (FLI), the Fast Limited Differentiator (FLD) and the Main Gain were used. The corner frequencies of the FLI were shifted from  $f_1 = 6.5$  kHz and  $f_2 = 80$  MHzs to  $f_1 = 65$  kHz and  $f_2 = 800$  MHz shifting the phase lag induced by the FLI towards higher frequencies. The corner frequencies of the FLD were shifted from

$f_1 = 1$  MHz and  $f_2 = 190$  kHz to  $f_1 = 2.3$  MHz and  $f_2 = 420$  kHz. In this way the phase lead of the FLD is shifted towards higher frequencies. Overall this means, that the phase lag of the controls Fast Analog Linewidth Control (see [Figure 3.4](#)) is increased and shifted to higher frequencies. By turning the main gain from  $\sim 0.3$  to  $\sim 0.2$  the overall gain profile of the feedback loop is lowered, which shifts the servo bump to  $\sim 500$  kHz. The corner frequency settings and calculated Bode plots of the worsened settings of the FALC are in the appendix at [section A.2](#).

## 5.2 Bode's Integral Formula

In [Equation 3.19](#) the sensitivity function was introduced, which describes the suppression of noise introduced at the lasers output in the closed loop. Bode's Integral formula puts a fundamental mathematical restriction on the sensitivity function  $S$  [[53](#)]

$$\int_0^{\infty} \log |S(i\omega)| d\omega = \pi \sum p_k \quad (5.2)$$

where  $\omega$  denotes the frequency and  $p_k$  denote the poles in the right half-plane of the open loop transfer function  $L(s) = T_{\text{laser}}(s) \cdot T_{\text{FALC}}(s) \cdot T_{\text{FRM}}(s)$ . This relation is only valid if the open Loop transfer function  $L(s)$  goes to 0 with at least  $1/s^2$  in the Laplace plain. Since all components in the feedback loop have a limited bandwidth, and we know that the amplification in the transfer function of the FALC and the laser go to 0 for large frequencies we can assume that this is fulfilled. Using the definition of the sensitivity function from [Equation 3.19](#) one can deduce:

$$S(i\omega) = \frac{Z(i\omega)}{N(i\omega)} = \frac{\int_0^{\infty} e^{-i\omega t} z(t) dt}{\int_0^{\infty} e^{-i\omega t} n(t) dt} \quad (5.3)$$

where  $n(t)$  and  $z(t)$  are traces of the noise and the output signal in time. Thus,  $N(i\omega)$  and  $Z(i\omega)$  correspond to Fourier transforms of those which is similar to the measured noise spectra  $S_{v,\text{unlocked}}$  and  $S_{v,\text{locked}}$ . This is however only accurate if the frequency fluctuations are the only sources of noise in the feedback loop (ignoring e.g. electronic noise in the controller). Inserting the recorded spectra into [Equation 5.2](#) leads to

$$\int_0^{\infty} \log \left| \frac{S_{v,\text{locked}}}{S_{v,\text{unlocked}}} \right| = 0 \quad (5.4)$$

if there is no pole in the open loop transfer function  $L(s)$ . Poles in the right half plane correspond to an unstable system, but since the frequency lock is stable over long times we know that the transfer function does not have any poles in the right-half plane [[71](#)]. The effect of [Equation 5.4](#) can be understood as a "waterbed effect", where reducing the frequency noise in a certain frequency regime always causes the increase of the noise in another frequency regime by the feedback loop.

| Spectrum       | $f(A_{\text{comp}})$ [kHz] | $A_{\text{comp}}$ [dBc · Hz] | $f(A_{\text{amp}})$ [kHz] | $A_{\text{amp}}$ [dBc · Hz] | $A_{\text{amp}}/A_{\text{comp}}$ |
|----------------|----------------------------|------------------------------|---------------------------|-----------------------------|----------------------------------|
| <b>Probe</b>   |                            |                              |                           |                             |                                  |
| Optimal        | 5-310                      | $-2.04 \times 10^7$          | 310-2380                  | $6.60 \times 10^7$          | 3.24                             |
| Worsened       | 5-230                      | $-1.86 \times 10^7$          | 230-1060                  | $3.07 \times 10^7$          | 1.65                             |
| <b>Control</b> |                            |                              |                           |                             |                                  |
| Optimal        | 5-238                      | $-2.43 \times 10^7$          | 238-5000                  | $3.64 \times 10^7$          | 1.50                             |
| Worsened       | 5-106                      | $-3.17 \times 10^7$          | 106-5000                  | $4.94 \times 10^7$          | 1.56                             |

Table 5.1: Areas of compensation  $A_{\text{comp}}$  and amplification  $A_{\text{amp}}$  of the frequency noise in the probe and control feedback loop. The values were calculated from the spectra shown in Figure 5.1 and Figure 5.2. Each  $f(A_{\text{comp}})/f(A_{\text{amp}})$  denotes the boundaries for integration.

To check this relation the integral in Equation 5.4 is broken down into two parts

$$\underbrace{\int_{S_{\nu,\text{locked}} < S_{\nu,\text{unlocked}}} \log \left| \frac{S_{\nu,\text{locked}}}{S_{\nu,\text{unlocked}}} \right|}_{A_{\text{comp}}} + \underbrace{\int_{S_{\nu,\text{locked}} > S_{\nu,\text{unlocked}}} \log \left| \frac{S_{\nu,\text{locked}}}{S_{\nu,\text{unlocked}}} \right|}_{A_{\text{amp}}} = 0. \quad (5.5)$$

Integration are  $A_{\text{comp}}$  corresponds to the case, where the feedback loop suppresses noise and is compared  $A_{\text{amp}}$ , where the feedback loop is amplifying the noise. However, we only consider the spectra shown in Figure 5.1 and Figure 5.2 and cannot integrate up to infinite frequencies. The results and the integration boundaries are shown in Table 5.1.

In the case of the probe the result of the integrals is affected by the spectra settling at different heights for high frequencies. This is not expected and results most likely from a systematic uncertainty. To compensate for this, only the area of the servo bump should be integrated when calculating  $A_{\text{amp}}$ . For both lock configurations of the probe (optimal and worsened) the area  $A_{\text{amp}}$  is significantly larger than  $A_{\text{comp}}$ . Therefore, Bode's integral formula cannot be confirmed with this measurement.

Compared to the measured spectra of the probe beam the difference between these spectra for high frequencies is significantly smaller as expected due to the roll-off. When comparing the areas  $A_{\text{comp}}$  and  $A_{\text{amp}}$  between the spectrum of the unlocked and the locked laser one also observes again that  $A_{\text{amp}}$  is larger for the optimal and the intentionally worsened setting of the Fast Analog Controller.

The deviation might have multiple origins here: Firstly, it is not possible to measure the entire spectrum due to the interferometers feedback loop setting compensating for low frequencies (below 1 kHz) and the suppression effect of the interferometer at 20 MHz. The difference between the spectra at high frequencies supports the impression that there might be systematic shift of the spectrum heights leading to a systematic error. Most importantly is that Bode's integral formula describes the mathematically ideal feedback system and therefore rather demonstrates an upper boundary. In the actual feedback loop the components of the feedback loop introduce additional noise and thus increase  $A_{\text{amp}}$  and  $A_{\text{comp}}$ .

One has to note here, that the previous calculation compares the change of the noise power spectral densities on a logarithmic scale. This does not mean that the noise is increased on a linear scale as well. Typically, when observing frequency noise traces as shown in Figure 4.5, a reduction in the amplitude factor  $\sim 4$  was observed when locking a laser.

### 5.3 Stability of the Servo Bump Position

As shown in [Figure 5.1](#) and [Figure 5.2](#) the position of the servo bump can be changed with the settings of the Fast Analog Linewidth Control. Additionally, the feedback loop is susceptible to outer disturbances. When performing the measurements of the probe and the control frequency noise power spectral density, it is observed that the position of the servo bump would occasionally move between measurements.

[Figure 5.3](#) shows the position of the control laser servo bump  $f_{\text{servo}}$  measured over a period of 17 hours, with the FALC set to the worsened settings. At the beginning of the measurements the control laser is turned on and locked and every 20 s the frequency noise spectral density is measured. Simultaneously, the temperature  $T_{\text{amb}}$  on the laser table, the barometric pressure  $p_{\text{amb}}$  and the power that is coupled into the ULE cavity  $P_{\text{cav}}$  are monitored (see [Figure 5.3](#)). To extract the movement of the servo bump to each of the recorded spectrum a curve of the form

$$a(f) = \frac{a}{1 + (f - b)^2/c} \cdot e^{d \cdot f} \quad (5.6)$$

is fitted, where  $f$  denotes the frequency of the noise components and  $a, b, c, d$  denote fitting parameters. This model is purely phenomenologically motivated as it resembles frequency noise spectral density around the servo bump and allows extracting the position  $f_{\text{servo}}$  of the servo bump. In [Figure 5.3](#) one can see how the servo bump is oscillating and drifting in the first hour and then settles at around 500 kHz. After 12 hours the servo bump then drifts again by  $\sim 30$  kHz.

The temperature on the laser table settles after  $\sim 5$  hours and then remains constant. The overall change is  $\sim 0.2^\circ\text{C}$  and does not match the trend of the servo bump position  $f_{\text{servo}}$  in time.

Similar observation can be made for the barometric pressure: The change in the pressure is below 1% and does not correspond to the movement of the servo bump. Thus, it can be concluded that the temperature and the pressure do not significantly contribute to the movement of the servo bump.

Across the measurement period it was observed that the power in the control light used for the frequency stabilization with the ultra-low-expansion cavity does fluctuate. In total this drift corresponds to about 0.3% of the total power. A change in the light power affects the height of the error signal going into the Fast Analog Laser Controller. This is similar to a change of the controllers main gain by 0.3%. When the control servo bump was intentionally lowered by  $\sim 600$  kHz (see [Figure 5.2](#)) the main gain was reduced from 0.3 to 0.2. To estimate an upper boundary for the impact of such a power drift, it is assumed that the servo bump was only shifted due to the change of the main gain. Extrapolating this change in the servo position leads to a change of  $\sim 12$  kHz if the main gain is changed by 1%, where a change by 0.2 corresponds to 100%. That leads to the conclusion that due to the power drifts the servo bump drifts by  $\sim 4$  kHz. Since a significantly larger drift is observed, there seem to be more effects adding up here leading to the shift of the servo bump.

Since the shift in the frequency seemingly does not originate from outer factors monitored, the drift in the servo bump might originate from a shift of the laser diodes internal noise spectrum. As shown in [Figure 3.5](#), the frequency emitted by a free-running laser is dependent on the gain profiles of the grating, the external and the internal cavity. If the e.g. temperature or the current of the diode are changing this shifts the position of these profiles, which impacts the frequency noise spectrum of the free-running laser. If the carrier frequency of the laser is closer to the borders of the mode-hop-free tuning range, the intrinsic frequency noise of the laser is expected to increase [72].

To verify whether this effect is significantly contributing to the drift of the servo bump the frequency

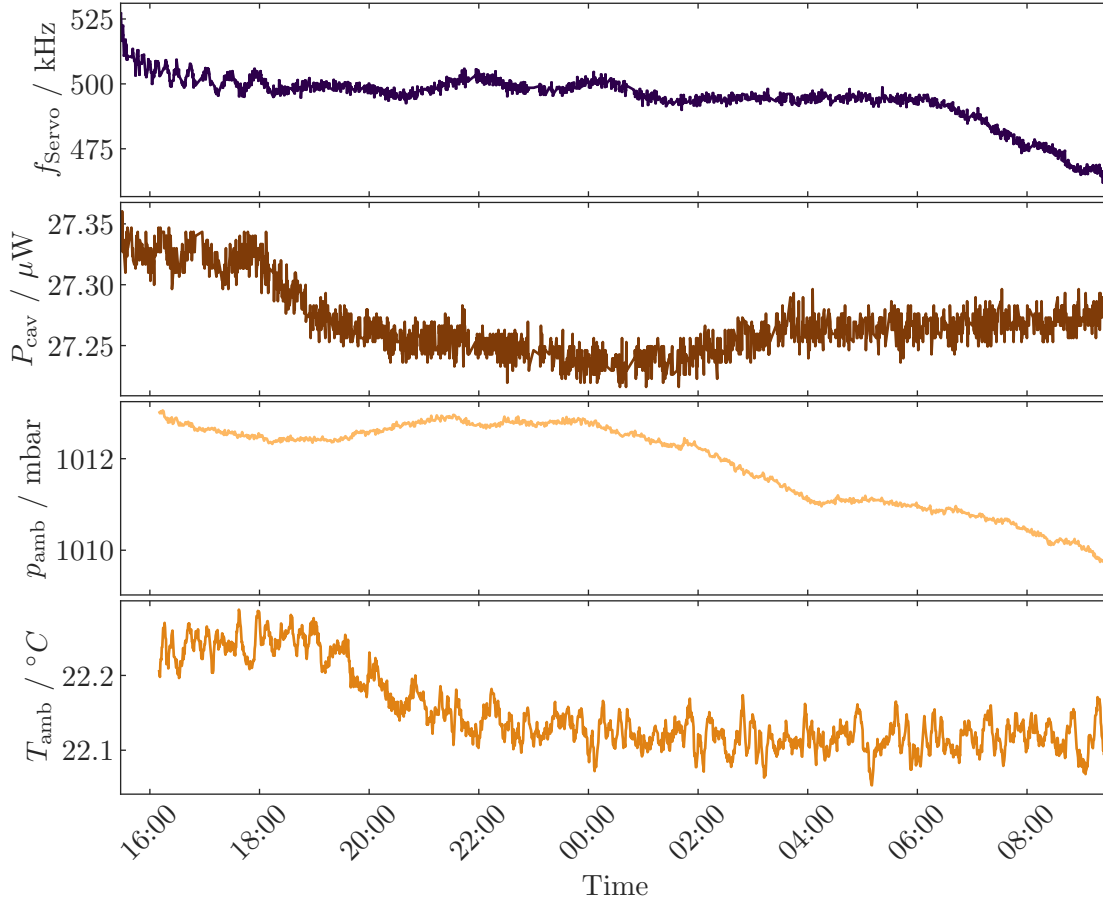


Figure 5.3: Measured servo bump location of the locked control laser over 17 hours. (First row) This graph shows the location of the control laser servo bump across the measurement time. Every 20 s the frequency noise spectral density of the laser was measured and a function of the form Equation 5.6 was fitted to the data to extract the location  $f_{\text{servo}}$  of the servo bump peak. (Second row) Shows the light power of the control laser towards the ultra-low-expansion cavity. (Third row) The barometric pressure in the laboratory. (Fourth row) Temperature on the optical stabilized laser table of the Control laser and the ULE cavity. At the same time the temperature is stabilized with an additional sensor.

noise spectral density of the locked control laser was measured for different single-photon detunings  $\Delta_c$ . This corresponds to a change of the length of the external cavity of the laser, which only affects the gain profile of the external cavity. In this way, for each detuning a different region in the mode-hop-free tuning range is sampled.

The upper row in Figure 5.4 shows the position and the height of the control servo bump for different detunings. The change of the servo bumps height indicates that the overall noise amplitude changed, since the feedback parameters remained untouched. A shift in the servo position indicates that the noise spectrum changed shape change, as the sensitivity function does not change for different detunings. Therefore, a significant shift in the servo bump is induced from the position of the laser in the mode-hop-free tuning range. This would explain the drift of the servo bump in the first hours of operation:

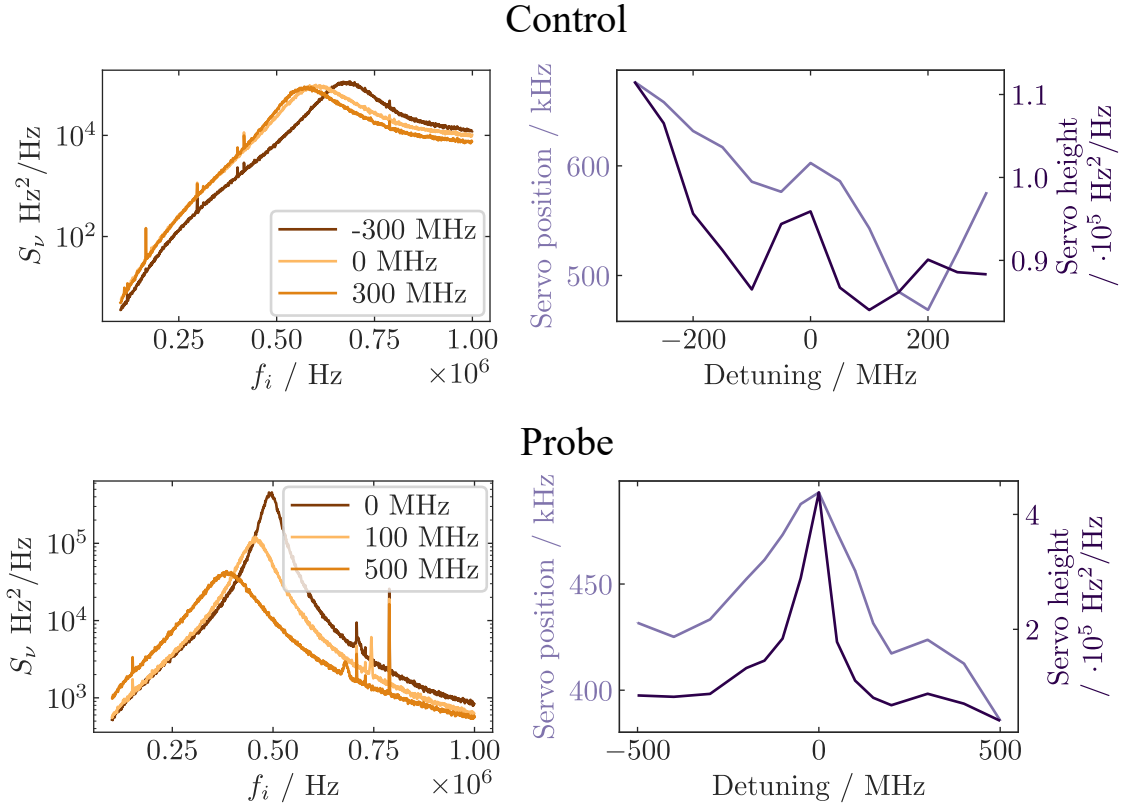


Figure 5.4: Measurement of the control and the probe servo bump depending on the detuning of the laser. (Left column) Three measured frequency noise power spectral densities depending on the single photon detuning  $\Delta_c$  ( $\Delta_p$ ) of the control (probe) laser, with the parameters of the feedback loop untouched. (Right) Dependence of the servo bump location and height on the detuning of the laser. The data is extracted from fitting curves of the form Equation 5.6 to the measured spectra (as the examples shown in the left column).

After turning on the laser the temperature inside the laser increased shifting the gain profiles of the laser components leading to differing frequency noise spectra inducing the observed shift in the servo bump. Still we have no knowledge, on how much the mode-hop-free tuning range actually drifted. Therefore, it can not be concluded whether this is the dominant effect contributing to the drift of the servo bump position.

In contrast to the control laser no significant drift of the probe servo bump position was observed, when doing performing a measurement as in Figure 5.3. To check whether the frequency noise spectrum of the probe laser also depends on the position of the carrier in the mode-hop-free tuning range, the probe frequency noise spectral density is measured for different detunings  $\Delta_p$  over the range of 1 GHz. The lower row in Figure 5.4 shows the result of this measurement. Compared to the control laser the shift in the position of the servo bump is smaller ( $\sim 100$  MHz instead of  $\sim 200$  MHz), whereas the height of the servo bump changes by a factor 4 between the edges and the center of the measurement. The measurement for different detunings shows that intrinsic noise of the probe laser does depend on the detuning. As no significant drifts had been observed the internal temperature of the probe laser works significantly better or the mode-hop-free tuning range of the probe is more stable against temperature or current drifts.

## 5.4 Simulation of a Noisy Two-Photon Rydberg Excitation

To predict and understand the impact of a noisy driving field on single-photon Rabi oscillations a numeric simulation can be used. In the following section the implementation of such a simulation is outlined and first features of the frequency noise are investigated using the simulation.

The idea behind the simulation is to calculate the light emitted by the superatom using the effective Hamiltonian from Equation 2.33 for a driving field with a fluctuating frequency. Multiple iterations of Rabi oscillations are generated and then averaged. For each single iteration, a noisy laser frequency trace is generated from the frequency noise spectral densities measured described in section 5.1. In this way an experimental measurement is simulated, where many iterations are averaged.

As a first step the measured frequency noise spectra of the probe  $S_{\nu,\text{probe}}$  and the control laser  $S_{\nu,\text{control}}$  need to be combined to one common noise spectrum of the effective driving light field  $S_{\nu,\text{eff}}$ . Therefore, the measured discrete spectra are summed up for every frequency entry  $S_{\nu,i}$

$$S_{\nu,\text{eff},i} = S_{\nu,\text{probe},i} + 4 \cdot S_{\nu,\text{control},i} \quad (5.7)$$

where the noise spectrum of the control is multiplied by a factor of 4. This factor captures that the frequency noise spectrum of the control laser was measured before frequency doubling. The second-harmonic-generation doubles the frequency fluctuations  $\Delta\nu(t)$  leading to a factor 4 increase in the effective spectrum (since  $\Delta\nu(t) \propto \sqrt{S_\nu}$ ).

With the total spectrum, frequency fluctuation time series  $\Delta\nu_{\text{eff}}(t)$  can be constructed and used to put in the Hamiltonian in Equation 2.33. A single time trace  $\Delta\nu_{\text{eff}}(t)$  is given by

$$\Delta\nu_{\text{eff}}(t) = \sum_i \sqrt{2S_{\nu,\text{eff},i}\Delta f} \cos(2\pi f_i t + \Phi_{f,i}) \quad (5.8)$$

where the phases  $\Phi_{f,i}$  are randomly drawn between 0 and  $2\pi$ . This leads to differing frequency traces for each iteration generation of  $\Delta\nu_{\text{eff}}(t)$ . To have the simulation comparable to the experiment a simulation length of 10  $\mu\text{s}$  is chosen. This corresponds to the length of the Tuckey pulses driving the Rabi oscillations as shown in Figure 3.2.

With a fluctuation frequency time trace one can calculate the density matrix of the superatom driven by a noisy light field. For that, typical values from Rabi oscillation measurements for  $\kappa$ ,  $R_{\text{in}}$ ,  $\Gamma$  and  $\gamma_D$  are used. In the simulation it is assumed that the probe laser is running at one constant level  $R_{\text{in}}$  and that the atomic ensemble is in the ground state  $|G\rangle$  at  $t = 0$ . Using the effective Hamiltonian

$$H_{\text{eff}}(t) = \hbar\sqrt{\kappa}(\sqrt{R_{\text{in}}}\sigma_{GW} + \sqrt{R_{\text{in}}}\sigma_{GW}^\dagger) + (\delta/2 + \dot{\Phi}(t))(\sigma_{DD} + \sigma_{WW} - \sigma_{GG}), \quad (5.9)$$

the time evolution of the superatom density matrix  $\rho(t)$  developed using `qutip.mesolve` [37] from the Lindblad master equation in Equation 2.11. With knowledge of the density matrix one can then calculate the outgoing light field  $R_{\text{out}}$  using Equation 2.13.

This procedure is repeated 300 times and an averaged Rabi oscillation trace is calculated. Figure 5.5 shows a simulation of the outgoing light field for four different input probe photon rates  $R_{\text{in}}$  using the values for  $\kappa$ ,  $\Gamma$  and  $\gamma_D$  from the measurement shown in Figure 3.2. The simulation was done using the optimal frequency noise spectra of the probe and the control laser. One can see how the individual traces vary significantly over the simulation time. This causes a loss in amplitude in the averaged curve.

To extract the values of  $\gamma_\nu$  from these curves, the same fitting procedure as for the experimental

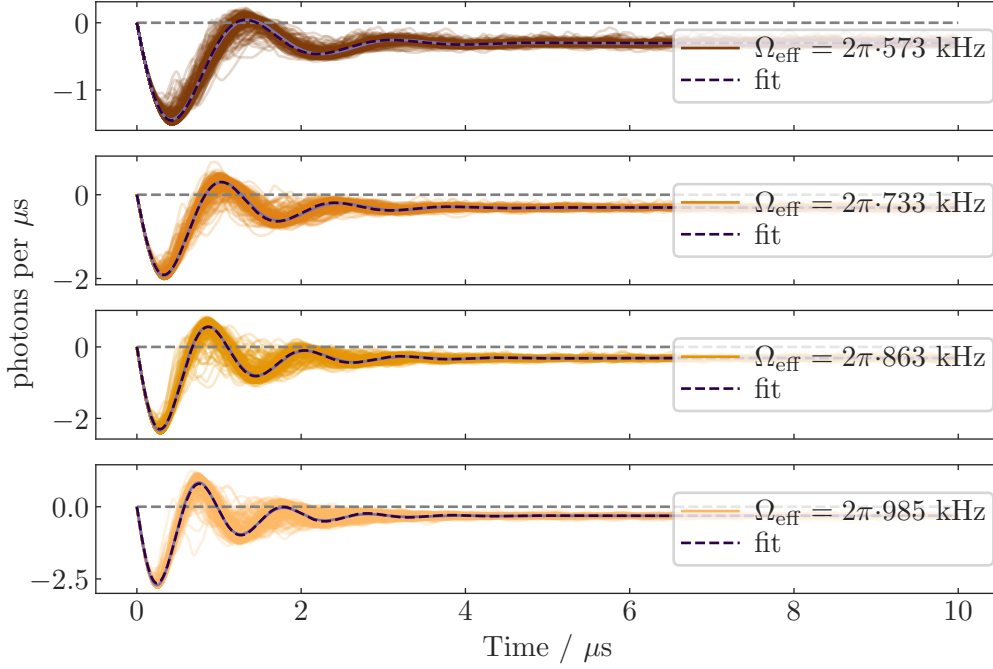


Figure 5.5: Simulated dephasing of superatom Rabi oscillations due to noisy driving fields. For each input power  $R_{\text{in}} = 10.6, 17.3, 24.0, 31.3$  photons per  $\mu\text{s}$  (top to bottom) 300 traces were computed. To calculate the frequency fluctuation the optimal probe and control frequency noise spectral densities were used. The colored traces show the individual Rabi oscillation traces for randomly generated frequency traces  $\Delta\nu_{\text{eff}}(t)$ . From each set of traces a mean trace is calculated (light purple) and the fitting model is applied (dark purple). The fit parameters are in the first column of Table 5.3. The input parameters for the simulation are  $\kappa = 0.31$  MHz,  $\gamma_D = 1$   $1/\mu\text{s}$  and  $\Gamma = 0.4$   $1/\mu\text{s}$ .

measurements is applied to the averaged curves. Therefore, out of the four oscillation traces with differing  $R_{\text{in}}$  common values for  $\kappa$ ,  $\Gamma$  and  $\gamma_D$  are obtained.  $\gamma_v$  is determined for each trace independently. The results of the simulation are shown in the first column of Table 5.3.

In principle one would expect that the fitted values for  $\kappa$ ,  $\Gamma$  and  $\gamma_D$  do not differ from the initial values fed into the simulation. As seen in Table 5.3, the values obtained from simulation and experiment do however differ. This is attributed to correlations between the fit parameters. Table 5.2 shows the linear correlation coefficients between the fit parameters for the simulation shown in Figure 5.5. The correlation coefficient  $C_{xy}$  between two fitting parameters  $x$  and  $y$  is given by [73]

$$C_{xy} = \frac{\text{cov}(x, y)}{\sigma_x \sigma_y} \quad (5.10)$$

where  $\text{cov}(x, y)$  denotes the covariance between  $x$  and  $y$ .  $\sigma_x$  and  $\sigma_y$  denote the standard deviations of  $x$  and  $y$ . If the correlation coefficient is  $\pm 1$  this means that both parameters are exactly linearly dependent on each other (with a positive/negative slope) and if  $C_{xy}$  is 0 that means that  $x$  and  $y$  are fully uncorrelated [74].

|               | $\kappa$ | $\Gamma$ | $\gamma_D$ | $\gamma_{v1}$ | $\gamma_{v2}$ | $\gamma_{v3}$ | $\gamma_{v4}$ |
|---------------|----------|----------|------------|---------------|---------------|---------------|---------------|
| $\kappa$      | 1.00     | -0.43    | 0.58       | -0.26         | -0.32         | -0.36         | -0.38         |
| $\Gamma$      | -0.43    | 1.00     | -0.81      | 0.40          | 0.46          | 0.51          | 0.54          |
| $\gamma_D$    | 0.58     | -0.81    | 1.00       | -0.50         | -0.61         | -0.69         | -0.73         |
| $\gamma_{v1}$ | -0.26    | 0.40     | -0.50      | 1.00          | 0.31          | 0.35          | 0.37          |
| $\gamma_{v2}$ | -0.32    | 0.46     | -0.61      | 0.31          | 1.00          | 0.43          | 0.45          |
| $\gamma_{v3}$ | -0.36    | 0.51     | -0.69      | 0.35          | 0.43          | 1.00          | 0.51          |
| $\gamma_{v4}$ | -0.38    | 0.54     | -0.73      | 0.37          | 0.45          | 0.51          | 1.00          |

Table 5.2: Correlation coefficients of the fit parameters from the simulation shown in [Figure 5.5](#).  $\gamma_{v1}$  corresponds to the trace with the lowest input photon rate  $R_{in}$  and  $\gamma_{v4}$  corresponds to the trace with the highest input photon rate  $R_{in}$ .

The correlation coefficients on the diagonal are all 1 because  $\text{cov}(x, x) = \sigma_x \sigma_x$ . In [Table 5.2](#) the highest correlation is between  $\Gamma$  and  $\gamma_D$  with  $C_{\Gamma\gamma_D} = -0.89$ . This means that the fitting model can poorly “distinguish” between these two. The negative sign in the correlation coefficient shows that if one of them increases the other one has to decrease.

$\gamma_D$  is also strongly correlated to the frequency noise induced dephasings  $\gamma_{v1}$ ,  $\gamma_{v2}$ ,  $\gamma_{v3}$  and  $\gamma_{v4}$ . Therefore, if frequency noise is introduced in the simulation and the average trace is fitted, the value of  $\gamma_D$  compensates for this dephasing, even though the mathematical rate of atoms transitioning in to the dark state does not change.

Comparing the averaged and fitted Rabi oscillation traces in [Figure 5.5](#) one can see that the fit is able to capture the decay of amplitude with a good accuracy. However, the oscillation frequency between the averaged and the fitted trace seems to differ slightly. This is most clearly visible in the case with the lowest Rabi frequency of  $2\pi \cdot 573$  kHz. The best agreement in the oscillation frequency is there for a Rabi frequency of  $2\pi \cdot 984$  kHz. Therefore, the difference between the fit and the averaged trace is also an effect of the frequency noise of the driving field. This shows that the fitting model from [Equation 2.39](#) is only an approximation and does not capture the dynamics of the superatom exactly.

Using the simulation we investigate the impact of the height and the shape of the frequency noise spectral densities on the measured frequency noise induced dephasing rate  $\gamma_v$ .

First the dependence of the dephasing rate  $\gamma_v$  on the height of the spectrum is investigated. The total spectrum is multiplied with a factor  $\beta$  and the simulation is performed. The left plot in [Figure 5.6](#) shows the dependence of  $\gamma_v$  on  $\beta$ . Overall a linear relation between  $\gamma_v$  and  $\beta$  is observed. The fluctuations in the relation are due to cross-talk between the fit parameters. According to [Equation 2.37](#)  $\gamma_v$  scales quadratically with the frequency  $\Delta_v(t)$ . As  $\Delta_v(t)$  scales with  $\sqrt{S_v}$  (see [Equation 5.8](#)) a linear relation between  $\beta$  and  $\gamma_v$  is expected from the theoretical model.

Secondly, the simulation is used to investigate which frequency noise components contribute most significantly to the dephasing  $\gamma_v$ . For this procedure is applied: a simulation of Rabi oscillations is performed for varying Rabi frequencies between  $550 \cdot 2\pi$  kHz and  $1100 \cdot 2\pi$  kHz. For each Rabi frequency 300 traces are generated with  $\kappa = 0.31$  MHz,  $\gamma_D = 1$  1/ $\mu$ s and  $\Gamma = 0.4$  1/ $\mu$ s. By averaging over these traces a mean trace is computed, and the photon signal is fitted using [Equation 2.39](#) to obtain  $\gamma_v$ .

The right plot in [Figure 5.6](#) shows the result of this simulation. The dephasing rate  $\gamma_v$  is plotted against the Rabi frequency  $\Omega_{eff}$ . One can see that the values for  $\gamma_v$  are strongly fluctuating, which is due

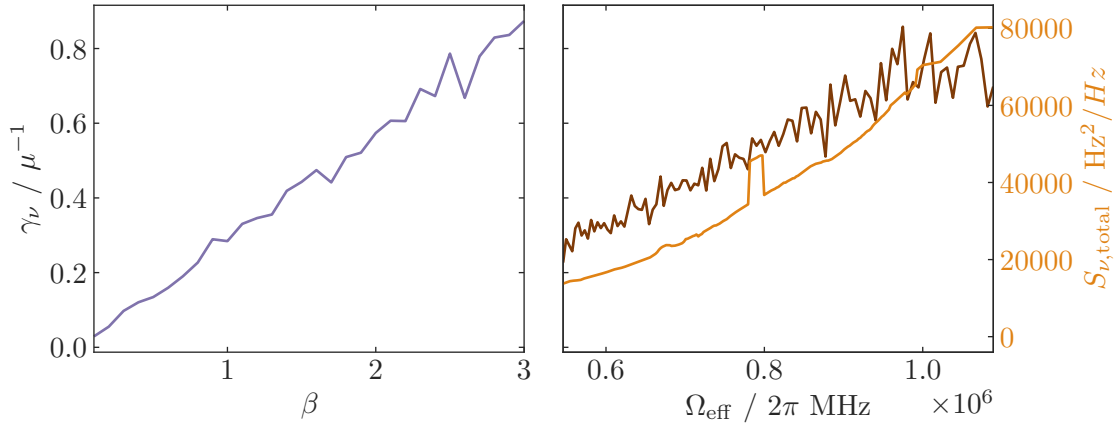


Figure 5.6: Simulating frequency noise dephasing for different noise powers and detunings. (Left) Simulated  $\gamma_\nu$  for different heights of the total noise spectrum. For each data point the total frequency noise spectrum was multiplied with the factor  $\beta$  a simulation averaging over 300 traces was performed with an input photon rate of  $R_{\text{in}} = 10.3$  photons per  $\mu\text{s}$ . (Right) Simulated  $\gamma_\nu$  (brown) for different Rabi frequencies  $\Omega_{\text{eff}}$  plotted with the total frequency noise spectrum used (orange). Each data point for  $\gamma_\nu$  is obtained from a Rabi oscillation simulation averaging over 300 traces using the total frequency noise spectral density shown. The spectrum is plotted against its frequency components  $f_i$ . In both plots  $\kappa = 0.31$  MHz,  $\gamma_D = 1$   $1/\mu\text{s}$  and  $\Gamma = 0.4$   $1/\mu\text{s}$  were used as initial parameters.

to the high correlation between the fitting parameters and because a single trace is fitted. Comparing the values of  $\gamma_\nu$  to the total frequency noise spectral density, one can see that the trend of  $\gamma_\nu$  approximately resembles the noise spectrum. This indicates that mainly the noise around the Rabi frequency significantly contributes to the dephasing. Therefore, to reduce  $\gamma_\nu$  in the experiment one has to reduce the frequency noise spectral density of the probe and the control laser at the Rabi frequency.

## 5.5 Comparing Simulated and Measured Dephasing Rates

In our experiment, we would like to determine how much laser noise of the probe and the control laser contribute to the overall dephasing in the Rabi oscillations of the superatom. In the previous section the influence of the noise spectrum was investigated with the help of simulations, which can be directly compared to experimental measurements.

As it was shown in Figure 5.6 the dephasing  $\gamma_\nu$  due to frequency noise strongly depends on the height of the noise spectrum at the Rabi frequency. Therefore, it is expected that the experimentally measured dephasing rate  $\gamma_\nu$  depends on the shape of the total noise spectrum. This dependency is investigated by changing the slope of the total frequency noise spectrum from positive to approximately flat to negative over the typical range of Rabi frequencies (500 kHz to 1 MHz).

The simulation and the experiment are compared for three different configurations of the total noise spectrum shown in the top row of Figure 5.7: Column (I) shows probe and control laser in the optimal setting of their Fast Analog Laser Controller with both servo bumps at  $\sim 1.1$  MHz. In column (II) the probe is at the optimal and control laser is at the worsened setting leading to plateau in the total spectrum around the Rabi frequencies realized in the experiment. For column (III) the probe and control laser

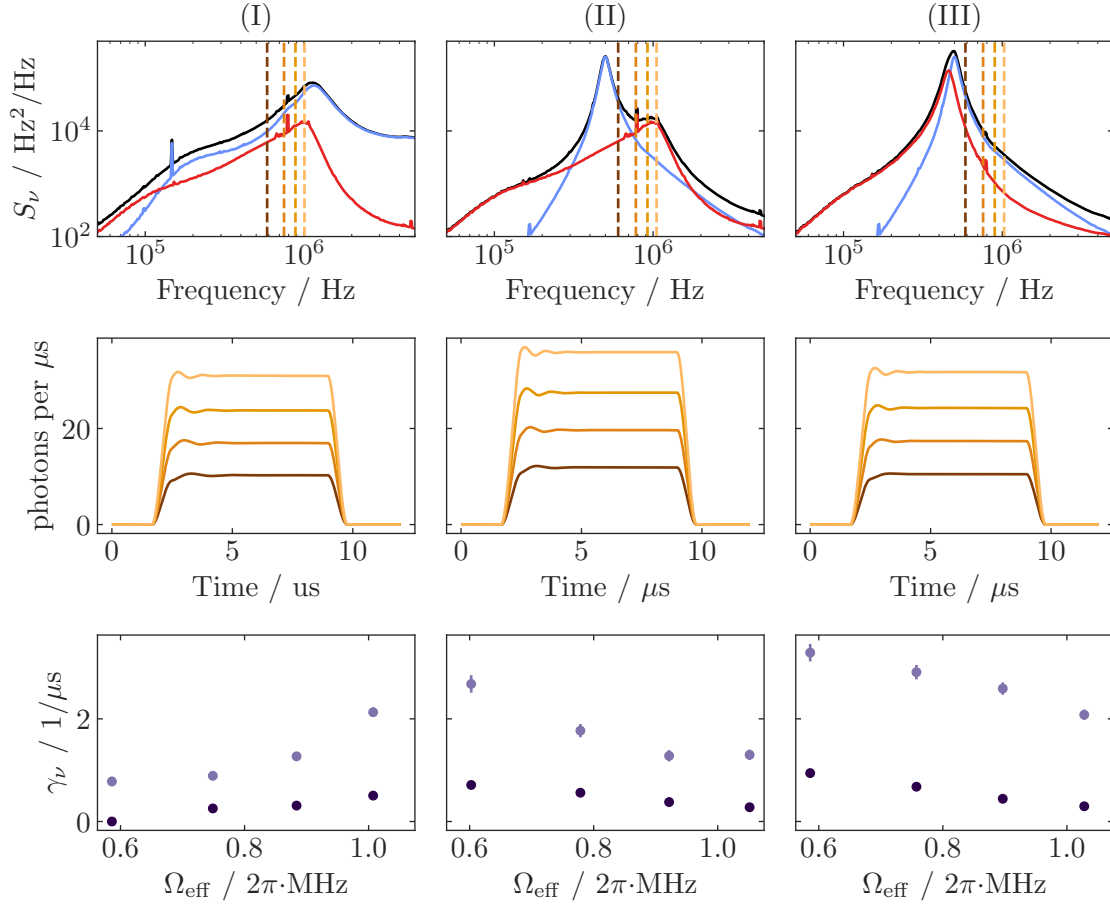


Figure 5.7: Comparison the experimental and simulated frequency noise induced dephasing for three configurations of the noise spectra of the probe and control laser. (Top row) Frequency noise power spectral densities of the probe (red), control (blue) and the combined effective (black) laser fields. The dashed vertical lines indicate the Rabi frequencies that probed in the experiment and the simulation the colors correspond to the traces in the middle row. (Middle row) Traces fitted to the experimentally measured Rabi oscillations. The height corresponds to the input photon rate  $R_{\text{in}}$ . The fit parameters are denoted in Table 5.3. (Bottom row) Comparison between the values of  $\gamma_\nu$  obtained from experiment (light purple) and simulation (dark purple) plotted against the Rabi frequency  $\Omega_{\text{eff}} = 2\sqrt{\kappa R_{\text{in}}}$ .

are at the worsened setting. This leads to a servo bump around 500 kHz and a falling slope between 500 kHz and 1 MHz.

For each configuration the measurement is done for four different probe photon rates  $R_{\text{in}}$  (see second row in Figure 5.7). Each photon rate corresponds to a different Rabi frequency (see dashed lines in the first row of Figure 5.7). The experimental and simulated values for  $\kappa$ ,  $\Gamma$ ,  $\gamma_D$  and  $\gamma_\nu$  are listed in Table 5.3

The last line in Figure 5.7 compares the values for  $\gamma_\nu$  obtained from simulation and experiment. To make the simulated Rabi traces comparable to the experimentally measured Rabi oscillations, the values of  $\kappa$ ,  $\gamma_D$  and  $\Gamma$  extracted from the experimental data were used as input variables for the simulation.

Comparing the values for  $\gamma_\nu$  for the optimal setting of probe and control (I) in simulation and

| Spectrum                   | (I)        |            | (II)       |            | (III)      |            |
|----------------------------|------------|------------|------------|------------|------------|------------|
|                            | Simulation | Experiment | Simulation | Experiment | Simulation | Experiment |
| $\kappa$ [MHz]             | 0.30583(5) | 0.31(1)    | 0.36220(2) | 0.35(1)    | 0.36742(5) | 0.35(1)    |
| $\Gamma$ [1/ $\mu$ s]      | 0.4099(2)  | 0.42(1)    | 0.4807(2)  | 0.48(1)    | 0.3222(2)  | 0.32(1)    |
| $\gamma_D$ [1/ $\mu$ s]    | 1.044(2)   | 0.91(4)    | 0.961(1)   | 0.94(6)    | 1.149(1)   | 1.16(5)    |
| $R_{in,1}$ [1/ $\mu$ s]    | 10.6       | 10.6       | 12.2       | 12.2       | 10.8       | 10.8       |
| $\gamma_{v1}$ [1/ $\mu$ s] | 0.2445(4)  | 0.78(9)    | 0.712(3)   | 2.68(17)   | 0.943(4)   | 3.29(17)   |
| $R_{in,2}$ [1/ $\mu$ s]    | 17.3       | 17.3       | 20.0       | 20.0       | 17.6       | 17.6       |
| $\gamma_{v2}$ [1/ $\mu$ s] | 0.499(4)   | 0.89(8)    | 0.561(3)   | 1.77(13)   | 0.678(4)   | 2.91(14)   |
| $R_{in,3}$ [1/ $\mu$ s]    | 24.0       | 24.0       | 27.8       | 27.8       | 24.5       | 24.5       |
| $\gamma_{v3}$ [1/ $\mu$ s] | 0.555(4)   | 1.27(8)    | 0.379(2)   | 1.28(11)   | 0.443(3)   | 2.59(12)   |
| $R_{in,4}$ [1/ $\mu$ s]    | 31.3       | 31.3       | 36.2       | 36.2       | 32.0       | 32.0       |
| $\gamma_{v4}$ [1/ $\mu$ s] | 0.749(4)   | 2.13(9)    | 0.278(2)   | 1.30(10)   | 0.297(2)   | 2.08(10)   |

Table 5.3: Fitting parameters obtained from experimental and from simulated data. The corresponding noise spectra of the probe and the control laser are shown in Figure 5.7. For the simulated data the values for  $\kappa$ ,  $\Gamma$  and  $\gamma_D$  were used as corresponding starting values. The rates of probe photons were measured in photons per  $\mu$ s

experiment, one notes that the dephasing  $\gamma_v$  is increasing as expected due to the total frequency noise spectrum in the top row. However, there is an offset between experimentally obtained and the simulated values. Additionally, the experimental values increase more rapidly with the Rabi frequency than the simulated values for  $\gamma_v$ .

In the other two cases of the flat (II) and falling (III) total noise spectrum one makes a similar observation: Both experiment and simulation show the same trend in  $\gamma_v$  but the experimentally obtained values are significantly higher.

The matching trends between the experimental and the simulated data show that the frequency noise induced dephasing  $\gamma_v$  is a significant effect contributing to the dephasing of the Rabi oscillations. The fact that the effect changes depending on the total noise spectrum confirms, that this is not just another e.g. power-dependent dephasing effect.

This difference between the simulated and the experimentally obtained values for  $\gamma_v$  can have multiple origins: In the fit obtained from the simulation in all cases either the value for  $\gamma_D$  or  $\kappa$  increased compared to the experimentally obtained value. This reduces the obtained values for  $\gamma_v$ , as the correlation coefficients of  $\gamma_D$  and  $\kappa$  with  $\gamma_v$  are all negative (see Table 5.3). The cross-talk between the fitting parameters also applies to the evaluation of the experimental data.

Also in the simulation, the frequency noise spectra of probe and control are expected to be static. This is not accurate on long time-scales (see Figure 5.3). Since the experimental measurements are performed over several hours to collect good statistics, a slow drift in the servo bump of the probe or control laser can impact the measurement result. This causes an averaging over different rates of  $\gamma_v$ , resulting in an of the measured values of  $\gamma_v$ .

The measurements shown in Figure 5.7 experiment confirms, what the simulation already suggested: If one wants to reduce the dephasing due to frequency noise, the total frequency noise spectral density has to be reduced at the Rabi frequency  $\Omega_{\text{eff}}$  of the Rabi oscillations. In the experiment these are typically between  $2\pi \cdot 500$  kHz and  $2\pi \cdot 1$  MHz.

One approach for a reduction of dephasing could be to increase the speed of the feedback loop. This

would shift the servo bump towards higher frequencies and reduce the noise at the Rabi frequencies. Such improvements are fundamentally limited by the bandwidth of the feedback loops components, especially the laser, and the cables between the components, which are already reduced to the minimum.

Another approach could be to intentionally reduce the bandwidth of the feedback loop, such the servo bump is shifted to a position much lower than 500 kHz. For a slower feedback loop these noise spectra between 500 kHz and 1 MHz resemble the free-running laser. Therefore, the improvement is limited by the intrinsic frequency noise of the probe and control laser. As the noise spectrum of the free running laser is falling for increasing frequencies, the dephasing would still be dependent on the Rabi frequency. Additionally, the stability of the lock suffers from the reduction of the bandwidth.

---

## Conclusion & Outlook

---

The goal of this thesis was to assess whether frequency noise of the probe and the control laser significantly contributes to the dephasing of Rydberg superatom Rabi oscillations measured in the RQO experiment.

In the first part of this thesis, the effect of frequency fluctuations in of optical field driving a two-level-system were discussed. We showed that the frequency fluctuation can be treated as a variation in the detuning of the driving field. When averaging over many experimental realizations, these frequency fluctuations can be approximated in the Lindblad Master equation as an additional term  $\frac{\gamma_v}{2} \mathcal{L}(\sigma_{WW})$ . The term describes the loss of coherence between the ground state  $|G\rangle$  and the bright state  $|W\rangle$ . Therefore, this dephasing effect is fundamentally different from e.g. thermal dephasing, since other effects describe a transition from the from  $|W\rangle$  to the manifold of dark states  $\{|D\rangle\}$ .

Afterward, it was described how the superatoms are realized experimentally and how the lasers driving the superatoms are stabilized in their frequency. The latter is crucial in the context of this thesis as the frequency stabilization loop determines the noise spectra of the probe and the control laser.

In order to measure the frequency noise spectra of the probe and control laser a laser noise interferometer was constructed in the scope of this thesis. With the interferometer, it is possible to obtain the frequency noise power spectral density of a laser between  $\sim 1$  kHz and  $\sim 10$  MHz, which is the relevant range for the dephasing of Rabi oscillations. The interferometer can not only measure the probe and the control laser, but any laser with a wavelength between  $\sim 770$  nm and  $\sim 1000$  nm.

With knowledge of the probe and the control frequency noise spectra, the impact of the frequency noise on the Rabi oscillation signal was simulated by approximating the dephasing numerically. Comparing the simulation and the experimental results it was possible to show that the frequency noise plays a significant role in the dephasing of the Rydberg superatom. A key observation from the simulation was that the height of the total noise spectrum at the Rabi frequency determines the dephasing rate  $\gamma_v$ , and noise at frequencies far away from the Rabi frequency barely contribute.

In the experiment, we use Rabi frequency in the range between  $2\pi \cdot 500$  kHz and  $2\pi \cdot 1$  MHz. In the case of the optimal frequency stabilization, the probe and the control laser have their servo bump at  $\sim 1.1$  MHz. Because the total frequency noise spectrum has a rising slope between 500 kHz and 1 MHz, the dephasing  $\gamma_v$  increases with the Rabi frequency, leading to varying values for  $\gamma_v$ , depending on the strength of the driving field  $R_{in}$ .

Manipulating the frequency noise spectra of the probe and the control laser led to a falling slope in the total frequency noise spectrum. This allowed inverting the trend of dephasing rate  $\gamma_v$ , such that it then decreases with growing  $R_{in}$ . This proofed the observed dephasing is indeed due to the frequency noise

of the excitation lasers.

## 6.1 Outlook

In order to increase the coherence time of the Rabi oscillations, one has to reduce the frequency noise of the excitation lasers for noise frequencies between 500 kHz and 1 MHz. To reduce the frequency noise in this range, one could make the feedback loops either significantly faster or slower pushing the servo bump of the probe and the control laser away from the Rabi frequencies. In order to increase the bandwidth of the feedback loop, one could replace the FALC controller by a controller that is capable of producing a larger phase lead at high frequencies.

The interferometer setup presented in this thesis was used to measure the frequency noise of the excitation lasers to gain insights in the frequency noise induced dephasing of the Rydberg superatom. The setup could also be used to actively suppress the noise using a feed-forward line. In reference [43], such a setup has already been implemented. In the setup the light from a diode laser is broken down into two arms. One arm contains a fiber-based interferometer, which is similar to the one presented in this thesis. The interferometer is used to measure the frequency noise in real-time. The light in the second arm is delayed with an optical fiber and then sent through an Electro-Optical-Modulator (EOM). The signal from the interferometer sent into the EOM which counteracts the frequency fluctuations in the laser light. With this method, it is possible to suppress the laser frequency noise by more than 20 dB in the frequency range between 1 MHz and 10 MHz. As the frequency noise induced dephasing  $\gamma_\nu$  scales approximately linearly with the height of the noise spectrum, with an active noise suppression by 20 dB we would be able to reduce the frequency noise induced dephasing by a factor up to 100. This would bring a significant improvement in the coherence time of the superatom.

## Appendix

### A.1 Superatom Dephasing due to Inhomogeneous Density of the Atomic Cloud

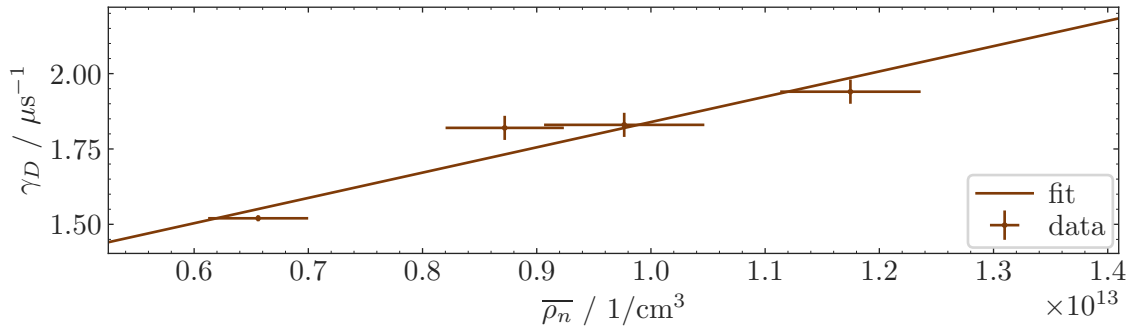


Figure A.1: Measurement of the density induced dephasing. Rabi oscillation measurements with the for the  $89S$ -state of Rubidium-87 with a detuning of 200 MHz were performed while varying the atomic density. A description of the measurement procedure and atom preparation scheme to obtain  $\gamma_D$  can be found in [section 3.2](#). The atom number and temperature of the atomic cloud was measured with absorption images of the atomic cloud expansion (for a detailed explanation see [17]). With knowledge of the trapping beam parameters (powers and detuning) the atomic density distribution can be obtained. The atomic density is modified by varying the power of the Repumper beam to change the number of loaded atoms. To rule out differential light shifts affecting trend of  $\gamma_D$  all experiments were performed with the same trapping conditions. Between the measurements the temperature of the atomic ensemble differs by less than 5%, such that it is assumed that thermal dephasing does not influence the trend of the data points.

This measurement investigates whether inhomogeneous density increases the dephasing of the superatom. In the experiment Rabi oscillations were measured for different densities of the atomic cloud (see [Figure A.1](#)). The dephasing rate  $\gamma_D$  is plotted against the weighted atomic density  $\bar{\rho}$  in the case where the Rydberg atom is sitting in the center of the atomic trap. If the peak density is increased this corresponds to an increase of the overall density induced shift over the atomic cloud or detuning “seen” by the atoms. As shown in the example for the differential light shift the decay rate  $\tau_{dl}$  scales with the detuning. Thus,

a linear relation between  $\bar{\rho}$  and the dephasing rate  $\gamma_D$  is expected.

To verify this expectation a linear fit function was fitted to the recorded data points. The fit seems to capture the overall trend of the data points, however due to the big errors on the density and the few data points in the measurement is not conclusive. A positive y-axis intercept is expected and captures the contribution of the other dephasing mechanisms. Therefore, this effect does indeed contribute significantly to the dephasing  $\gamma_D$ .

## A.2 Worsened Feedback Loop Settings

|      | Control |         |     | Probe   |         |     |
|------|---------|---------|-----|---------|---------|-----|
|      | $f_1$   | $f_2$   | $K$ | $f_1$   | $f_2$   | $K$ |
| XSLI | -       | -       | 1   | -       | -       | 1   |
| SLI  | 2.4 kHz | 140 kHz | 1   | 1.1 kHz | 65 kHz  | 1   |
| FLI  | 65 kHz  | 800 kHz | 1   | 300 kHz | 3.5 MHz | 1   |
| FLD  | 2.3 MHz | 420 kHz | 5   | 1 MHz   | 190 kHz | 5   |

Table A.1: Set corner frequencies of the Main branch of the Fast Analog Laser Controller of the probe and the control beam for the intentionally lowered servo bump. In both cases the XSLI was turned off.

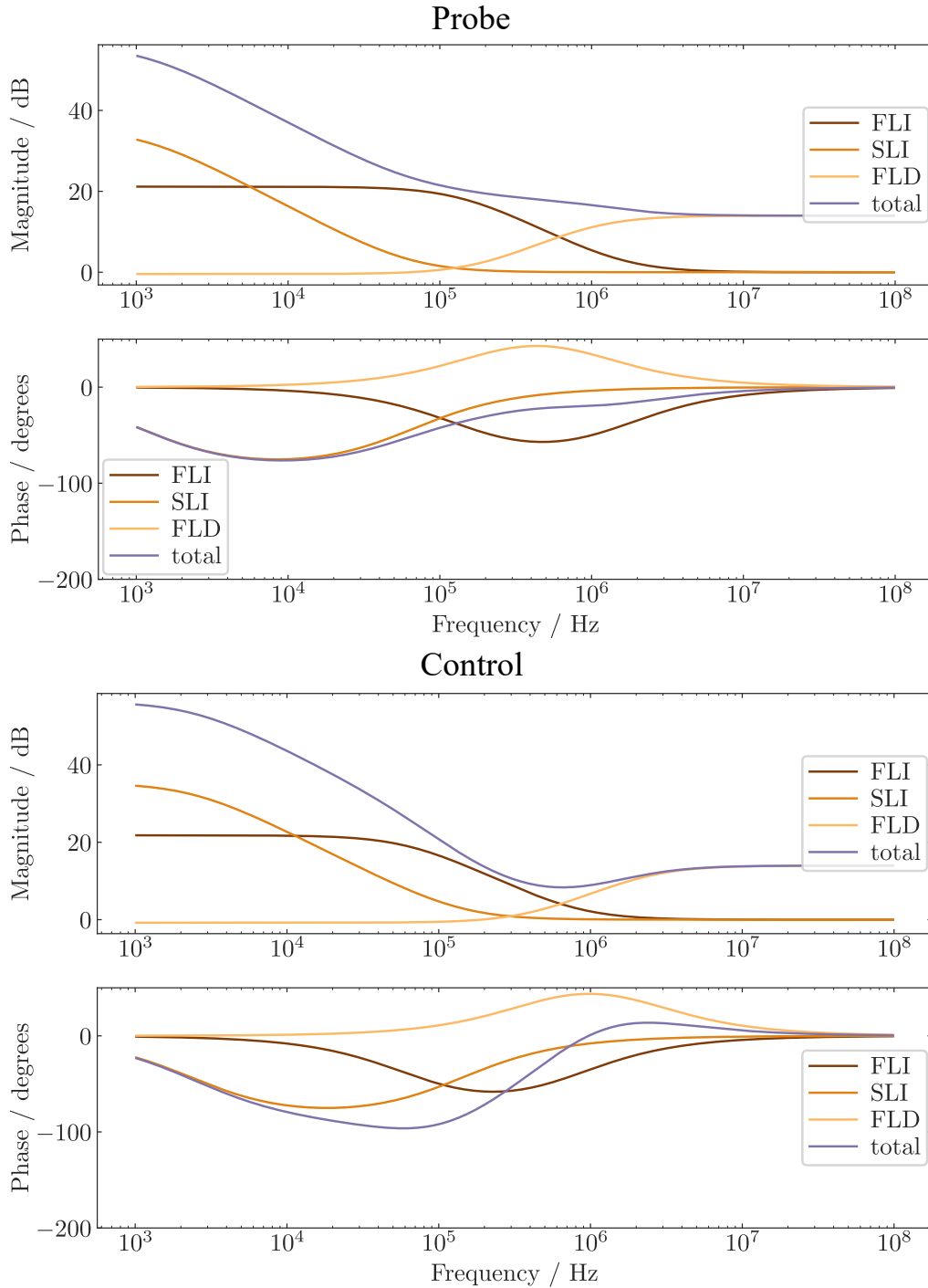


Figure A.2: Open-loop Bode plots of the Fast Analog Linewidth Control of the probe and control laser for the settings from Table A.1. The transfer functions of the Extra Slow Limited Integrator (XSLI), Slow Limited Integrator (SLI), Fast Limited Integrator (FLI) and the Fast Limited Differentiator (FLD) were calculated using Equation 3.8 to produce the phase and amplitude relation between in- and output of each component. The transfer function of the Extra Slow Limited Integrator is not plotted here as it is turned off. The total transfer function (light purple) was calculated from the product of the components' transfer functions. In the calculation the limited bandwidth of the controller was neglected.

---

## Acknowledgements

---

At this point I would like to thank all those, who helped me work out this thesis. Especially I would like to thank

- Professor Hofferberth for the possibility of doing my Master thesis in his group. After the great experience during my Bachelor thesis it took me little thought to return.
- The entire RQO team: Lukas for discussing every question, whether smart or not so smart, and great kicks on the football pitch. Nina for sharing knowledge on whatever topic of interest: Whether it is what a superatom feels or what my sick plants need the most. Daniil for lots of great fun at the lab and engaged discussions about the yummiest cuisines in the world. Jan for being a great lab companion in the starting phase of my thesis. Eduardo for broadening my knowledge in Wigner functions and my -very limited- Spanish skills.
- To the entire NQO team: Lukas T., Florian G., Daniel, Benedikt, Cedric, Valerie, Julia, Sam, Xin, Tangi, Ludwig, Knut, Eduardo and Eduardo, Florian P., Jan, Nina, Lukas A., Daniil, Wolfgang, Tina and Sebastian. Thank you for making the time so much fun and helping to find whatever I was looking for: Whether it is an oscilloscope, an experimental tip or a random discussion for lunch.
- To the nonlinear-quantum climbers: Eduardo, Sam, Daniil, Bennet and all those who will join in the future. You made the time after the lab lots of fun and reminded me that walls are meant for climbing.
- All those who had the pleasure (or sorrow) of proofreading parts of this thesis: Julia, Cedric, Eduardo, Wolfgang, Daniil and especially Lukas and Nina. Thank you for helping me complete this thesis and remove all (unnecessary) parenthesis.
- To all my friends and family, who made the past year very enjoyable, whether it was in- or outside the university. Without all of you I couldn't have made it.

# Bibliography

---

- [1] D. Browne, S. Bose, F. Mintert, and M. S. Kim, *From Quantum Optics to Quantum Technologies, Progress in Quantum Electronics, Special Issue in Honor of the 70th Birthday of Professor Sir Peter Knight FRS* **54** (2017) 2.
- [2] G. Leuchs and M. and Sondermann, *Light–Matter Interaction in Free Space, Journal of Modern Optics* **60** (2013) 36.
- [3] J. M. Raimond, M. Brune, and S. Haroche, *Manipulating Quantum Entanglement with Atoms and Photons in a Cavity, Reviews of Modern Physics* **73** (2001) 565.
- [4] A. Reiserer and G. Rempe, *Cavity-Based Quantum Networks with Single Atoms and Optical Photons, Reviews of Modern Physics* **87** (2015) 1379.
- [5] M. D. Lukin, M. Fleischhauer, R. Cote, L. M. Duan, D. Jaksch, J. I. Cirac, and P. Zoller, *Dipole Blockade and Quantum Information Processing in Mesoscopic Atomic Ensembles, Physical Review Letters* **87** (2001) 037901.
- [6] A. Paris-Mandoki, C. Braun, J. Kumlin, C. Tresp, I. Mirgorodskiy, F. Christaller, H. P. Büchler, and S. Hofferberth, *Free-Space Quantum Electrodynamics with a Single Rydberg Superatom, Physical Review X* **7** (2017) 041010.
- [7] D. P. Ornelas-Huerta, A. N. Craddock, E. A. Goldschmidt, A. J. Hachtel, Y. Wang, P. Bienias, A. V. Gorshkov, S. L. Rolston, and J. V. Porto, *On-Demand Indistinguishable Single Photons from an Efficient and Pure Source Based on a Rydberg Ensemble, Optica* **7** (2020) 813.
- [8] S. Shi, B. Xu, K. Zhang, G.-S. Ye, D.-S. Xiang, Y. Liu, J. Wang, D. Su, and L. Li, *High-Fidelity Photonic Quantum Logic Gate Based on near-Optimal Rydberg Single-Photon Source, Nature Communications* **13** (2022) 4454.
- [9] N. L. R. Spong, Y. Jiao, O. D. W. Hughes, K. J. Weatherill, I. Lesanovsky, and C. S. Adams, *Collectively Encoded Rydberg Qubit, Physical Review Letters* **127** (2021) 063604.
- [10] W. Xu, A. V. Venkatramani, S. H. Cantú, T. Šumarac, V. Klüsener, M. D. Lukin, and V. Vuletić, *Fast Preparation and Detection of a Rydberg Qubit Using Atomic Ensembles, Physical Review Letters* **127** (2021) 050501.
- [11] J. Wang, J. P. Wang, L. Dong, X. M. Xiu, and Y. Q. Ji, *Fast Generation of Quantum Logic Gate with Rydberg Superatoms, Optics & Laser Technology* **187** (2025) 112812.
- [12] T. D. Ladd, F. Jelezko, R. Laflamme, Y. Nakamura, C. Monroe, and J. L. O’Brien, *Quantum Computers, Nature* **464** (2010) 45.

## Bibliography

---

- [13] B. Zhao, Y.-A. Chen, X.-H. Bao, T. Strassel, C.-S. Chuu, X.-M. Jin, J. Schmiedmayer, Z.-S. Yuan, S. Chen, and J.-W. Pan, *A Millisecond Quantum Memory for Scalable Quantum Networks*, *Nature Physics* **5** (2009) 95.
- [14] I. Mirgorodskiy, F. Christaller, C. Braun, A. Paris-Mandoki, C. Tresp, and S. Hofferberth, *Electromagnetically Induced Transparency of Ultra-Long-Range Rydberg Molecules*, *Physical Review A* **96** (2017) 011402.
- [15] J. Lampen, H. Nguyen, L. Li, P. R. Berman, and A. Kuzmich, *Long-Lived Coherence between Ground and Rydberg Levels in a Magic-Wavelength Lattice*, *Physical Review A* **98** (2018) 033411.
- [16] L. Ahlheit, C. Nill, D. Svirskiy, J. de Haan, S. Schroers, W. Alt, N. Stiesdal, I. Lesanovsky, and S. Hofferberth, *Magic Running- and Standing-Wave Optical Traps for Rydberg Atoms*, *Physical Review A* **111** (2025) 013115.
- [17] J. A. de Haan, *Characterization of a 1D Magic Wavelength Lattice for Increasing the Coherence Time of Rydberg Superatoms*, MA thesis: Rheinische Friedrich-Wilhelms-Universität Bonn, 2024.
- [18] M. Schlosshauer, *Decoherence and the Quantum-To-Classical Transition*, Frontiers Collection, Berlin, Heidelberg: Springer, 2007, ISBN: 978-3-540-35773-5 978-3-540-35775-9.
- [19] J. Honer, R. Löw, H. Weimer, T. Pfau, and H. P. Büchler, *Artificial Atoms Can Do More Than Atoms: Deterministic Single Photon Subtraction from Arbitrary Light Fields*, *Physical Review Letters* **107** (2011) 093601.
- [20] S. De Léséleuc, D. Barredo, V. Lienhard, A. Browaeys, and T. Lahaye, *Analysis of Imperfections in the Coherent Optical Excitation of Single Atoms to Rydberg States*, *Physical Review A* **97** (2018) 053803.
- [21] N. Akerman, N. Navon, S. Kotler, Y. Glickman, and R. Ozeri, *Universal Gate-Set for Trapped-Ion Qubits Using a Narrow Linewidth Diode Laser*, *New Journal of Physics* **17** (2015) 113060.
- [22] S. Schneider and G. J. Milburn, *Decoherence in Ion Traps Due to Laser Intensity and Phase Fluctuations*, *Physical Review A* **57** (1998) 3748.
- [23] J. R. Rydberg, XXXIV. On the Structure of the Line-Spectra of the Chemical Elements, *The London, Edinburgh, and Dublin Philosophical Magazine and Journal of Science* **29** (1890) 331.
- [24] A. Browaeys, D. Barredo, and T. Lahaye, *Experimental Investigations of Dipole–Dipole Interactions between a Few Rydberg Atoms*, *Journal of Physics B: Atomic, Molecular and Optical Physics* **49** (2016) 152001.
- [25] T. F. Gallagher, “Rydberg Atoms,” *Springer Handbook of Atomic, Molecular, and Optical Physics*, ed. by G. W. F. Drake, Cham: Springer International Publishing, 2023 231, ISBN: 978-3-030-73893-8.
- [26] O. Firstenberg, C. S. Adams, and S. Hofferberth, *Nonlinear Quantum Optics Mediated by Rydberg Interactions*, *Journal of Physics B: Atomic, Molecular and Optical Physics* **49** (2016) 152003.

## Bibliography

---

- [27] R. Löw, H. Weimer, J. Nipper, J. B. Balewski, B. Butscher, H. P. Büchler, and T. Pfau, *An Experimental and Theoretical Guide to Strongly Interacting Rydberg Gases*, *Journal of Physics B: Atomic, Molecular and Optical Physics* **45** (2012) 113001.
- [28] S. Weber, C. Tresp, H. Menke, A. Urvoy, O. Firstenberg, H. Büchler, and S. Hofferberth, *Tutorial: Calculation of Rydberg Interaction Potentials*, *Journal of Physics B: Atomic, Molecular and Optical Physics* **50** (2017).
- [29] E. Urban, T. A. Johnson, T. Henage, L. Isenhower, D. D. Yavuz, T. G. Walker, and M. Saffman, *Observation of Rydberg Blockade between Two Atoms*, *Nature Physics* **5** (2009) 110.
- [30] A. Gaëtan, Y. Miroshnychenko, T. Wilk, A. Chotia, M. Viteau, D. Comparat, P. Pillet, A. Browaeys, and P. Grangier, *Observation of Collective Excitation of Two Individual Atoms in the Rydberg Blockade Regime*, *Nature Physics* **5** (2009) 115.
- [31] D. Tong, S. M. Farooqi, J. Stanojevic, S. Krishnan, Y. P. Zhang, R. Côté, E. E. Eyler, and P. L. Gould, *Local Blockade of Rydberg Excitation in an Ultracold Gas*, *Physical Review Letters* **93** (2004) 063001.
- [32] N. Stiesdal, *Intrinsic Three Photon Correlation Mediated by a Single Rydberg Superatom*, MA thesis: Univeristy of Southern Denmark, 2018.
- [33] E. Brion, L. H. Pedersen, and K. Molmer, *Adiabatic Elimination in a Lambda System*, *Journal of Physics A: Mathematical and Theoretical* **40** (2007) 1033.
- [34] R. H. Dicke, *Coherence in Spontaneous Radiation Processes*, *Physical Review* **93** (1954) 99.
- [35] M. O. Scully, E. S. Fry, C. H. R. Ooi, and K. Wódkiewicz, *Directed Spontaneous Emission from an Extended Ensemble of N Atoms: Timing Is Everything*, *Physical Review Letters* **96** (2006) 010501.
- [36] N. Stiesdal, *Collective Atom-Light Interactions with Rydberg Superatoms*, PhD thesis: University of Southern Denmark, 2022.
- [37] N. Lambert et al., *QuTiP 5: The Quantum Toolbox in Python*, 2024, arXiv: [2412.04705](https://arxiv.org/abs/2412.04705) [quant-ph].
- [38] D. A. Steck, *Rubidium 87 D Line Data*, 2024.
- [39] C. J. Foot, *Atomic Physics*, Oxford University Press, 2005, ISBN: 978-0-19-850695-9.
- [40] S. A. C. McDowell, *A Simple Derivation of the Boltzmann Distribution*, *Journal of Chemical Education* **76** (1999) 1393.
- [41] M. V. Sadovskii, *Statistical Physics*, De Gruyter, 2019, ISBN: 978-3-11-064848-5.
- [42] A. Gaj, A. T. Krupp, J. B. Balewski, R. Löw, S. Hofferberth, and T. Pfau, *From Molecular Spectra to a Density Shift in Dense Rydberg Gases*, *Nature Communications* **5** (2014) 4546.
- [43] T. Denecker, Y. T. Chew, O. Guillemant, G. Watanabe, T. Tomita, K. Ohmori, and S. de Léséleuc, *Measurement and Feed-Forward Correction of the Fast Phase Noise of Lasers*, *Physical Review A* **111** (2025) 042614.
- [44] P. Cladé, *Oscillations de Bloch d'atomes ultrafroids et mesure de la constante de structure fine*, PhD thesis: Université Pierre et Marie Curie-Paris VI, 2005.

## Bibliography

---

- [45] F. Schwabl, *Quantum Mechanics*, Springer Science & Business Media, 2007, ISBN: 978-3-540-71933-5.
- [46] U. Dorner, *Quantum Frequency Estimation with Trapped Ions and Atoms*, *New Journal of Physics* **14** (2012) 043011.
- [47] A. Omelyanchouk, S. Savel'ev, A. Zagoskin, E. Il'ichev, and F. Nori, *Noise-Induced Quantum Coherence and Persistent Rabi Oscillations in a Josephson Flux Qubit*, *Physical Review B* **80** (2009).
- [48] S. Schroers, *Raman-Seitenbandkühlung von Rubidiumatomen*, Bachelor Thesis: University of Bonn, 2022.
- [49] R. Grimm, M. Weidemüller, and Y. Ovchinnikov, *Optical Dipole Traps for Neutral Atoms*, *Advances in Atomic, Molecular, and Optical Physics* **42** (2000) 95.
- [50] C. S. Adams, H. J. Lee, N. Davidson, M. Kasevich, and S. Chu, *Evaporative Cooling in a Crossed Dipole Trap*, *Physical Review Letters* **74** (1995) 3577.
- [51] E. D. Black, *An Introduction to Pound–Drever–Hall Laser Frequency Stabilization*, *American Journal of Physics* **69** (2001) 79.
- [52] U. Schünemann, H. Engler, R. Grimm, M. Weidemüller, and M. Zielonkowski, *Simple Scheme for Tunable Frequency Offset Locking of Two Lasers*, *Review of Scientific Instruments* **70** (1999) 242.
- [53] K. J. Åström and R. M. Murray, *Feedback Systems: An Introduction for Scientists and Engineers*, Princeton: Princeton University Press, 2008, ISBN: 978-0-691-13576-2.
- [54] M. Mulder, M. M. Van Paassen, J. Flach, and R. Jagacinski, “Fundamentals of Systems and Control Theory,” *Fundamentals of Manual Control Theory*, 2005 12.1, ISBN: 978-0-8493-1937-2.
- [55] Toptica Photonics AG, *FALC 110 Fast Analog Linewidth Control*, M-044 Version 02, Manual, Graefeling/Munich, 2011.
- [56] Y. Zhu, B. Qiu, W. Li, and Z. Liu, *Mode-Hop-Free Synchronous Tuning Range Extension of an Uncoated External Cavity Diode Laser Based on PZT Hysteresis Characteristic Compensation*, *Applied Physics B* **130** (2024) 200.
- [57] T. Führer and T. Walther, *Extension of the Mode-Hop-Free Tuning Range of an External Cavity Diode Laser Based on a Model of the Mode-Hop Dynamics*, *Optics Letters* **33** (2008) 372.
- [58] Toptica Photonics AG, *DLpro HP Grating Stabilized Diode Laser Head Designed for DLC Pro*, M-59 Version 6, Manual, Graefeling/Munich, 2021.
- [59] A. L. Schawlow and C. H. Townes, *Infrared and Optical Masers*, *Physical Review* **112** (1958) 1940.
- [60] H. M. Wiseman, *Light Amplification without Stimulated Emission: Beyond the Standard Quantum Limit to the Laser Linewidth*, *Physical Review A* **60** (1999) 4083.
- [61] Y. Salvadé and R. Dändliker, *Limitations of Interferometry Due to the Flicker Noise of Laser Diodes*, *JOSA A*, Vol. 17, Issue 5, pp. 927-932 (2000).

## Bibliography

---

- [62] T. N. Huynh, S. P. Ó. Dúill, L. Nguyen, L. A. Rusch, and L. P. Barry, *Simple Analytical Model for Low-Frequency Frequency-Modulation Noise of Monolithic Tunable Lasers*, *Applied Optics*, Vol. 53, Issue 5, pp. 830-835 (2014).
- [63] S. A. Mahdi, *The Power Spectral Density of 1/f Noise in a Tunable Diode Laser at Different Temperatures*, *Journal of Optics* **47** (2018) 61.
- [64] L. D. Turner, K. P. Weber, C. J. Hawthorn, and R. E. Scholten, *Frequency Noise Characterisation of Narrow Linewidth Diode Lasers*, *Optics Communications* **201** (2002) 391.
- [65] J. Bechhoefer, *Feedback for Physicists: A Tutorial Essay on Control*, *Reviews of Modern Physics* **77** (2005) 783.
- [66] P. Ge and M. Jouaneh, *Modeling Hysteresis in Piezoceramic Actuators*, *Precision Engineering* **17** (1995) 211.
- [67] P. Welch, *The Use of Fast Fourier Transform for the Estimation of Power Spectra: A Method Based on Time Averaging over Short, Modified Periodograms*, *IEEE Transactions on Audio and Electroacoustics* **15** (1967) 70.
- [68] S. Braun, "WINDOWS," *Encyclopedia of Vibration*, ed. by S. Braun, Oxford: Elsevier, 2001 1587, ISBN: 978-0-12-227085-7.
- [69] W. Demtröder, *Experimentalphysik 2: Elektrizität und Optik*, Springer-Lehrbuch, Berlin, Heidelberg: Springer, 2013, ISBN: 978-3-642-29943-8 978-3-642-29944-5.
- [70] N. S. Nise, *Control Systems Engineering*, John Wiley & Sons, 2020, ISBN: 978-1-119-72140-6.
- [71] D. Trumper, *Analysis and Design of Feedback Control Systems*, Massachusetts Institute of Technology. Department of Mechanical Engineering (2007).
- [72] S.-w. Chiow, Q. Long, C. Vo, H. Mueller, and S. Chu, *Extended Cavity Diode Lasers with Tracked Resonances*, *Applied Optics* **46** (2007) 7997.
- [73] P. G. Bagos and M. Adam, *On the Covariance of Regression Coefficients*, *Open Journal of Statistics* **05** (2015) 680.
- [74] A. G. Asuero, A. Sayago, and A. G. González, *The Correlation Coefficient: An Overview*, *Critical Reviews in Analytical Chemistry* **36** (2006) 41.